

ON-LINE ESTIMATION OF IMPLEMENT DYNAMICS FOR ADAPTIVE
STEERING CONTROL OF FARM TRACTORS

Except where reference is made to work of others, the work described in this thesis is my own or was done in collaboration with my advisory committee. This thesis does not include proprietary or classified information

Evan R. Gartley

Certificate of Approval:

George T. Flowers
Professor
Mechanical Engineering

David M. Bevly, Chair
Assistant Professor
Mechanical Engineering

John Y. Hung
Associate Professor
Electrical and Computer Engineering

Stephen L. McFarland
Dean
Graduate School

ON-LINE ESTIMATION OF IMPLEMENT DYNAMICS FOR ADAPTIVE
STEERING CONTROL OF FARM TRACTORS

Evan Robert Gartley

A Thesis

Submitted to

the Graduate Faculty of

Auburn University

in Partial Fulfillment of the

Requirements for the

Degree of

Masters of Science

Auburn, Alabama
December 16, 2005

ON-LINE ESTIMATION OF IMPLEMENT DYNAMICS FOR ADAPTIVE
STEERING CONTROL OF FARM TRACTORS

Evan Robert Gartley

Permission is granted to Auburn University to make copies of this thesis at
its discretion, upon the request of individuals or institutions and
at their expense. The author reserves all publication rights.

Signature of the Author

Date of Graduation

THESIS ABSTRACT

ON-LINE ESTIMATION OF IMPLEMENT DYNAMICS FOR ADAPTIVE STEERING CONTROL OF FARM TRACTORS

Evan Robert Gartley

Master of Science, December 16, 2005
(B.M.E., Auburn University, 2003)

135 Typed Pages

Directed by David M. Bevly

An adaptive control technique for the control of a farm tractor during low levels of excitation and at low velocities is presented. Results of a set of system identification experiments are compared to previous tractor models. A cascaded controller is then designed for the feedback of steer angle, yaw rate, and lateral position based on the new tractor model. An on-line analysis of the data is used to determine if enough excitation is available for adaptation. A cascaded Kalman Filter is presented to estimate the slope of the DC gain of the steer angle to yaw rate transfer function, M_{DC} , with respect to velocity. An estimator also provides faster updates of position. From the on-line estimate of M_{DC} , the controller gains are scheduled based on a lookup table of predetermined values that were calculated from system identification tests.

The sensitivity of the controller to model simplifications, incorrect velocities, and M_{DC} estimate errors are investigated. The accuracy of the estimated M_{DC} due to neglected dynamics and the rate of convergence is shown. A simulation is used to show the errors that can be induced in the position estimator by the GPS delay. The yaw rate estimator is designed for fixed point math using a square root covariance filter. Experimental and simulation results are provided which show the validity of the M_{DC} estimate. Finally, experimental results which show that the accuracy changes little as a result of hitch loading and velocity are presented and discussed.

ACKNOWLEDGEMENTS

The author would like to thank the John Deere Corporation for providing a tractor for this research and Andy Rekow for providing assistance with the tractor. Thanks are expressed to the AU Agriculture Department for supplying land and an implement for testing. Thanks are also due to the entire GPS and Vehicle Dynamics Laboratory for their help.

Style of Journal Used:

ASME Journal of Dynamic Systems, Measurement, and Control

Computer Software Used:

Microsoft Word 2003

TABLE OF CONTENTS

LIST OF FIGURES.....	xi
LIST OF TABLES.....	xv
1. INTRODUCTION	
1.1 Motivation.....	1
1.2 Background.....	2
1.3 Outline of Thesis.....	3
1.3 Contributions.....	5
2. MODELING AND SYSTEM IDENTIFICATION	
2.1 Introduction.....	6
2.2 Steering Servo Dynamics.....	6
2.3 Previous Tractor Yaw Dynamics Models.....	9
2.4 8420 Tractor Yaw Dynamics.....	13
2.5 Summary and Conclusion.....	21

3.	CASCADED CONTROLLER DESIGN AND ANALYSIS	
3.1	Introduction.....	23
3.2	Steering Servo Controller.....	24
3.2	Yaw Rate Controller.....	26
3.3	Closed Loop Yaw Rate Sensitivity.....	31
3.4	Lateral Position Controller.....	38
3.5	Closed Loop Lateral Position Sensitivity.....	43
3.6	Summary and Conclusion.....	46
4.	STATE AND PARAMETER ESTIMATION	
4.1	Introduction.....	48
4.2	Extended Kalman Filter.....	48
4.3	Design of Yaw Rate Dual Estimator.....	53
4.4	Sensitivity of Estimation to Neglected Dynamics.....	59
4.5	Rate of Convergence.....	70
4.6	Design of Position Estimator.....	73
4.7	Effects of GPS Delay.....	79
4.8	Summary and Conclusion.....	85
5.	EXPERIMENTAL IMPLEMENTATION	
5.1	Introduction.....	86
5.2	Trajectory Design.....	86

5.3	Results.....	89
5.4	Summary and Conclusion.....	94
6.	FIXED POINT IMPLEMENTATION OF YAW RATE ESTIMATOR	
6.1	Introduction.....	95
6.2	Square Root Covariance Filter.....	95
6.3	Fixed Point Math.....	97
6.4	Estimator Model.....	98
6.5	Comparison Between Fixed and Floating Point Implementation.....	100
6.6	Summary and Conclusion.....	108
8.	CONCLUSIONS	
8.1	Summary.....	110
8.2	Recommendation for Future Work.....	112
	REFERENCES.....	114
	APPENDIX	
A	Experimental Setup.....	118

LIST OF FIGURES

2.1	Steady state steering rate versus command input.....	7
2.2	ETFE of steering servo dynamics from input to slew rate.....	9
2.3	Bicycle model augmented with a hitch force and moment.....	10
2.4	Comparison of ETFE and Box Jenkins Fits.....	14
2.5	Experimental fits of DC gain.....	15
2.6	Experimental fits of the dominant poles.....	17
2.7	Experimental fits of the secondary poles.....	18
2.8	Experimental fits of the imaginary zeros.....	19
2.9	Experimental fits of the right half plane zero time constant.....	20
3.1	Block diagram of the controller system.....	23
3.2	Block diagram of steering servo system.....	24
3.3	\hat{s}_1 versus velocity for each yaw model.....	29
3.4	\hat{r}_1 versus velocity for each model.....	30
3.5	Sensitivity of yaw rate closed loop for no implement.....	32
3.6	Root locus of closed loop yaw rate.....	33
3.7	Sensitivity of yaw rate closed loop with an implement.....	34
3.8	Sensitivity with no implement to too low M_{DC}	36

3.9	Sensitivity with no implement with 2 mph control gains.....	37
3.10	Sensitivity with no implement with 5 mph control gains.....	38
3.11	Controller values for various velocities and hitch loadings.....	41
3.12	Controller values for various velocities and hitch loadings.....	42
3.13	Sensitivity of lateral error closed loop for no implement.....	44
3.14	Sensitivity of lateral error closed loop with an implement.....	45
4.1	Windowed auto-correlation of steer angle.....	56
4.2	Estimate of M_{DC} and yaw rate.....	58
4.3	Mean M_{DC} versus input frequency using the input of $\delta = A \sin(\omega t)$	61
4.4	Magnitude and phase difference between yaw rate and steer angle times DC gain for $\delta = 5 \sin(3t)$	62
4.5	Estimate of M_{DC} with an input of $\delta = 5 \sin(3t)$	63
4.6	Standard deviation of estimated M_{DC} versus input frequency.....	64
4.7	Bode magnitudes divided by velocity for no implement.....	65
4.8	Bode magnitudes divided by velocity for various hitch loadings at 3 mph.....	66
4.9	Mean M_{DC} versus input frequency for second order model.....	68
4.10	Frequency response of the actual system and second order estimator model.....	69
4.11	Standard deviation of M_{DC} for improved estimator.....	70
4.12	Convergence from different offsets.....	71
4.13	Time to converge within 99.9 % of the correct value.....	72

4.14	Estimated standard deviation for M_{DC}	73
4.15	Delay in GPS messages.....	76
4.16	Comparison of measured and estimated course from experimental test....	78
4.17	North error.....	80
4.18	East error.....	82
4.19	Heading Error.....	83
4.20	Comparison of covariances for an estimator with no delay and estimator that is compensated for the delay.....	84
5.1	Tracking a straight line.....	87
5.2	Curved trajectory to the straight line.....	88
5.3	Estimation of M_{DC} during experimental tests.....	90
5.4	Lateral error versus velocity.....	91
5.5	Lateral error without an implement.....	92
5.6	Lateral error with a four shank ripper at a twelve inch depth.....	93
6.1	Windowed analysis of experimental data to determine when to adapt.....	101
6.2	Comparison of the estimation of the slope of the dc gain equation with respect to velocity for fixed and floating point using experimental data...	102
6.3	Comparison of the estimation of the yaw rate bias in fixed and floating point using experimental data.....	103
6.4	Comparison of the estimation of yaw rate in fixed and floating point using experimental data.....	104

6.5	Comparison of the estimation of yaw rate in fixed and floating point for simulated data.....	105
6.6	Comparison of the estimation of the yaw rate bias in fixed and floating point using simulated data.....	106
6.7	Comparison of the estimation of the yaw rate dc gain slope with respect to velocity in fixed and floating point for simulated data.....	107
6.8	Windowed analysis of experimental data to determine when to adapt.....	108
A.1	John Deere 8420 Tractor.....	118
A.2	Versallogic PC/104 CPU [Versallogic, 2005a].....	119
A.3	Versallogic PC/104 data acquisition board [Versallogic, 2005b].....	119
A.4	Versallogic VL-ENCL-4 Ruggedized Enclosure [Versallogic, 2005c].....	119
A.5	Bosch IMU.....	120
A.6	Steer angle sensor.....	120
A.7	Starfire GPS reciever.....	120

LIST OF TABLES

2.1	Steering servo input transformation.....	8
2.2	DC Gain Linear Fits.....	16
2.3	Tractor Model Parameters.....	21
3.1	Inverse mapping of steady state steering rate versus command value.....	25
3.2	Yaw rate controller values.....	30
3.3	Gain margin for yaw rate.....	35
3.4	Yaw rate controller values.....	42
3.5	Gain margin for lateral position.....	46
3.6	Phase margin for lateral position.....	46
4.1	Discrete noise values used for the yaw rate dual estimator.....	59
4.2	Square root of covariance of M_{DC} provided by the estimator.....	65
4.3	Discrete noise values used for the position estimator.....	79
5.1	Statistics of lateral error.....	94

CHAPTER 1

INTRODUCTION

1.1 Motivation

Farm tractor models vary widely due to the many configurations possible and the different ground conditions encountered. The controller must give an adequate response to a system in which towed or hitched implements of varying sizes can be used at a wide range of depths. By automating tracking operations, costs such as row overlaps can be reduced. Also, less trained operators can be used without a reduction in accuracy and tractor operations can be performed during low visibility.

Due to the various implement loadings that are possible, a controller designed for a time-invariant vehicle model has the potential to either have a poor response or go unstable. Therefore, it is desired to have a controller that can compensate for the change in dynamics. It is also desired to not add more sensors to the tractor and as such only sensors that can be found on tractors that currently have an option for a controlled response were used. Complicating the problem, desired trajectories consist of straight line segments, which lead to low levels of excitation. Also, the implement depth is not set until the straight line trajectory begins. Therefore, fits from when the tractor is lining up for the controlled run are not applicable for the controller design.

The algorithms designed must also be able to operate on a low cost microcontroller. The microcontroller that is considered for this research is only capable of fixed point math.

1.2 Background

A number of companies currently produce tractor control systems for tracking straight lines, such as John Deere and Beeline Technologies, which use GPS for navigation. Work at Stanford developed simple tractor models and control algorithms that produced sub inch accuracy of a tractors position using carrier-phase differential GPS [O'Conner, 1996]. Further research allowed for the tracking of additional trajectories [Bell, 1999]. Additionally, combines have been controlled with GPS [Cordesses, 1999].

Before the use of GPS as a navigation system, computer vision was used for the control of tractors [Reid, 1987]. Research into blending the navigation of GPS and vision has shown improvements in position accuracy [Zhang, 1999]. A comparison of the blending of GPS with a magnetometer against using only GPS has also been shown [Benson, 1998].

System identifications of tractor dynamics between steer angle and yaw rate have been conducted for input frequencies up to one hertz, for controller design [Bevly, 2001; Stombaugh, 1998]. Additionally a model of a tractor tire has been developed which accounts for faulty circularity through the modification of a Pacejka Similarity Method tire model and has been verified with measured tire data [Bohler, 1999].

Numerous tire-soil interaction models exist [Saarilahti, 2002]. However, they are currently not used for the design of controllers for the lateral dynamics of tractors. Tractor models used for the design of tractor controllers have included kinematic models [O’Conner, 1997]. Kinematic models have also been able to model the dynamics between an object being towed and a vehicle [Svestka, 1995; Hingwe, 2000]. These kinematic models for the angle between the implement and tractor have been used to control the position of the implement [Bevly, 2001]. Controllers have also been designed for tractors modeled using a first order lag and a bicycle model [O’Conner, 1997]. A bicycle model with tire relaxations has been used to control a tractor at high velocities [Bevly, 2001].

Online adaptation of a tractor model has been investigated using an Extended Kalman Filter / LMS algorithm [Rekow, 2001]. That work identified the parameters defined in [O’Conner, 1997]. An adaptive controller has also been designed for a tractor’s steering servo to account for a changing dead band and dynamics [Wu, 2001]. Additionally, the slope of the DC gain with respect to velocity of the steer angle to yaw rate transfer function has been previously estimated along with a steering bias [Bell, 1999].

1.3 Outline of Thesis

In Chapter 2, system identification of the steering servo is performed and a model is presented which accounts for its nonlinearities. A review of previous yaw dynamic models for tractors is also covered. The results of open loop system identification experiments of a tractor with and without an implement are given. The similarities and

differences between the previously used models and the open loop system identification fits are discussed. It is justified that the slope of the DC gain with respect to velocity (M_{DC}) of the steer angle to yaw rate transfer function can be estimated rather than the DC gain. Finally, the model of the tractor used for the design of the controllers in this thesis is given.

In Chapter 3, the design of the controllers for the steering servo, yaw rate, and lateral position are detailed. The method of determining the controller gains using the estimation of the parameter M_{DC} is discussed. The sensitivity of the controllers to the model simplifications in Chapter 2, incorrect velocities, and an incorrect M_{DC} estimation are shown.

Chapter 4 develops a method for estimating the yaw rate and M_{DC} for the adaptation of the controller. A method of determining when there exists sufficient excitation to estimate M_{DC} is given. The rate of convergence upon initial determination of when to adapt is shown. The effect of the neglected dynamics on the estimation is displayed and a method of correcting for some of these errors is discussed. The rate of the convergence of the estimated parameter due to the forgetting factor in the estimator is shown. The design of the position estimator for providing faster updates of position is also detailed. The output equations for the estimator which account for the GPS delay are justified through the use of a simulation. Also, approximations are given for the errors that are induced from not including the GPS delay in the estimator, which are validated in simulation.

In Chapter 5, the design of the trajectories that were used for the tractor controller in this thesis are discussed. Experimental results showing the accuracy of the estimation

algorithms is given. It is shown that the tracking response using the estimation and adaptive control methods developed in this thesis do not vary significantly.

The estimator for the yaw rate and M_{DC} estimation is designed using fixed point calculations in Chapter 6. A comparison of estimators using fixed and floating point math are displayed for both experimental and simulation data. Finally, in Chapter 7, the conclusions and future work are given.

1.4 Contributions

A summary of the contributions provided in this thesis are listed below.

- A model for a John Deere 8420 tractor was developed using system identifications experiments
- A controller was designed which compensated for changes in velocity and hitch loading. Analysis showed that not accounting for changes in the velocity and hitch loading could cause the tractor controller to be unstable.
- An estimator was designed to estimate the effect of the hitch loading on the tractors dynamics. The accuracy and the amount of time for convergence was provided.
- A position estimator was designed which accounted for the delay in the receipt of the GPS message.
- A fixed point estimator was developed for estimating hitch loading through the parameter M_{DC} , in order to allow implementation of the algorithm on low cost microcontrollers.

CHAPTER 2

MODELING AND SYSTEM IDENTIFICATION

2.1 Introduction

In this chapter the modeling of the hydraulic steering servo and the tractors yaw rate dynamics will be discussed. While a number of different models have been presented for the yaw rate dynamics of a tractor, few have provided justifications of their designs through the use of system identification techniques, instead relying on controlled responses to determine which model gives the best results. A review of past models as well as their similarities to system identifications of a John Deere 8420 tractor is presented. While the past models do not adequately describe the yaw rate dynamics that of the 8420 tractor, it is shown that one of the models shows promise in describing the DC gain of the steer angle to yaw rate transfer function. The DC gain equation of this model will be used as part of the justification for only estimating the slope of the DC gain (M_{DC}). This will also be justified with the use of system identification results. Finally, the model that is used in the design of the controllers, which is based on the system identification results, is presented.

2.2 Steering Servo Dynamics

Based on earlier research [Bell, 1999], the steering servo dynamics were assumed to be a nonlinear system described using an input transformation and a transfer function

which included an integrator. An integrator is necessary since the steering servo is hydraulic with an input of flow rate and an output of steer angle. To identify the input transformation, constant inputs were commanded to the tractor resulting in the steer angle moving at a constant rate as shown below in Figure 2.1.

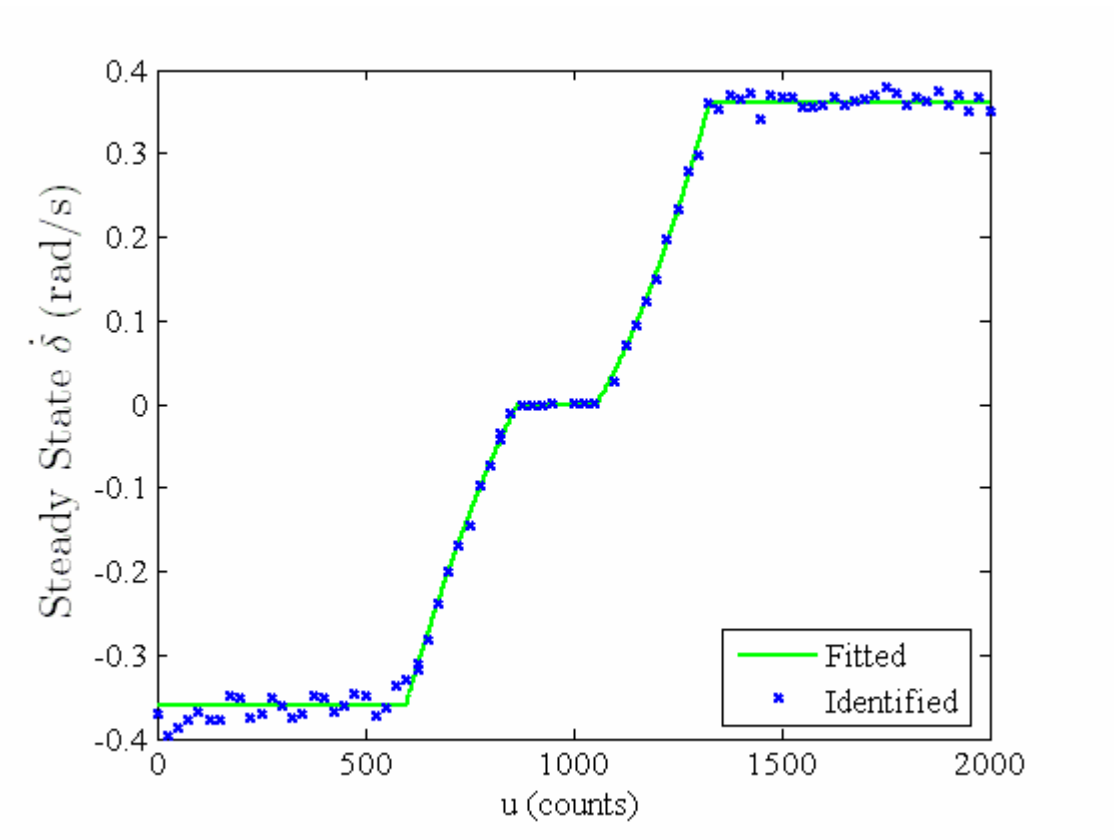


Figure 2.1: Steady state steering rate versus command input.

The steer angle measurement was differentiated with a center difference equation to obtain the steer angle rate, slew rate, for a wide range of inputs in order to produce the data in Figure 2.1. The input transformation was then modeled with a dead-band, saturations, and nonlinear equations with the values given in Table 2.1, where u is the

value provided to the tractor. The fitted model is also compared to the identified values in Figure 2.1.

Table 2.1: Steering servo input transformation

Steady State Slew Rate ($\dot{\delta}_{DC}$)	Input Command (u)
$\dot{\delta}_{DC} = -0.36$	$u < 598$
$\dot{\delta}_{DC} = -1.295e - 6u^2 + 0.00324u - 1.835$	$598 \leq u < 866$
$\dot{\delta}_{DC} = 0$	$866 \leq u < 1055$
$\dot{\delta}_{DC} = 1.859e - 6u^2 - 0.003111u + 1.213$	$1055 \leq u < 1325$
$\dot{\delta}_{DC} = 0.36$	$u \geq 1325$

To obtain the transfer function of the steering servo, a chirp input was given to the tractor while accounting for the input transformation, which is detailed in Chapter 3. The output was then differentiated with a center difference equation and an empirical transfer function estimate (ETF) [Ljung, 1999] was formed, Figure 2.2, which resembles a system which has two poles. A Box-Jenkins model [Ljung, 1999] was used to fit the system identification data.

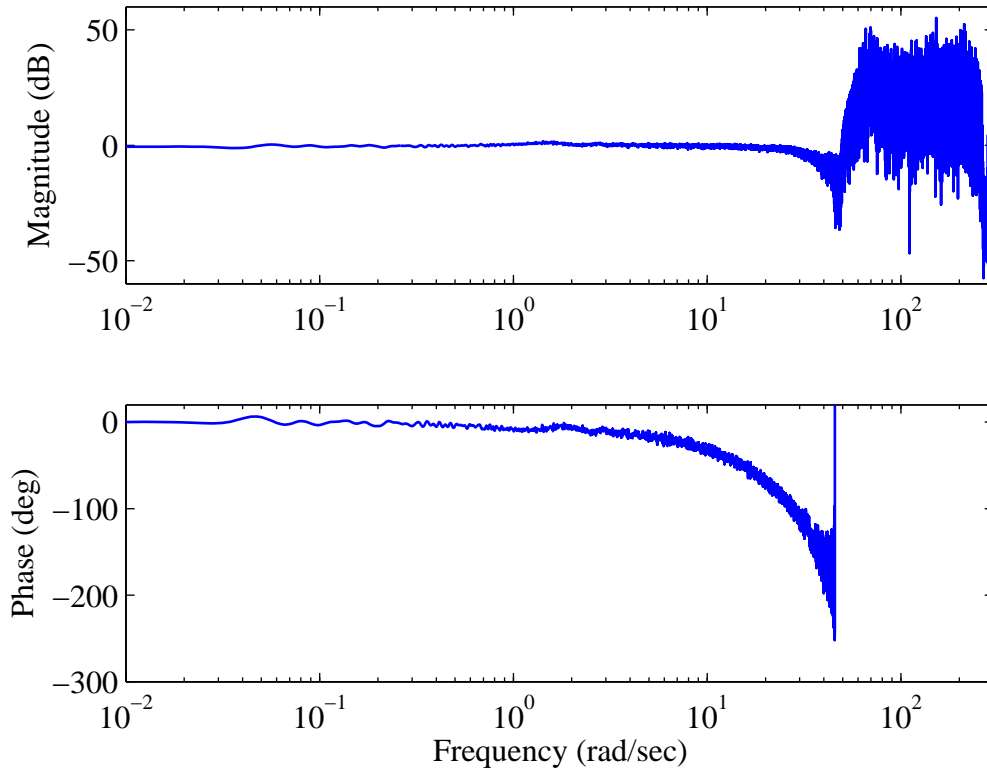


Figure 2.2: ETFE of steering servo dynamics from input to slew rate.

The Box-Jenkins model was then combined with the integrator to produce the discrete transfer function describing the steering servo dynamics (Equation (2.1)) at 100 hertz.

$$\frac{\delta}{u} = \frac{0.0063552511902254}{z^3 - 2.63184659881507z^2 + 2.33043587208497z - 0.69858927326991} \quad (2.1)$$

2.3 Previous Tractor Yaw Dynamic Models

The schematic displayed in Figure 2.3 is a common vehicle dynamics model known as the bicycle model [Wong, 1978], that has been augmented with the addition of

a hitch force and moment caused by an implement. The use of a towed implement would have no moment, while a hitched implement would have a force and moment. The bicycle model lumps the inner and outer tires and together and assumes that there is no weight transfer. The bicycle model also relates the forces at the tires to the velocities of the tire, through slip angles. The additional force that has been added for the implement will also be modeled as being a function of the slip angle at the hitch.

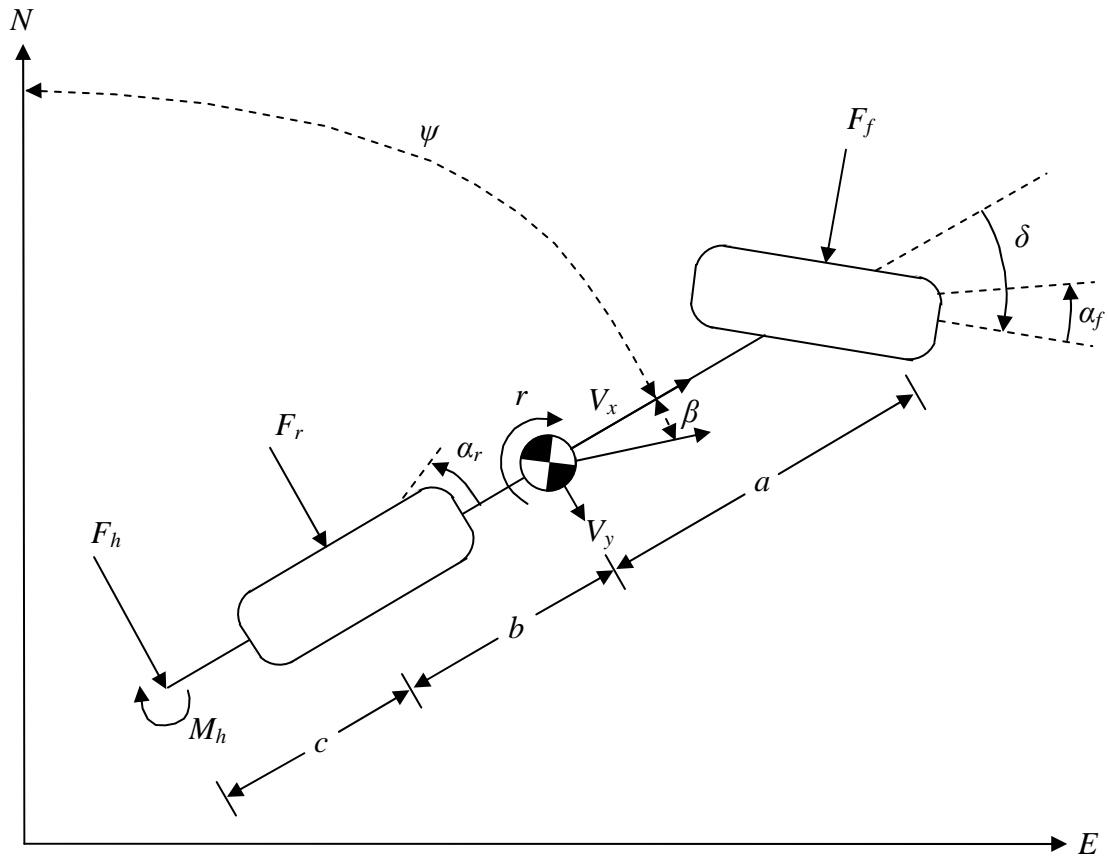


Figure 2.3: Bicycle model augmented with a hitch force and moment.

As can be seen in Figure 2.3, the force on the front tire, rear tire, and hitch are defined as F_f , F_r , and F_h respectively. The distance from the center of gravity to the front tire and rear tire are defined as a and b , and the distance from the rear tire to the hitch is

c. The front, rear, and hitch slip angles are defined as α_f , α_r , and α_h respectively. Also depicted in the figure are the longitudinal velocity (V_x), lateral velocity (V_y), yaw rate (r), and steer angle (δ). The heading angle (ψ) is the angle between the North direction (N) and the tractors longitudinal direction. The side slip (β) is the angle between the longitudinal and lateral velocities. The course angle (ν), the angle provided by GPS, is the heading angle (ψ) plus the side slip (β). The dynamics of the bicycle model in a state space representation are shown below.

$$\begin{bmatrix} \dot{V}_y \\ \dot{r} \end{bmatrix} = \begin{bmatrix} \frac{2(C_{\alpha h} + C_{\alpha r} + C_{\alpha f})}{mV_x} & \frac{2((b+c)C_{\alpha h} + bC_{\alpha r} - aC_{\alpha f})}{mV_x} - V_x \\ \frac{2((b+c)C_{\alpha h} + bC_{\alpha r} - aC_{\alpha f})}{I_z V_x} & \frac{2((b+c)^2 C_{\alpha h} + b^2 C_{\alpha r} + a^2 C_{\alpha f})}{I_z V_x} \end{bmatrix} \begin{bmatrix} V_y \\ r \end{bmatrix} + \begin{bmatrix} \frac{2C_{\alpha f}}{m} \\ \frac{2aC_{\alpha f}}{I_z} \end{bmatrix} \delta \quad (2.2)$$

The front, rear, and hitch cornering stiffnesses are $C_{\alpha f}$, $C_{\alpha r}$, and $C_{\alpha h}$ respectively. The cornering stiffnesses represent the resistance to turning and are a factor in computing the forces from the slip angles. The mass of the tractor is m and the mass moment of inertia about the vertical axis is I_z .

The bicycle model has two poles which decrease in bandwidth as velocity increases. Additionally, the bandwidth of the bicycle model goes to infinity as velocity goes to zero. However, it will be shown that the poles of the system identification model do not go to infinity as velocity decreases. Therefore this is not a good model for low velocities. Another model that has been used assumes that the lateral velocity is negligible which causes the bicycle model to collapse into a first order model. These models also have too few poles to describe what was obtained through system identification tests shown in the next section. It is believed, however, that the bicycle

model can provide an adequate description of how the DC gain changes with hitch loading [Pearson, 2005]. The DC gain equation for the bicycle model is shown below.

$$\frac{r_{ss}}{\delta_{ss}} = \frac{C_{\alpha f}[(a+b+c)C_{\alpha h} + (a+b)C_{\alpha r}]V_x}{(a+b)^2 C_{\alpha f} C_{\alpha r} + c^2 C_{\alpha r} C_{\alpha h} + (a+b+c)^2 C_{\alpha f} C_{\alpha h} + 0.5m[(b+c)C_{\alpha h} + bC_{\alpha r} - aC_{\alpha f}]V_x^2} \quad (2.3)$$

This equation can be condensed to Equation (2.4), where K_2 , the understeer [Gillespie, 1992] component, is typically much smaller than K_1 .

$$\frac{r}{\delta} = \frac{V_x}{K_1 + K_2 V_x^2} \quad (2.4)$$

K_2 being much smaller causes the steady state relationship between steer angle and rate to be linear at low velocities with an intercept of zero and begin curving at higher velocities. As will be seen from experimental data, the velocity range of interest does indeed produce linear fits. Therefore, the term K_2 can be neglected in the estimation scheme.

A bicycle model with tire relaxations for a tractor without an implement has been used to improve the bicycle model for low velocities [Owen, 1982]. The relaxation length causes a lag in the production of the slip angle generating the tire force. The addition of the tire relaxation lengths to the bicycle model adds two poles to the system and maintains the same DC gain equation. In Equation (2.5), the bicycle model with front and rear tire relaxation lengths (σ_f and σ_r) is presented with the hitch modeled as a cornering stiffness.

$$\begin{bmatrix} \dot{V}_y \\ \dot{r} \\ \dot{\alpha}_f \\ \dot{\alpha}_r \end{bmatrix} = \begin{bmatrix} -\frac{2C_{\alpha h}}{mV_x} & \frac{2(b+c)C_{\alpha h}}{mV_x} - V_x & \frac{2C_{\alpha f}}{m} & \frac{2C_{\alpha r}}{m} \\ \frac{2(b+c)C_{\alpha h}}{I_z V_x} & -\frac{2(b+c)^2 C_{\alpha h}}{I_z V_x} & \frac{2aC_{\alpha f}}{I_z} & -\frac{2bC_{\alpha r}}{I_z} \\ -\frac{1}{\sigma_f} & -\frac{a}{\sigma_f} & -\frac{V_x}{\sigma_f} & 0 \\ -\frac{1}{\sigma_r} & \frac{b}{\sigma_r} & 0 & -\frac{V_x}{\sigma_r} \end{bmatrix} \begin{bmatrix} V_y \\ r \\ \alpha_f \\ \alpha_r \end{bmatrix} + \begin{bmatrix} 0 \\ 0 \\ \frac{V_x}{\sigma_f} \\ 0 \end{bmatrix} \delta \quad (2.5)$$

This model has four poles and two zeros, with the dominant poles no longer going to infinity as velocity decreases. The addition of relaxation lengths has been used to control farm tractors at high velocities [Bevly, 2001]. In that research it was assumed that the four poles and two zeros from the model were of similar bandwidth. Therefore the resulting frequency response contained only one resonant peak.

There are relatively few system identifications of farm tractors in the literature and none were found which provided more than one hertz of excitation. Therefore, no previous work could be compared to the system identifications for the dynamics found above one hertz.

2.4 8420 Tractor Yaw Dynamics

For the system identification of the tractor, chirp inputs were used on a road with no implement and in a field with a four shank ripper at three different depths. In Figure 2.4, a comparison of the ETFE and Box Jenkins fits shows that the transfer function from steer angle to yaw rate had four poles and three zeros.

The location of the four poles is clearly seen by the two resonant peaks in Figure 2.4. The three zeros are found between the two sets of poles, and one of the zeros is non-

minimum phase which is why the second resonant peak is so high and the phase goes to -270 degrees.

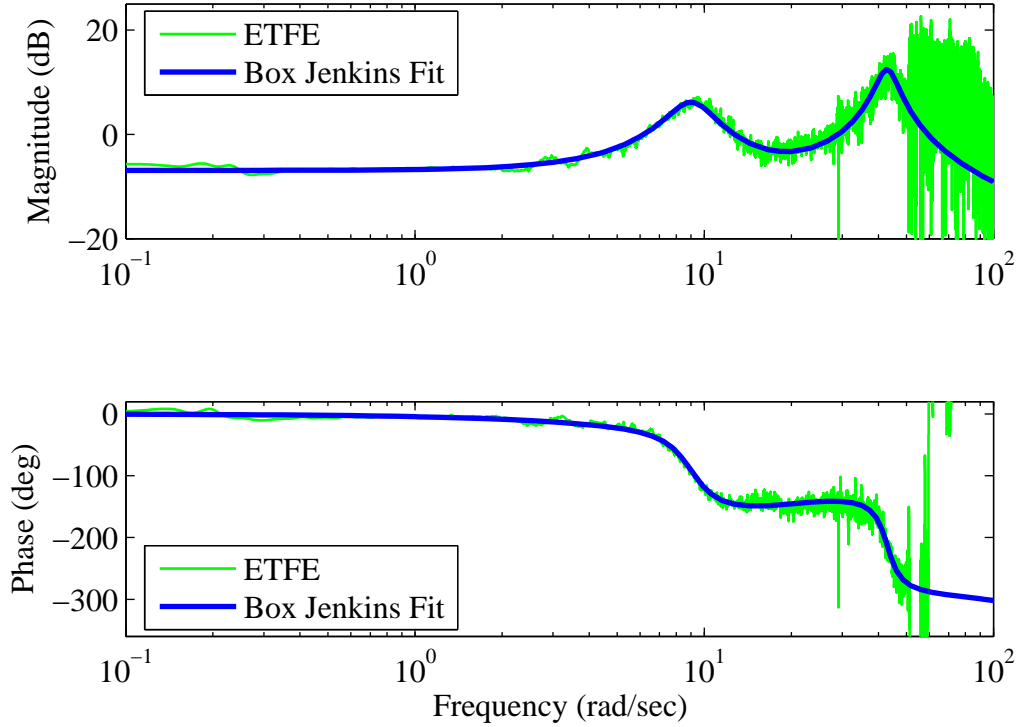


Figure 2.4: Comparison of ETFE and Box Jenkins Fits.

From the comparison of an ETFE and Box Jenkins Fit of experimental data the tractor was found to have four poles and three zeros, which means that the model in Equation (2.5) is not even adequate for describing the system.

It may be possible that the poles and zeros of the bicycle model with relaxation lengths are not lumped into the first resonance of Figure 2.4 and there is only a slight adjustment needed to this model to add a zero without majorly changing the DC characteristics of the model. Because the focus of this work is on the control of the

tractor, system identification fits provide adequate information, without fitting them to a known model.

In Figure 2.5, a comparison of the DC gain of the identified transfer functions shows that the DC gain is linear through the velocities of interest.

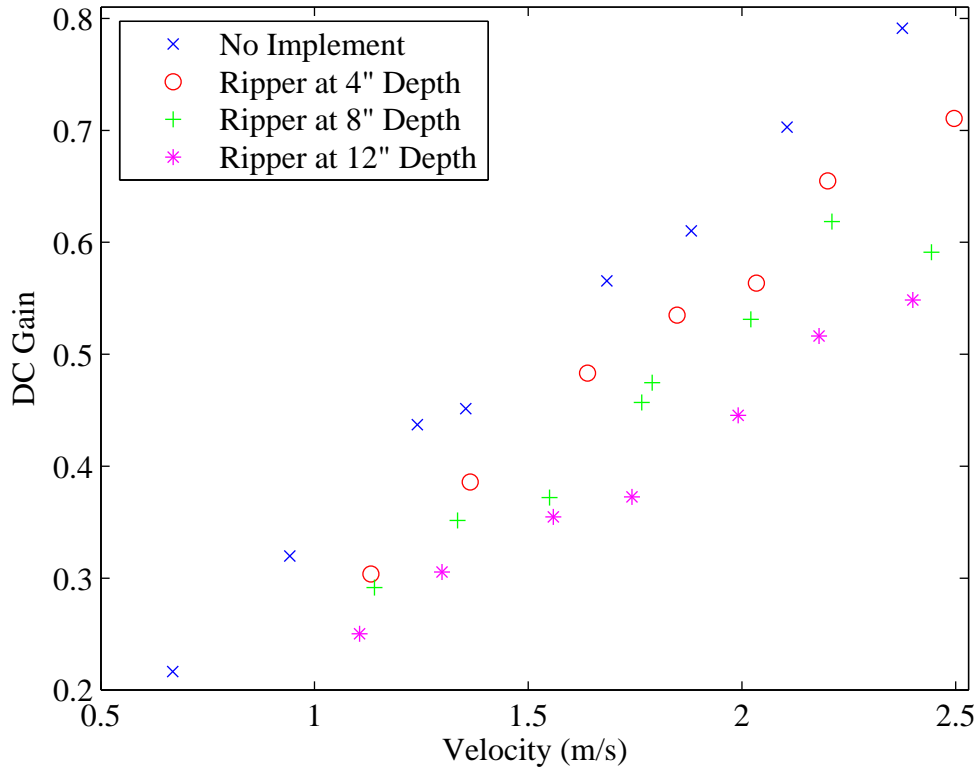


Figure 2.5: Experimental fits of DC gain.

Table 2.2 provides fits of the DC gains identified, which produced intercepts that were close to zero. This provides further evidence that the understeer of the tractor does not affect the linearity of the DC gain in the velocities of interest. Therefore the estimator introduced in Chapter 4 can simply estimate the slope of the DC gain to characterize the tractors steady state handling on-line.

Table 2.2: DC Gain Linear Fits

DC Gain = Slope*Velocity				
	Baseline	4" depth	8" depth	12" depth
Slope	0.334	0.284	0.258	0.227
DC Gain = Slope*Velocity + Intercept				
	Baseline	4" depth	8" depth	12" depth
Slope	0.329	0.298	0.259	0.231
Intercept	0.00800	0.0222	0.00153	0.00616

As seen in Figure 2.6, the dominant poles of the system, did not contain as clear of trends as the DC gain. Linear fits for the natural frequency with no implement appear to decrease slightly with velocity while, with the ripper they appear to increase with velocity. However, with the ripper the fits are not as clean. For this reason, the natural frequency was chosen to be constant at each depth regardless of velocity since this is a good approximation for the tractor with no implement.

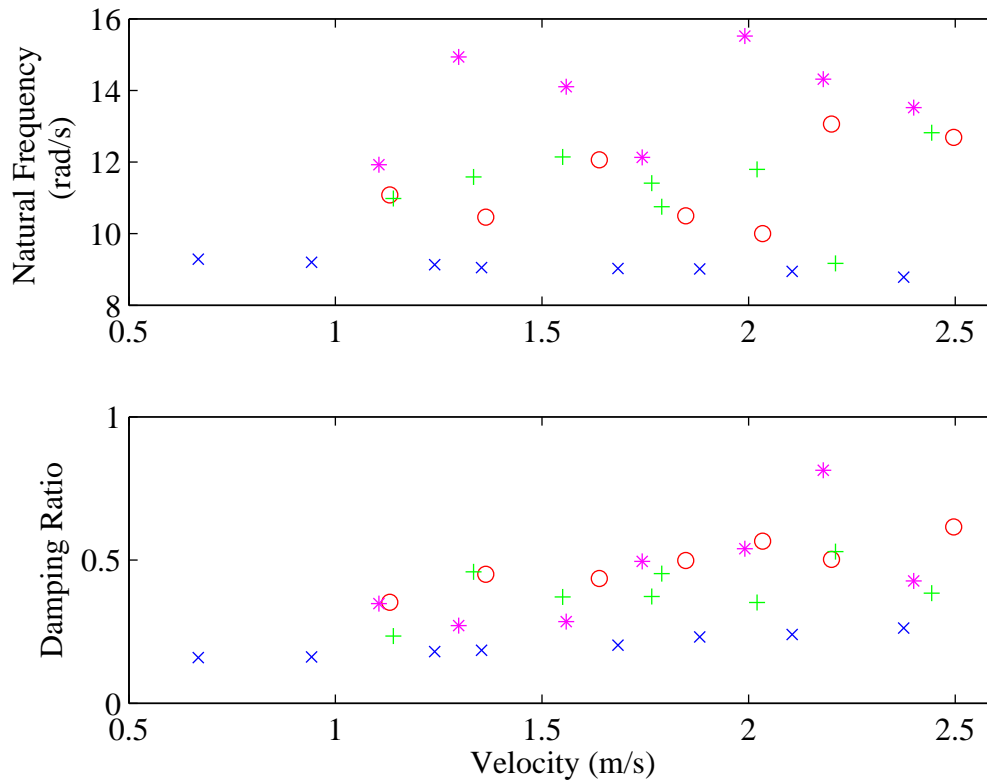


Figure 2.6: Experimental fits of the dominant poles. (x = baseline tractor, o = 4 shank ripper at 4” depth, + = 4 shank ripper at 8” depth, * = 4 shank ripper at 12” depth)

With an implement the dominant poles have considerably more damping; however, it was not clear how the damping changes between hitch loadings. Therefore, for the design of the controller, the damping was chosen as a linear fit for no implement and a separate linear fit with an implement that was the same for all depths.

The remainder of the poles and zeros are displayed in Figures 2.7-2.9. Due to the noise in the fits with an implement it is not clear as to how the natural frequency and damping changes with implement depth. However most of these vary only slightly from what is obtained with no implement. Since these values will have a lesser effect on the

design of the controller, as they are at higher natural frequencies, they were modeled as the same as with no implement in the design of the controller.

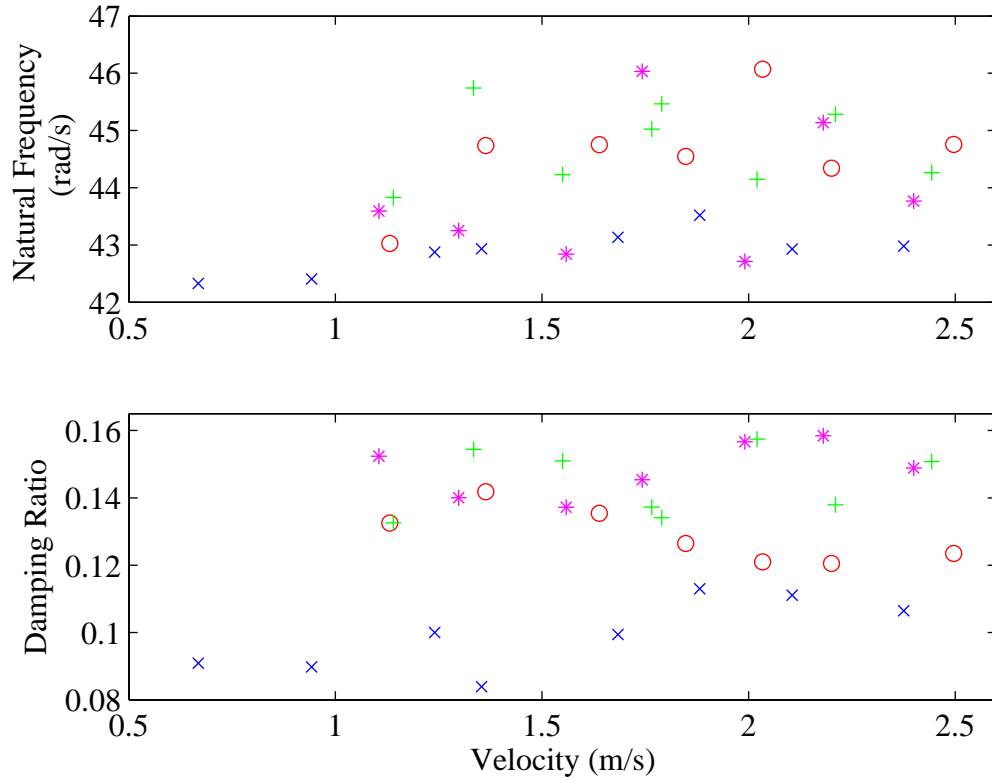


Figure 2.7: Experimental fits of the secondary poles. (x = baseline tractor, o = 4 shank ripper at 4" depth, + = 4 shank ripper at 8" depth, * = 4 shank ripper at 12" depth)

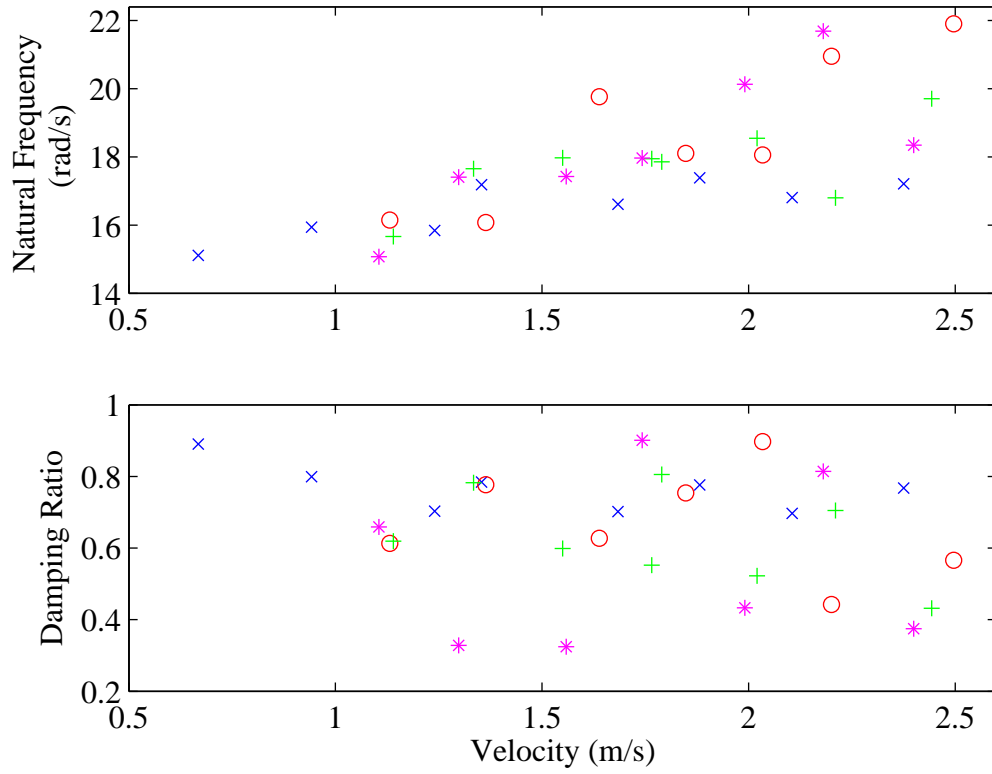


Figure 2.8: Experimental fits of the imaginary zeros. (x = baseline tractor, o = 4 shank ripper at 4" depth, + = 4 shank ripper at 8" depth, * = 4 shank ripper at 12" depth)

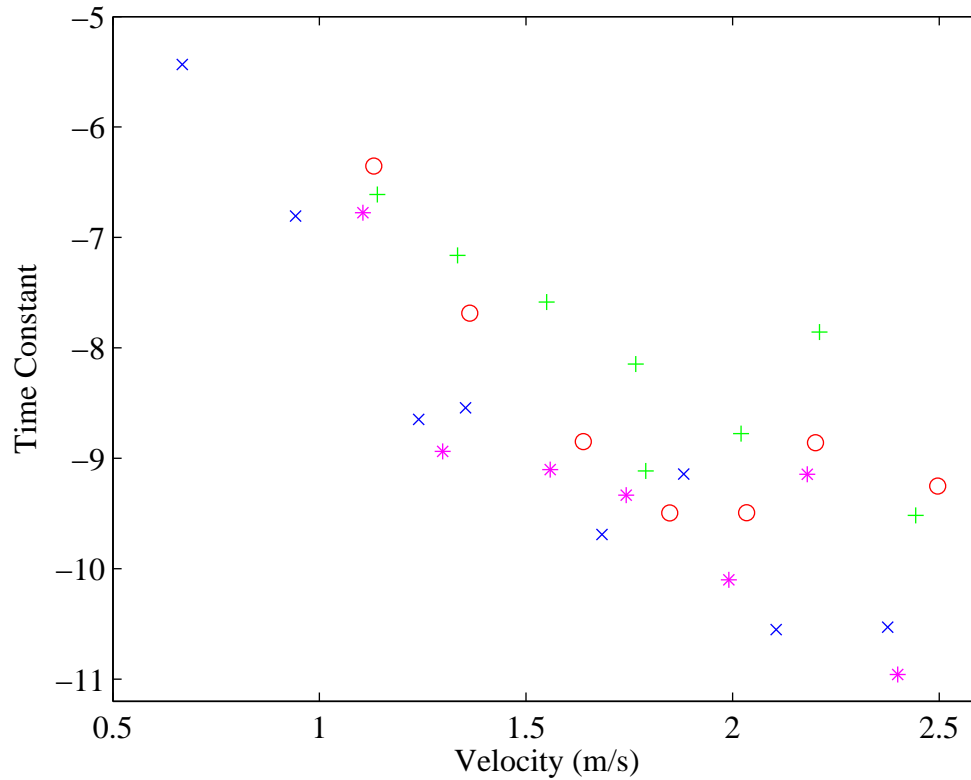


Figure 2.9: Experimental fits of the right half plane zero time constant. (x = baseline tractor, o = 4 shank ripper at 4" depth, + = 4 shank ripper at 8" depth, * = 4 shank ripper at 12" depth)

A summary of values used to model the tractor are given in Table 2.3. These values describe the continuous poles that were used in the design of the controllers in Chapter 3.

Table 2.3: Tractor Model Parameters

	No Implement	Ripper at 4'' Depth	Ripper at 8'' Depth	Ripper at 12'' Depth
M_{DC}	0.335	0.285	0.258	0.227
Dominant pole frequency	9	11	13	15
Dominant pole damping	$0.064V_x$ +0.10496	$0.1719V_x$ +0.1396		→
Secondary pole frequency	$0.46858V_x$ 42.17			→
Secondary pole damping	$0.013764V_x$ +0.078253			→
Imaginary zero frequency	$1.1276V_x$ 14.784			→
Imaginary zero damping	$-0.065439V_x$ +0.86505			→
Non-minimum phase zero time constant	$1.532V_x^2$ $-7.5414V_x$ -1.1705			→

2.5 Summary and Conclusions

A model of the steering servo was found which uses an input transformation, to account for its nonlinearities, and a transfer function. It was shown that previous tractor

models were inadequate in describing the tractor used in this research. Therefore a model based on system identification fits was developed. It was found that the DC gain from steer angle to yaw rate could simply be determined through the use of the slope of the DC gain. Finally, a table of the tractor model parameters was presented for use in the controller design.

CHAPTER 3

CASCADED CONTROLLER DESIGN AND ANALYSIS

3.1 Introduction

This chapter discusses the design of the cascaded controllers using the dynamics identified in Chapter 2. Also, the sensitivity of the closed loop systems to the model simplifications in Chapter 2 are discussed along with the effects the incorrect velocity and M_{DC} estimate in the design of the controller.

A block diagram of the cascaded controllers [Franklin, 2002] is displayed in Figure 3.1, where $G_{c1}(z)$, $G_{c2}(z)$, and $G_{c3}(z)$ are the controllers for the steering servo, yaw rate, and lateral position. $G_{p1}(z)$, $G_{p2}(z)$, and $G_{p3}(z)$ are the open loop dynamics of the steering servo, yaw rate, and lateral position. The values being fed back to the controllers are the steer angle, yaw rate, and lateral position.

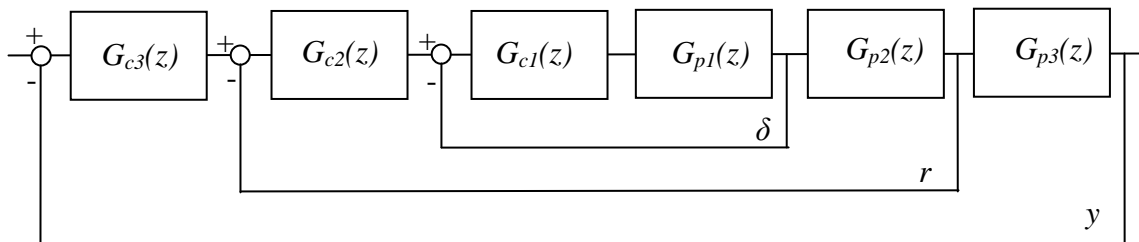


Figure 3.1: Block diagram of the controller system

3.2 Steering Servo Controller

The input to the tractor is the flow rate of the steering servo, which as discussed in Chapter 2 has been modeled as a third order system with input nonlinearities. To compensate for these nonlinearities, a transformation of the controller output has been used as shown in the block diagram in Figure 3.2. This transformation is generated by taking the inverse of the mapping of the steady state steering rate versus the command input shown previously in Figure 2.1.

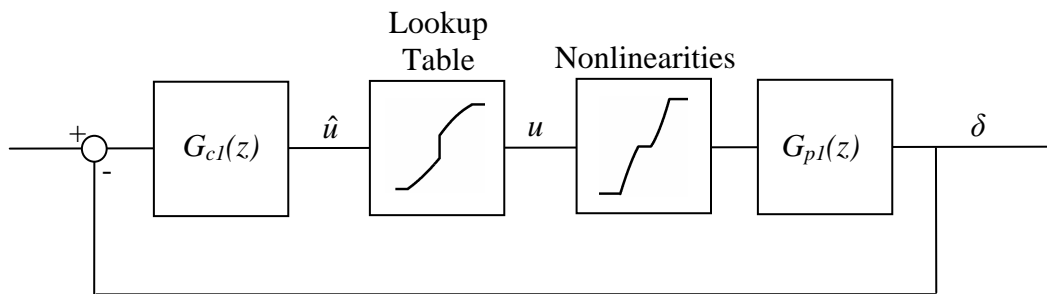


Figure 3.2: Block diagram of steering servo system

The equations for the inverse mapping of the steering servo nonlinearities are given in Table 3.1. The inverse mapping effectively linearizes the system such that classical design techniques can be used for the design of the steering servo controller.

Table 3.1: Inverse mapping of steady state steering rate versus command value

Input to plant	Range of \hat{u} for function
$u = 598$	$\hat{u} < -0.36$
$u = 518.7\hat{u}^2 + 920.2\hat{u} + 864.4$	$\hat{u} \geq -0.36 \ \& \ \hat{u} < 0$
$u = -887.9\hat{u}^2 + 1045\hat{u} + 1059$	$\hat{u} \geq 0 \ \& \ \hat{u} < 0.36$
$u = 1325$	$\hat{u} \geq 0.36$

Since the input frequency to the tractor is at 50 hertz and the identified transfer function for the steering servo given previously in Equation (2.1) is at 100 hertz, a discrete conversion [Franklin, 1998] was done leading to Equation (3.1).

$$\frac{\delta(z)}{u(z)} = \frac{b_2 z + b_3}{z^3 + a_1 z^2 + a_2 z + a_3} \quad (3.1)$$

The discrete conversion adds a zero to the transfer function that is located close to minus one inside of the discrete unit circle.

A constant proportional control law was used for the steering servo control loop. This results in a closed loop with three poles. The decision on modeling the controller as a proportional gain was made because the steering dynamics already was an integrator in the plant and it reduced the number of poles in the design of the yaw rate and position controllers. Equation (3.2) gives the polynomials of the closed loop denominator used in the controller design.

$$B(z) = (z + e_1)(z^2 + f_1 z + f_2) \quad (3.2)$$

The first order polynomial contains the pole that can be placed by the controller. The second order polynomial contains the poles that can not be placed because the controller only allows the placement of one variable.

The system of equations that must be solved to place the desired pole is shown in Equation (3.3), where s_0 is the proportional controller gain.

$$\begin{bmatrix} 0 & -1 & 0 \\ b_2 & -e_1 & -1 \\ b_3 & 0 & -e_1 \end{bmatrix} \begin{bmatrix} s_0 \\ f_1 \\ f_2 \end{bmatrix} = \begin{bmatrix} e_1 - a_1 \\ -a_2 \\ -a_3 \end{bmatrix} \quad (3.3)$$

Also, solving for this equation allows for the set of poles that have not been placed to be checked to make sure that they don't interfere with the desired closed loop dominant pole. The closed loop system in Equation (3.4) then can then be used in to the design of the yaw rate and position controllers.

$$\frac{\delta(z)}{\delta_{des}(z)} = \frac{s_0(b_2z + b_3)}{z^3 + a_1z^2 + a_2z + a_3 + s_0(b_2z + b_3)} \quad (3.4)$$

3.3 Yaw Rate Controller

A set of yaw rate controllers were designed for each of the yaw rate models given previously in Table 2.3, as a function of velocity. Fourth order curve fits of each set were then found so that upon the estimation of M_{DC} it could be determined what controller values to use through interpolation. In order to design the individual points for the fit, the damping and natural frequency of the poles and zeros were calculated from Table 2.3 based on the velocity for each value of M_{DC} . This led to a transfer function that when converted to 50 Hz led to Equation (3.5) which could be used to calculate the controller values for that velocity and M_{DC} .

$$\frac{r(z)}{\delta(z)} = \frac{\bar{b}_1 z^3 + \bar{b}_2 z^2 + \bar{b}_3 z + \bar{b}_4}{z^4 + \bar{a}_1 z^3 + \bar{a}_2 z^2 + \bar{a}_3 z + \bar{a}_4} \quad (3.5)$$

The transfer function from steer angle to yaw rate (Equation (3.5)) was then multiplied by the closed loop steering servo (Equation (3.4)) producing the open loop yaw rate system, shown below in Equation (3.6).

$$\begin{aligned} \frac{r(z)}{\delta_{des}(z)} &= \frac{s_0(b_2 z + b_3)}{z^3 + a_1 z^2 + a_2 z + a_3 + s_0(b_2 z + b_3)} \cdot \frac{\bar{b}_1 z^3 + \bar{b}_2 z^2 + \bar{b}_3 z + \bar{b}_4}{z^4 + \bar{a}_1 z^3 + \bar{a}_2 z^2 + \bar{a}_3 z + \bar{a}_4} \\ &= \frac{\hat{b}_3 z^4 + \hat{b}_4 z^3 + \hat{b}_5 z^2 + \hat{b}_6 z + \hat{b}_7}{z^7 + \hat{a}_1 z^6 + \hat{a}_2 z^5 + \hat{a}_3 z^4 + \hat{a}_4 z^3 + \hat{a}_5 z^2 + \hat{a}_6 z + \hat{a}_7} \end{aligned} \quad (3.6)$$

The yaw rate controller was chosen to be a lag controller [Ogata, 1998] consisting of a pole and no zero as shown below.

$$\frac{\delta_{des}}{e_r} = \frac{\hat{s}_1}{z + \hat{r}_1} \quad (3.7)$$

This was primarily done to mitigate the effect of the second resonant peak that was identified in Figure 2.3. It was also done in order to prevent a non-minimum phase zero being placed during the design process, which tended to occur when designing for larger values of M_{DC} . This would have caused complications in the design of the position controller.

Since the controller has two design variables, the location of two closed-loop poles can be selected. Equation (3.8) shows the closed loop denominator, which contains the second order polynomial of the poles that can be selected and the sixth order polynomial of the remaining closed loop poles.

$$\hat{B}(z) = (z^2 + \hat{e}_1 z + \hat{e}_2) (z^6 + \hat{f}_1 z^5 + \hat{f}_2 z^4 + \hat{f}_3 z^3 + z^2 \hat{f}_4 + z \hat{f}_5 + \hat{f}_6) \quad (3.8)$$

By calculating the denominator from Equations (3.6) and (3.7) and setting that equal to Equation (3.8), leads to the set of equations in Equation (3.9) to be solved for to obtain the controller values.

$$\begin{bmatrix} 1 & 0 & -1 & 0 & 0 & 0 & 0 & 0 \\ \hat{a}_1 & 0 & -\hat{e}_1 & -1 & 0 & 0 & 0 & 0 \\ \hat{a}_2 & 0 & -\hat{e}_2 & -\hat{e}_1 & -1 & 0 & 0 & 0 \\ \hat{a}_3 & \hat{b}_3 & 0 & -\hat{e}_2 & -\hat{e}_1 & -1 & 0 & 0 \\ \hat{a}_4 & \hat{b}_4 & 0 & 0 & -\hat{e}_2 & -\hat{e}_1 & -1 & 0 \\ \hat{a}_5 & \hat{b}_5 & 0 & 0 & 0 & -\hat{e}_2 & -\hat{e}_1 & -1 \\ \hat{a}_6 & \hat{b}_6 & 0 & 0 & 0 & 0 & -\hat{e}_2 & -\hat{e}_1 \\ \hat{a}_7 & \hat{b}_7 & 0 & 0 & 0 & 0 & 0 & -\hat{e}_2 \end{bmatrix} \begin{bmatrix} \hat{r}_1 \\ \hat{s}_1 \\ \hat{f}_1 \\ \hat{f}_2 \\ \hat{f}_3 \\ \hat{f}_4 \\ \hat{f}_5 \\ \hat{f}_6 \end{bmatrix} = \begin{bmatrix} \hat{e}_1 - \hat{a}_1 \\ \hat{e}_2 - \hat{a}_2 \\ -\hat{a}_3 \\ -\hat{a}_4 \\ -\hat{a}_5 \\ -\hat{a}_6 \\ -\hat{a}_7 \\ 0 \end{bmatrix} \quad (3.9)$$

Solving for Equation (3.9) can also determine if any of the remaining poles would cause the system to be unstable.

The controller values were calculated for various velocities for each of the yaw rate models in Table 2.3. The trends in the controller values could then be seen as a function of hitch loading. Figures 3.3 and 3.4 show how the controller values varied for the various yaw rate models.

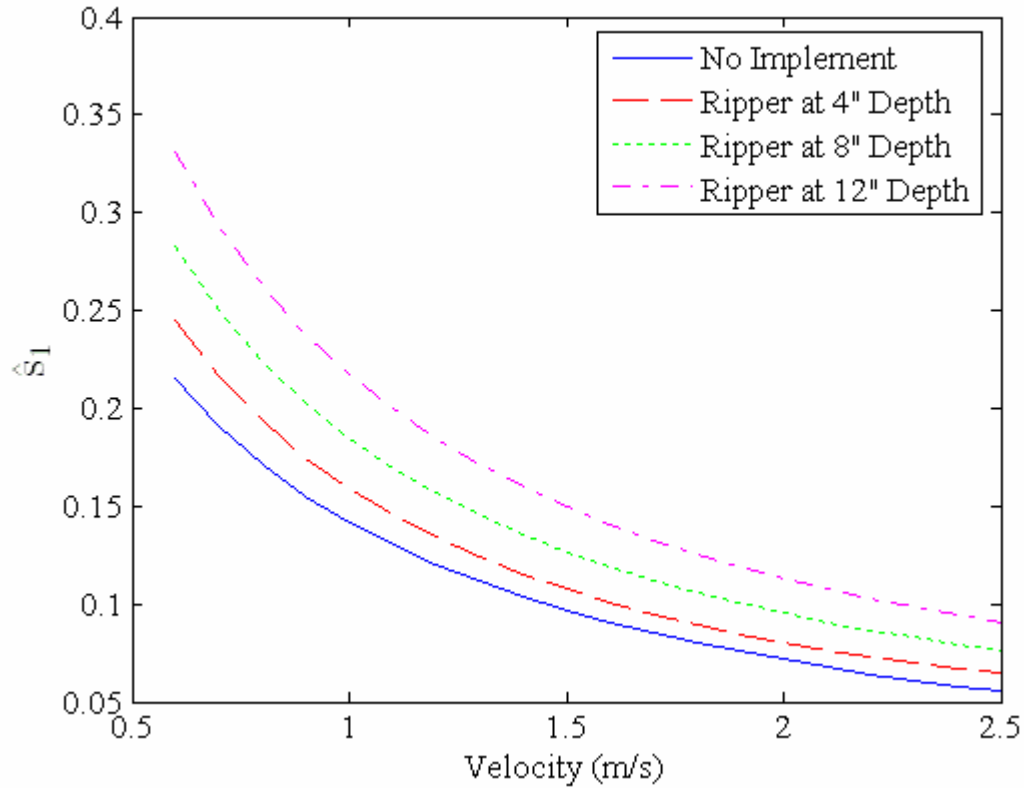


Figure 3.3: \hat{s}_1 versus velocity for each yaw model

As seen in Figure 3.3 the variation due to the implement simply shifts the curve down. However, in Figure 3.4 there is a more significant difference in the trend of the curves. Also, there is a less of a percentage difference between the curves in Figure 3.4 than there is in Figure 3.3.

As stated previously, fourth order fits were used for of the curves. Since each of these curves has a known M_{DC} value related to it, the controller gains could then be calculated through interpolation using an estimated value of M_{DC} . In Table 3.2, the curve fits used for the interpolations are listed according to the yaw rate controller variable.

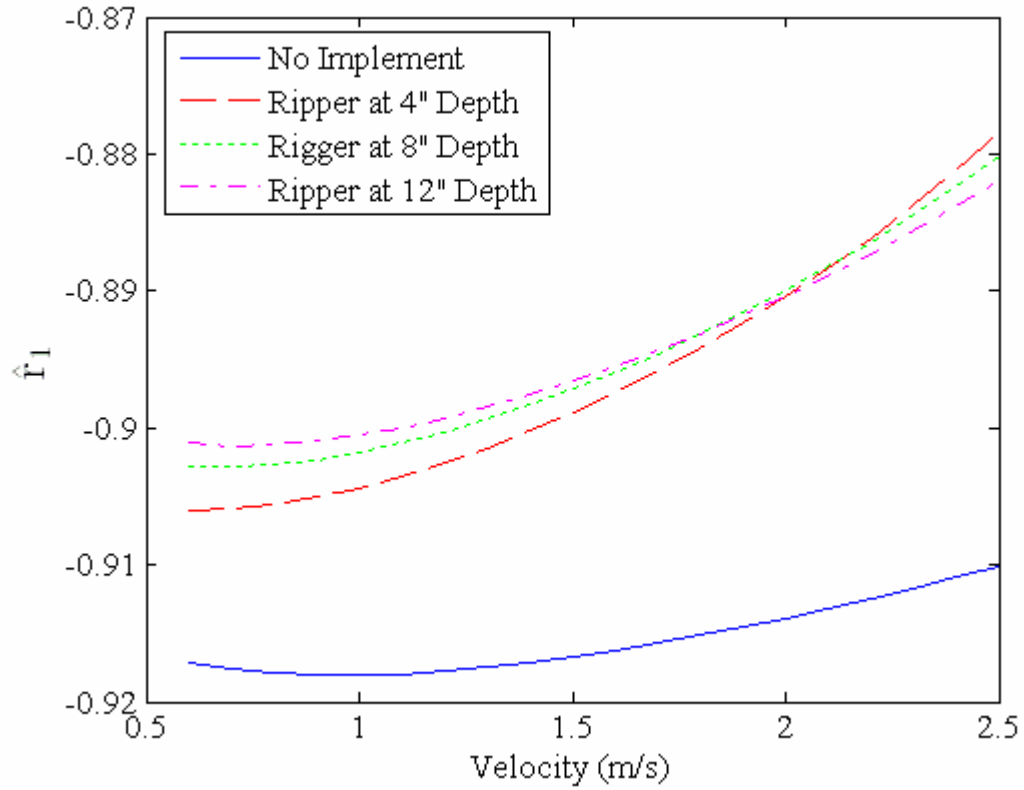


Figure 3.4: \hat{r}_1 versus velocity for each model

Table 3.2: Yaw rate controller values (variable = $g_0V^4 + g_1V^3 + g_2V^2 + g_3V + g_4$)

Values for \hat{s}_0					
M_{DC}	g_0	g_1	g_2	g_3	g_4
0.355	0.016544	-0.12928	0.39308	-0.59242	0.45384
0.285	0.020274	-0.15792	0.47963	-0.7158	0.53252
0.258	0.02307	-0.17972	0.54481	-0.81169	0.60811
0.227	0.02681	-0.20882	0.63224	-0.94108	0.70793

Values for \hat{r}_0					
M_{DC}	g_0	g_1	g_2	g_3	g_4
0.355	0.00069355	-0.0054523	0.017887	-0.021717	-0.90949
0.285	0.0010538	-0.0066872	0.021571	-0.019729	-0.9006
0.258	0.00093468	-0.006382	0.020994	-0.020493	-0.89685
0.227	0.00088336	-0.0063049	0.020818	-0.021387	-0.89455

3.4 Closed Loop Yaw Rate Sensitivity

To examine the how the accuracy of the M_{DC} estimate (developed in Chapter 4) will effect the phase and gain margins of the yaw rate controller, a frequency domain analysis using the system identification models and the previously described controller adaptation was conducted. The values of M_{DC} were assumed to be known exactly and within ten percent of the actual value.

Figure 3.5 shows the results of the bodes that were obtained with no implement. In the figure, the closed loop poles are at 4 rad/s which is before the first resonant peak that can be seen in the magnitude graph. Recall that if this resonant peak crossed 0 dB then the system is unstable. Fortunately, it decreases as velocity increases, ensuring the system is stable with increasing velocity.

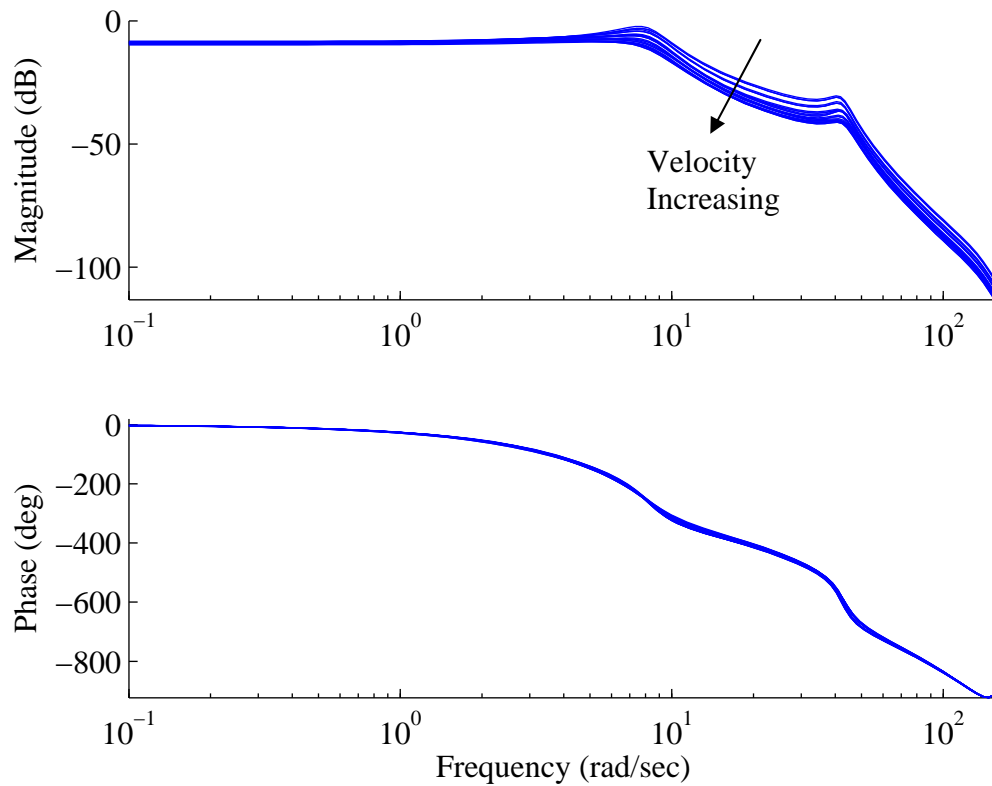


Figure 3.5: Sensitivity of yaw rate closed loop for no implement

The cause of the resonant peak can be seen more clearly in the root locus of the closed loop system. Figure 3.6 demonstrates that after the dominant poles there are a set of poles which have little damping. Recall that the yaw controller selected could only specify the location of two poles. Therefore these additional poles are not constrained to a specified location.

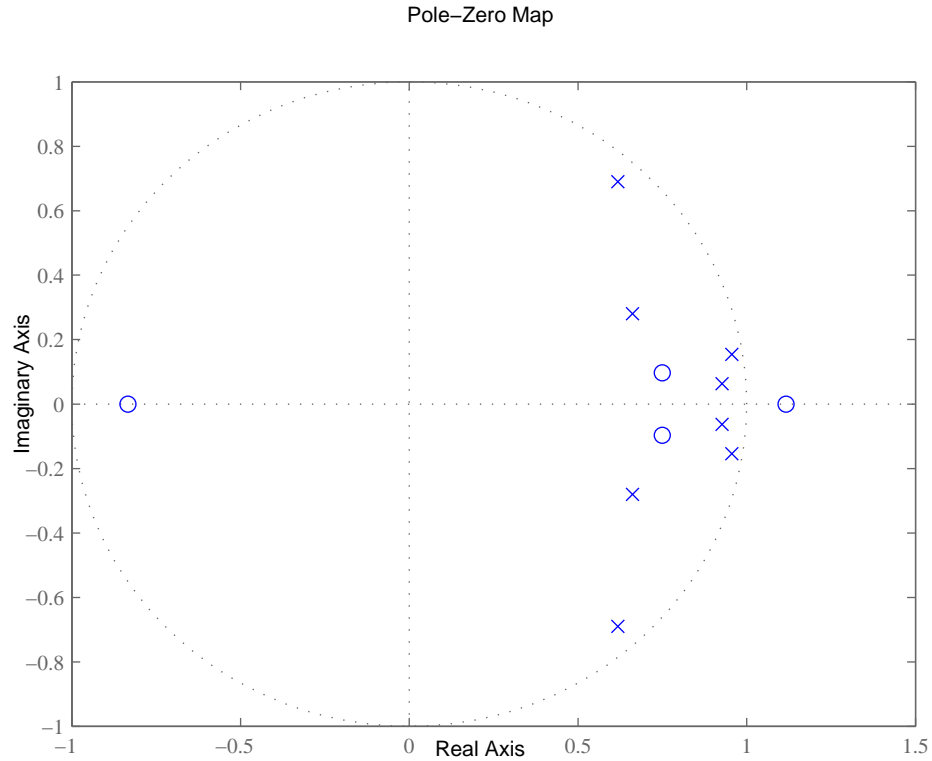


Figure 3.6: Root locus of closed loop yaw rate.

Figure 3.7 shows the closed loop bode for the tractor with an implement at all of the depths. Note that the resonant peak with the implement is not nearly as pronounced as in Figure 3.5. It looks like it could exist on a couple of lines, but these are believed to be bad fits, since that Box-Jenkins fit did not match the ETFE well. The DC portion of the bode also looks thicker than that of the frequency response without an implement. This is most likely due to the fact that the fits are better for the system identification tests without an implement.

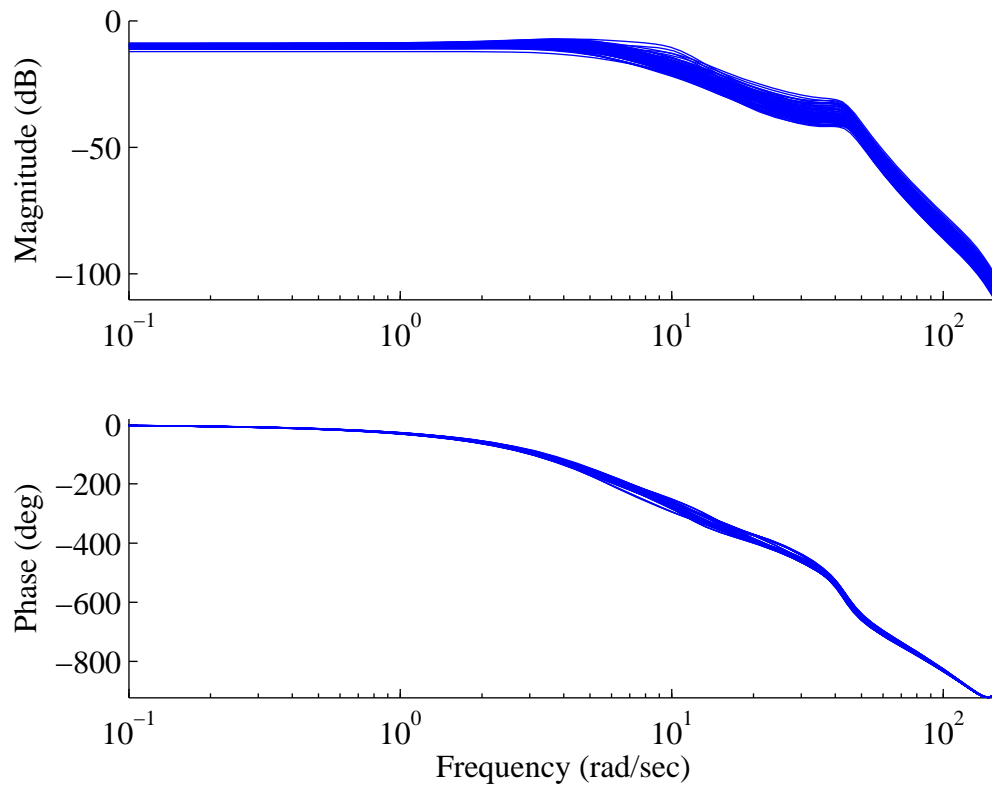


Figure 3.7: Sensitivity of yaw rate closed loop with an implement

For all of the cases tested varying M_{DC} the controller was found to be stable. Table 3.3 shows the maximum, minimum, mean, and standard deviation of gain margin for the various hitch loadings. As seen in the table, the mean gain margin appears increase as the implement hitch loading increases. This is most likely caused by the unconstrained set of closed loop poles near the first resonant peak increasing in damping ratio as the hitch loading is increased. Note that all the cases investigated had infinite phase margin.

Table 3.3: Gain margin (dB) for yaw rate

	Maximum	Minimum	Mean	σ
No Implement	8.65	3.77	6.67	1.52
Ripper 4" Depth	14.09	8.93	11.63	1.40
Ripper 8" Depth	15.60	7.80	11.18	1.90
Ripper 12" Depth	15.00	8.89	12.44	1.51

Figure 3.8 shows that for a low value of M_{DC} used in the design of the control law design would cause the closed loop yaw rate to be unstable. Additionally, values of M_{DC} significantly greater than the actual value in the controller design can lead to degraded performance.

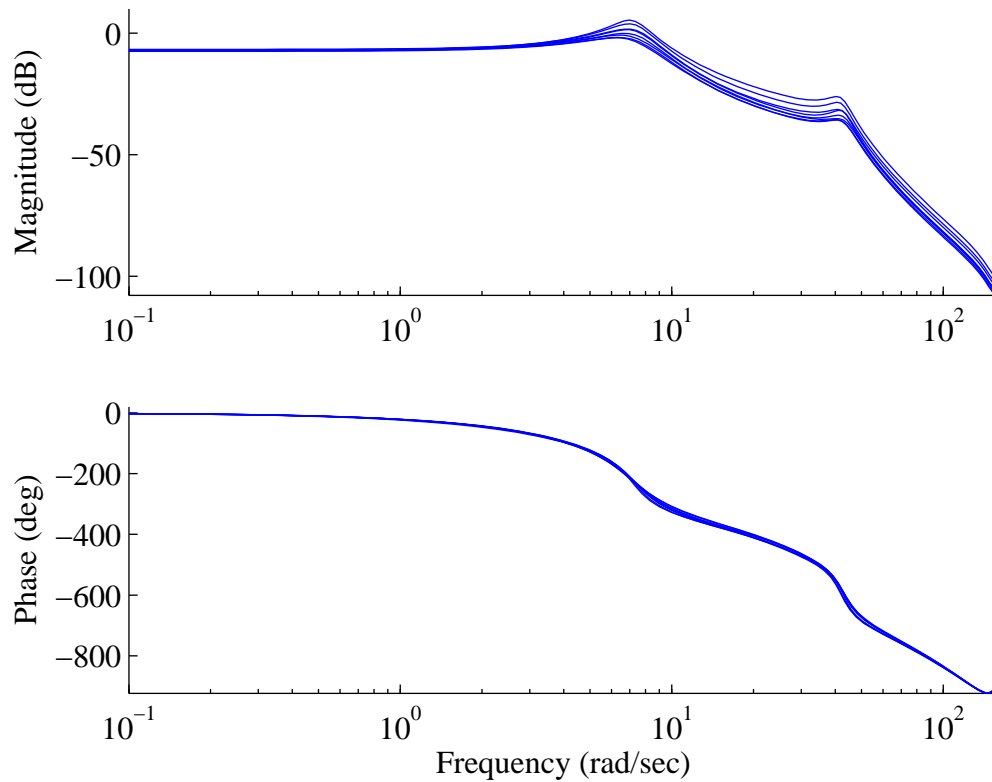


Figure 3.8: Sensitivity with no implement to too low M_{DC} .

Additionally, if the controller does not account for the changes in velocity it can cause the yaw rate controller to be unstable. Figure 3.9 shows the results of the controller being designed for 2 mph for all of the system identification models without an implement. Note that the magnitude crosses 0 dB after there has been -180 degrees of phase change for a number of models, indicating that the closed loop system is unstable. This instability was also seen using the system identification models with an implement.

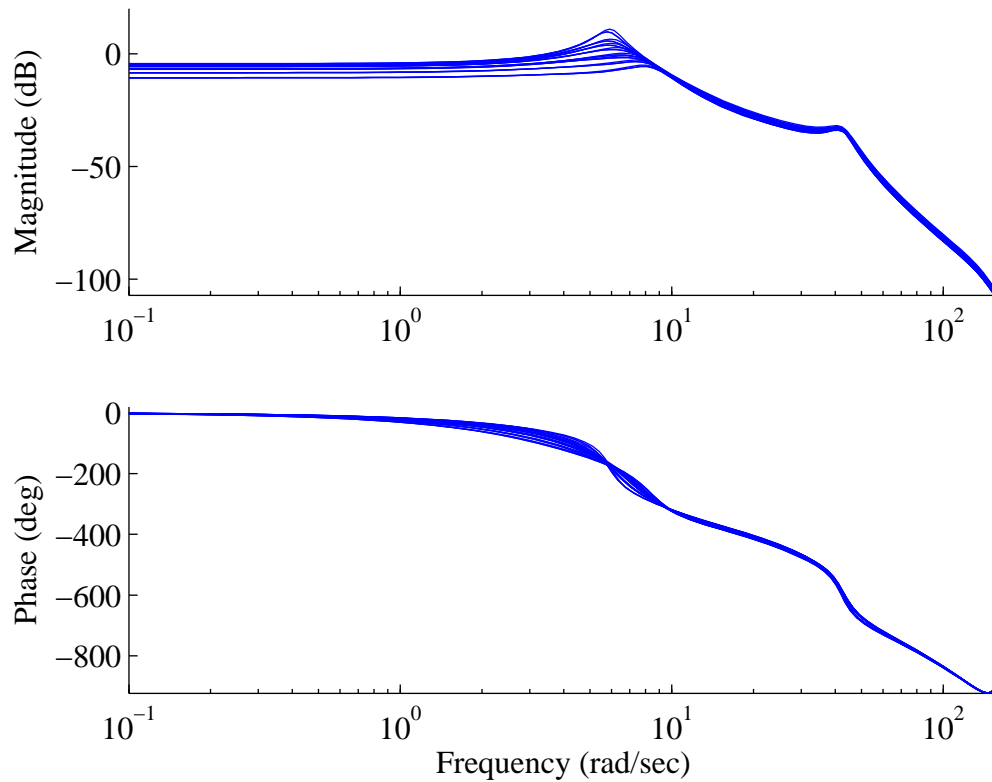


Figure 3.9: Sensitivity with no implement with 2 mph control gains.

When the controller was designed for a constant velocity of 5 mph the closed loop systems were stable for all hitch loadings identified as seen in Figure 3.10. However the performance of the controller was highly degraded since the system was at a lower bandwidth.

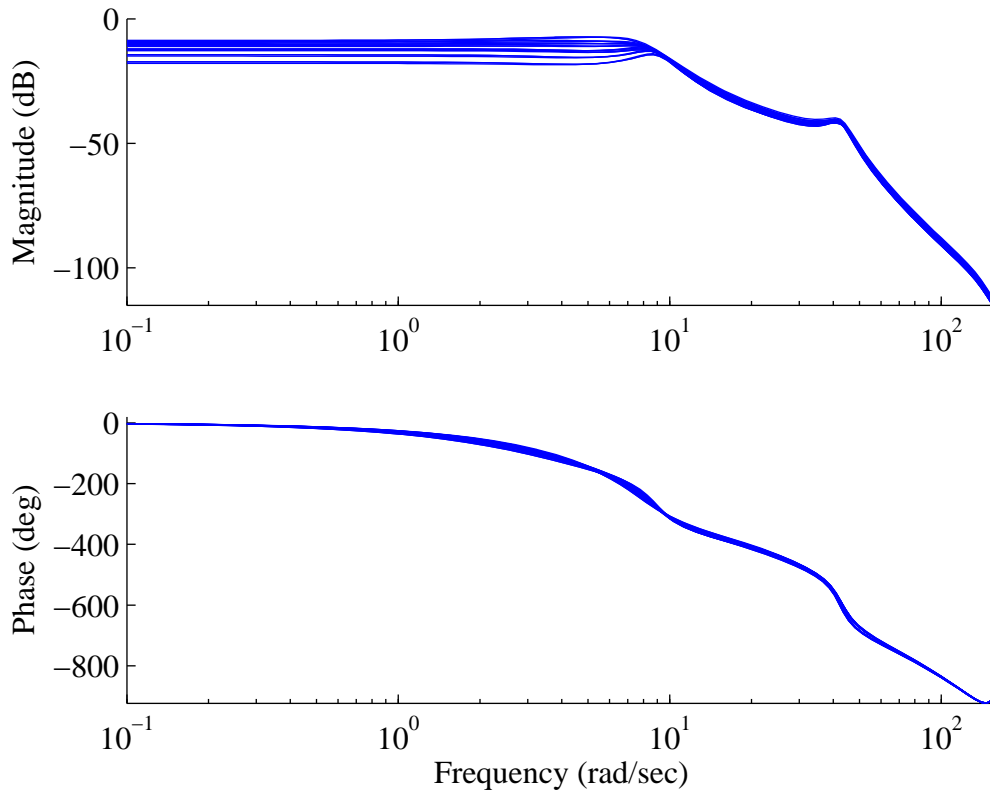


Figure 3.10: Sensitivity with no implement with 5 mph control gains.

3.5 Lateral Position Controller

The transfer function for lateral position used in the controller design was obtained from Equations (3.10) and (3.11).

$$\dot{y} = V_v \sin(\nu) \quad (3.10)$$

$$\dot{\nu} = r + \dot{\beta} \quad (3.11)$$

In Equation (3.10), the lateral velocity is defined as the total velocity times the sine of the course angle (which is taken with respect to the desired longitudinal direction). Equation (3.11) shows that the course angle is the integrated yaw rate plus side slip.

Neglecting the vehicle sideslip and linearizing about a small course angle, the Laplace transform of Equations (3.10) and (3.11) can be combined to produce the approximation shown below for lateral position.

$$y \approx \frac{V_y}{s^2} r \quad (3.12)$$

By discretizing the above equation, the following discrete transfer function between yaw rate and lateral position is obtained.

$$\frac{y(z)}{r(z)} = \frac{\tilde{b}_1 z + \tilde{b}_2}{z^2 - 2z + z} \quad (3.13)$$

The above transfer function can then be combined with the closed loop yaw rate transfer function, forming the open loop transfer function for lateral position shown below.

$$\frac{y(z)}{r_{des}(z)} = \frac{\tilde{b}_5 z^5 + \tilde{b}_6 z^4 + \tilde{b}_7 z^3 + \tilde{b}_8 z^2 + \tilde{b}_9 z + \tilde{b}_{10}}{z^{10} + \tilde{a}_1 z^9 + \tilde{a}_2 z^8 + \tilde{a}_3 z^7 + \tilde{a}_4 z^6 + \tilde{a}_5 z^5 + \tilde{a}_6 z^4 + \tilde{a}_7 z^3 + \tilde{a}_8 z^2 + \tilde{a}_9 z + \tilde{a}_{10}} \quad (3.14)$$

A simple lead control law with on zero and one pole was used for the lateral error controller as seen below.

$$\frac{r_{des}(z)}{e_y(z)} = \frac{\tilde{s}_0 z + \tilde{s}_1}{z + \tilde{r}_1} \quad (3.15)$$

Since there are three parameters in the controller, three poles of the closed loop system could be selected. Equation (3.16) shows the polynomials of the selected poles and the polynomial for the remaining poles of the closed loop transfer function denominator.

$$\tilde{B}(z) = (z^3 + \tilde{e}_1 z^2 + \tilde{e}_2 z + \tilde{e}_3) (z^8 + \tilde{f}_1 z^7 + \tilde{f}_2 z^6 + \tilde{f}_3 z^5 + \tilde{f}_4 z^4 + \tilde{f}_5 z^3 + \tilde{f}_6 z^2 + \tilde{f}_7 z + \tilde{f}_8) \quad (3.16)$$

The controller values can then solved for using Equation (3.17), which uses the values from Equations (3.14-3.16).

$$\begin{bmatrix}
1 & 0 & 0 & -1 & 0 & 0 & 0 & 0 & 0 & 0 & 0 \\
\tilde{a}_1 & 0 & 0 & -\tilde{e}_1 & -1 & 0 & 0 & 0 & 0 & 0 & 0 \\
\tilde{a}_2 & 0 & 0 & -\tilde{e}_2 & -\tilde{e}_1 & -1 & 0 & 0 & 0 & 0 & 0 \\
\tilde{a}_3 & 0 & 0 & -\tilde{e}_3 & -\tilde{e}_2 & -\tilde{e}_1 & -1 & 0 & 0 & 0 & 0 \\
\tilde{a}_4 & \tilde{b}_5 & 0 & 0 & -\tilde{e}_3 & -\tilde{e}_2 & -\tilde{e}_1 & -1 & 0 & 0 & 0 \\
\tilde{a}_5 & \tilde{b}_6 & \tilde{b}_5 & 0 & 0 & -\tilde{e}_3 & -\tilde{e}_2 & -\tilde{e}_1 & -1 & 0 & 0 \\
\tilde{a}_6 & \tilde{b}_7 & \tilde{b}_6 & 0 & 0 & 0 & -\tilde{e}_3 & -\tilde{e}_2 & -\tilde{e}_1 & -1 & 0 \\
\tilde{a}_7 & \tilde{b}_8 & \tilde{b}_7 & 0 & 0 & 0 & 0 & -\tilde{e}_3 & -\tilde{e}_2 & -\tilde{e}_1 & -1 \\
\tilde{a}_8 & \tilde{b}_9 & \tilde{b}_8 & 0 & 0 & 0 & 0 & 0 & -\tilde{e}_3 & -\tilde{e}_2 & -\tilde{e}_1 \\
\tilde{a}_9 & \tilde{b}_{10} & \tilde{b}_9 & 0 & 0 & 0 & 0 & 0 & 0 & -\tilde{e}_3 & -\tilde{e}_2 \\
\tilde{a}_{10} & 0 & \tilde{b}_{10} & 0 & 0 & 0 & 0 & 0 & 0 & 0 & -\tilde{e}_3
\end{bmatrix}
\begin{bmatrix}
\tilde{r}_1 \\
\tilde{s}_0 \\
\tilde{s}_1 \\
\tilde{f}_1 \\
\tilde{f}_2 \\
\tilde{f}_3 \\
\tilde{f}_4 \\
\tilde{f}_5 \\
\tilde{f}_6 \\
\tilde{f}_7 \\
\tilde{f}_8
\end{bmatrix}
=
\begin{bmatrix}
\tilde{e}_1 - \tilde{a}_1 \\
\tilde{e}_2 - \tilde{a}_2 \\
\tilde{e}_3 - \tilde{a}_3 \\
-\tilde{a}_4 \\
-\tilde{a}_5 \\
-\tilde{a}_6 \\
-\tilde{a}_7 \\
-\tilde{a}_8 \\
-\tilde{a}_9 \\
-\tilde{a}_{10} \\
0
\end{bmatrix} \quad (3.17)$$

Once the controller gains were determined for various velocities for each of the yaw rate models, the trends in the controller values as a function of hitch loading could be studied. Figures 3.11 and 3.12 show how the controller values varied gains vary with velocity and implement loading.

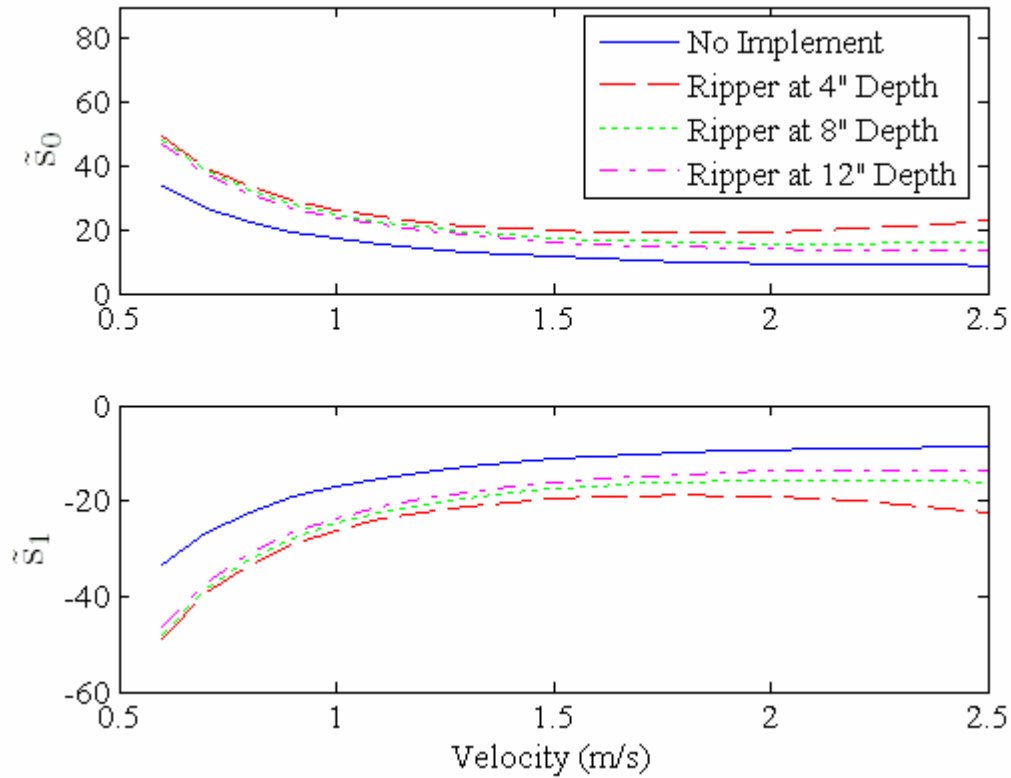


Figure 3.11: Controller values for various velocities and hitch loadings.

Like the yaw rate controller, fourth order fits were made for the controller gain curves shown in Figure 3.11 and 3.12. Each of these curves has a known M_{DC} value related to it, the controller gains could again be calculated through interpolation using an estimated value of M_{DC} . In Table 3.4, the curve fits used for the interpolations are listed according to the position controller variable.

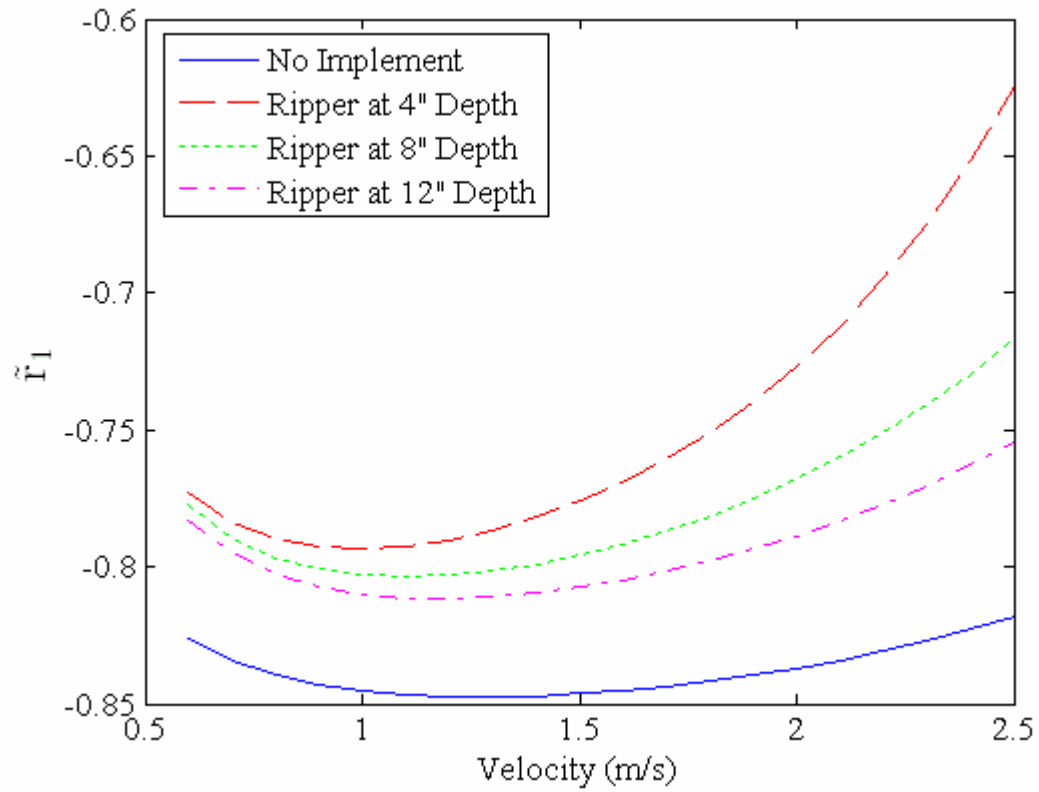


Figure 3.12: Controller values for various velocities and hitch loadings.

Table 3.4: Yaw rate controller values (variable = $g_0V^4 + g_1V^3 + g_2V^2 + g_3V + g_4$)

Values for \tilde{s}_0					
M_{DC}	g_0	g_1	g_2	g_3	g_4
0.355	8.0185	-58.726	161.18	-200.3	106.83
0.285	12.479	-89.378	242.36	-295.36	156.02
0.258	12.108	-88.024	240.09	-294.62	155.17
0.227	11.843	-86.358	235.71	-289.88	152.3

Values for \tilde{s}_1					
M_{DC}	g_0	g_1	g_2	g_3	g_4
0.355	-7.9577	58.281	-159.95	198.77	-106
0.285	-12.382	88.687	-240.48	293.07	-154.8
0.258	-12.014	87.34	-238.22	292.32	-153.94
0.227	-11.75	85.684	-233.87	287.6	-151.09
Values for \tilde{r}_1					
M_{DC}	g_0	g_1	g_2	g_3	g_4
0.355	0.011359	-0.080389	0.22571	-0.27599	-0.7263
0.285	0.028812	-0.17191	0.4395	-0.48022	-0.61013
0.258	0.019994	-0.13449	0.3703	-0.43411	-0.62486
0.227	0.017956	-0.12553	0.34986	-0.41878	-0.63368

3.6 Closed Loop Lateral Position Sensitivity

To examine the how the accuracy of the M_{DC} estimate effects the phase and gain margins of the position loop, a bode analysis using the system identification models and the previously described controller adaptation was again conducted. The values of M_{DC} were again assumed to be known exactly and within ten percent of the actual value.

Figure 3.13 shows the results of the bode plots that were obtained with. Note that in the figure the closed loop poles are at 1 rad/s.

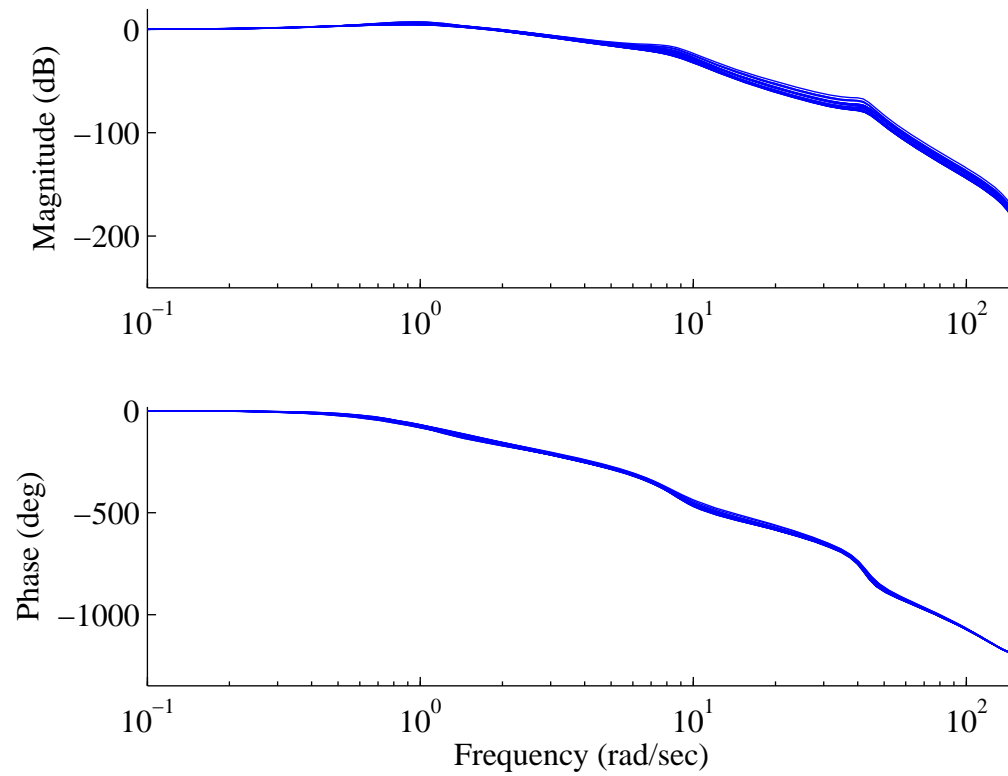


Figure 3.13: Sensitivity of lateral position closed loop for no implement

Figure 3.14 shows the results of the bode analysis with the varying M_{DC} when an implement is used. Unlike the results from the yaw rate analysis, the change in M_{DC} has very little change on the closed loop frequency response (with or without an implement).

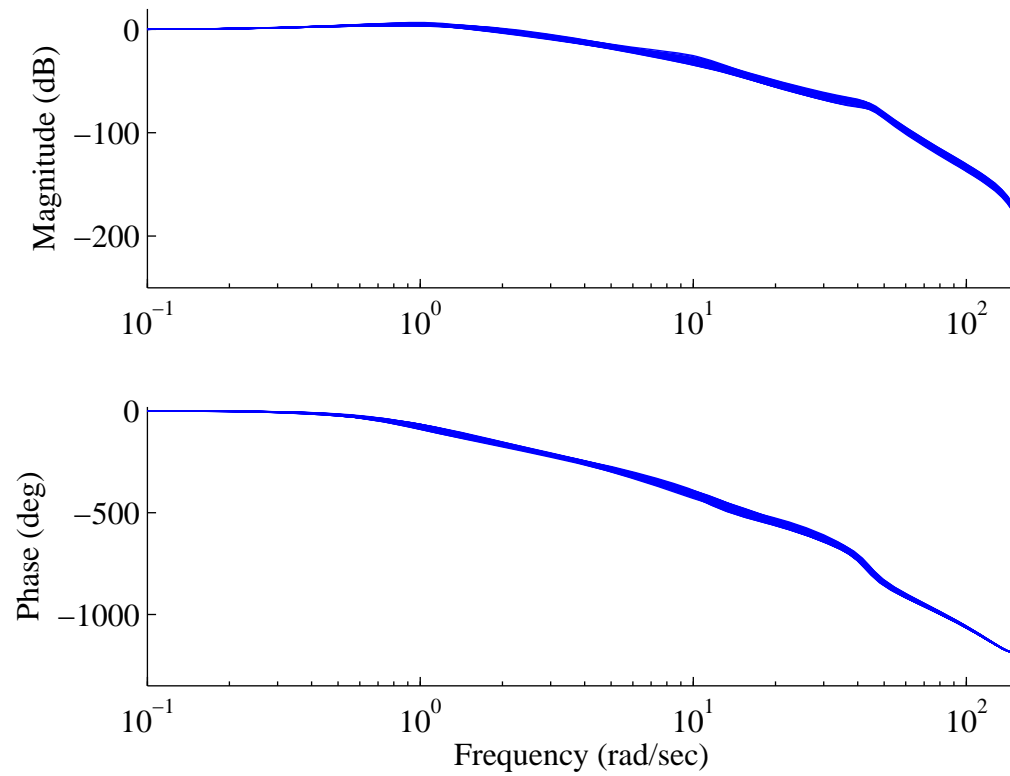


Figure 3.14: Sensitivity of lateral position closed loop with an implement

The gain margins for Figure 3.13 and 3.14 are shown in Table 3.5. Like the yaw rate controller, the gain margin for the position controller increases with hitch loading (which improves the stability of the controller).

Table 3.5: Gain margin (dB) for lateral position

	Maximum	Minimum	Mean	σ
No Implement	3.504	2.383	2.989	0.283
Ripper 4" Depth	3.654	1.434	2.469	0.638
Ripper 8" Depth	5.382	0.673	3.019	1.109
Ripper 12" Depth	5.158	2.563	3.745	0.726

The phase margins for Figure 3.13 and 3.14 are shown in Table 3.6, which also shows that the phase margin increases with hitch loading.

Table 3.6: Phase margin (deg) for lateral position

	Maximum	Minimum	Mean	σ
No Implement	30.963	20.332	26.221	3.436
Ripper 4" Depth	30.053	12.926	21.423	5.235
Ripper 8" Depth	38.202	7.421	26.594	7.693
Ripper 12" Depth	42.268	28.401	34.874	4.710

3.7 Summary and Conclusion

The controller for the steering servo using a transformation for the nonlinearities was designed. The yaw rate and position controllers were also designed using the system identification models from Chapter 2. Information was also provided on how the controller gains would be adapted through the estimation of M_{DC} . The method involves interpolating the control gain curve fits for various values of M_{DC} . The sensitivity of the

closed loop system was investigated for the values of M_{DC} within plus and minus ten percent. It was also shown that the controllers could become unstable if designed with a velocity that was less than the actual value or for a value of M_{DC} that was less than the actual value of M_{DC} . Additionally, when the controllers were designed with too high of a velocity or too large of a value of M_{DC} , they had a degraded performance.

CHAPTER 4

STATE AND PARAMETER ESTIMATION

4.1 Introduction

This chapter describes the design of the estimator used to identify the slope of the DC gain with respect to longitudinal velocity (M_{DC}) of the steer angle to yaw rate transfer function. The errors associated with neglecting dynamics in the yaw rate transfer function will be examined and an improvement in the estimator design is given. The rate of convergence of the estimator due to the forgetting factor on M_{DC} is also investigated. A description of the position estimator is detailed and a justification of its output equations is produced.

4.2 Extended Kalman Filter

The Extended Kalman Filter [Stengal, 1994; Bryson, 1975; Maybeck, 1979b; Gelb, 1992] is a first order Taylor series expansion of the Kalman Filter for nonlinear systems. The state and measurement equations are shown in Equations (4.1) and (4.2).

$$\dot{x} = f(x, u, w, t) \quad (4.1)$$

$$y = h(x, u, v, t) \quad (4.2)$$

The values passed to the state function are the previous estimate of the states, inputs, disturbances, and time. The values passed to the measurement function include the current estimate of the states, inputs, measurement noise, and time. The

nonlinearities for the yaw rate estimator occur from a state being multiplied by the input. In the linearization, the second order partial derivatives in the Taylor series expansion and higher are zero. Hence the estimator is not sub-optimal because an Extended Kalman Filter is being used. The estimator is sub-optimal because an approximated system is being used. The position estimator contains states times the sine and cosine of another state. This results in higher order partial derivatives in its Taylor series expansion which are non-zero. Therefore, a sub-optimal estimation is caused by the use of an Extended Kalman Filter. However, a state times the sine or cosine of another state is not a large nonlinearity for an estimator and an Extended Kalman Filter will provide a decent estimate, especially since it is updated at 100 hertz. An iterated Extended Kalman Filter [Gelb, 1992] could also provide the same improvement that a faster update gives. The position estimator is sub-optimal do to the approximation necessary for the use of an Extended Kalman Filter and an approximated system being used. Neglecting the higher order terms of a system that is modeled perfectly causes the estimate to be biased and the estimate of the covariance to be smaller then the correct value. The covariance being less than the actual value can lead to filter divergence. However, this can be corrected by designing the estimator with extra process noise.

Second order Taylor expansion Kalman Filters [Maybeck, 1979b] such as the Truncated Second Order Filter and the Gaussian Second Order Filter use Hessian matrices for bias correction and improvement of the covariance propagations. However, these estimators are much more computationally intensive then the Extended Kalman Filter. Most of the added computation is in the covariance propagations, and not in the

bias correction terms. The bias correction terms from these estimators can easily be used in an Extended Kalman Filter [Maybeck, 1979b].

Other Kalman Filters that would provide a better approximation include statistically linearized filters such as the Unscented Kalman Filter [Wan, 2000; Haykin, 2001]. The Unscented Kalman Filter provides a third order approximation for Gaussian noise systems and second order approximations for all other noise systems. It takes fewer computations than the second order Taylor series filters. This estimator does not require that the states or measurements have a derivative. Additionally, the Unscented Kalman Filter can be extremely helpful in debugging other estimators because it doesn't require derivative information.

The Extended Kalman Filter was chosen since the majority of the errors in the estimator are caused by model approximation and not by the format of the estimator. Also, the Extended Kalman Filter was chosen so that the yaw rate estimator could be implemented in fixed point as discussed in Chapter 6, for which a simple estimator was desired.

In the Extended Kalman Filter, the Jacobian matrices defined in Equations (4.3-4.5) are linearized with the state estimates from the time update.

$$H = \frac{\partial f(x, u, w, t)}{\partial x} \quad (4.3)$$

$$G = \frac{\partial f(x, u, w, t)}{\partial w} \quad (4.4)$$

$$U = \frac{\partial h(x, u, v, t)}{\partial v} \quad (4.5)$$

The covariance matrices for the Extended Kalman Filter are given in Equations (4.6) and (4.7), where Q is semi-definite and R is positive definite.

$$Q = E[w, w] \quad (4.6)$$

$$R = E[v, v] \quad (4.7)$$

The Kalman Filter gain (K) is computed with Equation (4.8), where U is typically an identity matrix.

$$K = PH^T (HPH^T + URU^T)^{-1} \quad (4.8)$$

Sequential processing is frequently used so that only a scalar value is inverted. The Kalman Filter gain is then used for updating the state estimates with the current measurements as shown below.

$$x_k = x_{k|k-1} + K(y_k - h(x_{k|k-1}, u_k, 0, t)) \quad (4.9)$$

As a result of the measurement update the covariance decreases by Equation (4.10), where I is the identity matrix.

$$P_k = (I - KH)P_{k|k-1} \quad (4.10)$$

Equations (4.8-4.10) are typically referred to as the measurement update since they only need to occur if a measurement is received. Equations (4.11) and (4.12) are typically referred to as the time update since they propagate the estimates to the next time step.

$$\dot{x}_{k|k-1} = f(x_{k-1}, u_{k-1}, 0, t) \quad (4.11)$$

$$\dot{P}_{k|k-1} = FP_{k-1} + P_{k-1}F^T + GQG^T \quad (4.12)$$

The time update for an Extended Kalman Filter can either be in discrete time or in continuous time. Equations (4.11) and (4.12) show the continuous state and covariance

propagations, which is how they are used for the position estimator. Note that the time update can be performed before a measurement is received.

The covariance propagation in the time update (4.12) increases the uncertainty in the states. The Jacobian matrices in Equation (4.12) are linearized with the state propagations from Equation (4.11) and the two equations are ideally integrated together so that the most accurate Jacobian matrices available are used.

The yaw rate estimator used in Section 4.3 has a discrete time update, and Equation (4.12) is replaced with Equation (4.13).

$$P_{k|k-1} = F_d P_{k-1} F_d^T + Q_d \quad (4.13)$$

Additionally, a discrete state equation replaces Equation (4.11).

The Extended Kalman Filter reduces to the Kalman Filter if the state and measurement equations are linear. Furthermore, the Extended Kalman Filter reduces to a Recursive Least Squares estimator [Stengel, 1994] if the system is linear, discrete and Equations (4.14) and (4.15) are used for the time update.

$$\dot{x}_{k|k-1} = 0 \quad (4.14)$$

$$P_{k|k-1} = P_{k-1} \quad (4.15)$$

The Extended Kalman Filter can reduce to a Recursive Least Squares [Astrom, 1989] with a forgetting factor by using Equations (4.14) and (4.15) using the following equation, and setting F_d to an identity matrix.

$$Q_d = \left(\frac{1}{\lambda} - 1 \right) P_{k-1} \quad (4.16)$$

4.3 Design of Yaw Rate Dual Estimator

A dual estimator simultaneously estimates clean states and model parameters. A clean estimate of yaw rate is needed for the position estimator. An estimate of M_{DC} is needed to adapt the steering controller. The state equations used for the design of the Extended Kalman Filter are shown in Equation (4.17).

$$x = \begin{bmatrix} r \\ r_{bias} \\ M_{DC} \end{bmatrix} = \begin{bmatrix} M_{DC}(V_x + w_V)(\delta + w_\delta) \\ r_{bias} + w_{r_{bias}} \\ M_{DC} + w_{M_{DC}} \end{bmatrix} \quad (4.17)$$

The states in the discrete estimator are yaw rate, yaw rate bias, and M_{DC} . Note that the yaw rate depends on the current measurement of steer angle. Therefore, the time update can not be calculated before a measurement is received. The velocity used in the estimator is from GPS which is available at 5 Hz. Although GPS provides velocity in the direction of course, a small angle approximation allows GPS velocity to be used for the longitudinal velocity.

The Jacobian of the state equations with respect to the states (4.18) shows that the rate at which M_{DC} converges will depend on the velocity and the steer angle.

$$F_d = \begin{bmatrix} 0 & 0 & V_x \delta \\ 0 & 1 & 0 \\ 0 & 0 & 1 \end{bmatrix} \quad (4.18)$$

The measurement in the Kalman filter is the yaw rate gyro which includes the yaw rate plus its bias, which is reflected in the Jacobian of the measurement equation with respect to the states shown below.

$$H = [1 \quad 1 \quad 0] \quad (4.19)$$

However, the yaw rate gyro bias will only be estimated when M_{DC} can be estimated, otherwise the bias would be corrupted with scale factor errors. Therefore, Equation (4.20) will be used when there is too little excitation.

$$H = [1 \ 0 \ 0] \quad (4.20)$$

The bias could be estimated under low excitation by augmenting the estimator with a heading state and using the approximation that course angle equals heading angle at low levels of excitation [Bevly, 2001]. However, in Chapter 6 the estimator is designed in fixed point where only a limited number of states can be estimated.

Since a discrete covariance time update is used, the discrete process noise matrix was approximated using Equation (4.21).

$$Q_d = G_d Q_1 G_d^T = \begin{bmatrix} M_{DC} V_x & M_{DC} \delta & 0 & 0 \\ 0 & 0 & 1 & 0 \\ 0 & 0 & 0 & 1 \end{bmatrix} \begin{bmatrix} \sigma_\delta^2 & 0 & 0 & 0 \\ 0 & \sigma_v^2 & 0 & 0 \\ 0 & 0 & \sigma_{r_{bias}}^2 & 0 \\ 0 & 0 & 0 & \sigma_{M_{DC}}^2 \end{bmatrix} \begin{bmatrix} M_{DC} V_x & 0 & 0 \\ M_{DC} \delta & 0 & 0 \\ 0 & 1 & 0 \\ 0 & 0 & 1 \end{bmatrix} \quad (4.21)$$

In Equation (4.21), the process noise on the yaw rate state was computed to be a function of the DC gain times the yaw rate disturbance covariance (σ_δ) plus the noise covariance for the velocity (σ_v) times M_{DC} and the steer angle measurement. The sensor noise on the steer angle measurement was considered negligible. The yaw rate bias and M_{DC} were both modeled as random walks with covariances $\sigma_{r_{bias}}$ and $\sigma_{M_{DC}}$, which will determine how fast the estimates will react to changes in the states after the estimator has settled. The measurement noise for the estimator was simply found with Equation (4.22).

$$R = [\sigma_r^2] \quad (4.22)$$

Even though there is a clear relationship between the yaw rate and steer angle, it can not be estimated continuously, because too little excitation will cause the estimate to fit disturbances. A method of determining how much excitation exists in the system is therefore needed. Auto-correlation matrices of varying sizes can be used to determine how many parameters can be estimated [Astrom, 1995]. The largest auto-correlation matrix that is of full rank corresponds to the order of excitation there is in the system. The order of excitation then corresponds to how many parameters can be estimated. Since only one parameter is desired to be estimated in this thesis, only a one by one auto-correlation matrix would have to be of full rank, which is always of full rank if it is non zero. It is possible to determine when there is enough excitation by evaluating larger auto-correlation matrices. However, sensor noise may make it appear as if there is more excitation than actually exists. Therefore, the magnitude of a windowed auto-correlation was used to determine the degree of excitation in the system. This indicates that there is a current trend in the steer angle, as opposed to a single large measurement, which makes it likely that M_{DC} can be estimated for some period of time. With this method there is a possibility that the window analysis may determine there is enough excitation for adaptation for the period defined by the time in the window, even though current excitation is quite low. However, the rate of convergence decreases, as seen in Equation (4.18), as the magnitude of the steer angle decreases. Therefore, little convergence would occur towards an incorrect value in this case. The main goal of the determination of when to adapt is to prevent a prolonged estimation during low levels of excitation.

Figure 4.1 shows the value of the auto-correlation of the steer angle over a one second window for an experimental test. When this value is large enough that a fixed

relationship can be seen between the steer angle and yaw rate, it is determined that it is safe to adapt the system. A threshold value is used for this determination which should depend on the maximum expected disturbance in the yaw rate and the amount of sensor noise on the steer angle. As can be seen from Figure 4.1, a reliable time to adapt usually occurs at the beginning of the controlled run when the controller makes a step input to the tracked line. The analysis also allows for an improved estimate if the tracking degrades as is also shown Figure 4.1 (at time = 60 seconds).

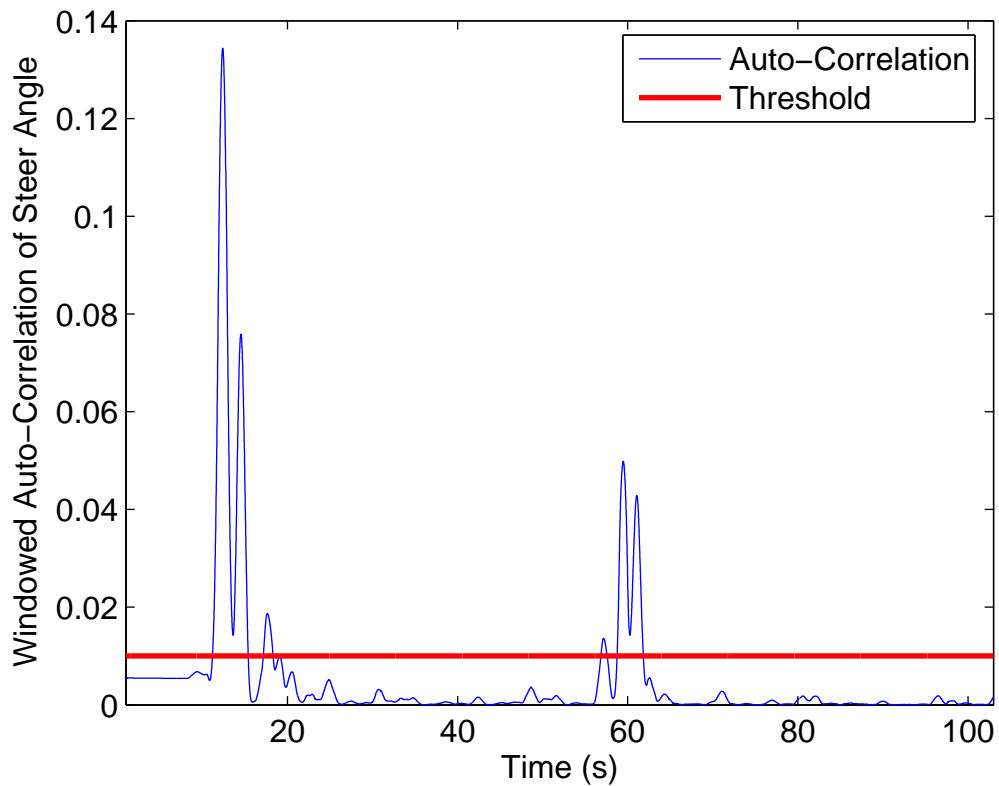


Figure 4.1: Windowed auto-correlation of steer angle.

When there is adequate excitation to accurately estimate M_{DC} , the covariance associated with M_{DC} is reset 0.0025 in order to inject uncertainty into the system and

allow the estimate to converge quickly. When there is too little excitation in the system, the Kalman gain associated with M_{DC} is over-ridden with zero and the noise covariance for M_{DC} and the yaw rate bias is set to zero. This is numerically equivalent to changing (4.18) to (4.23) and changing (4.21) to (4.24), where $P_{M_{DC}}$ is the estimated covariance of M_{DC} .

$$F_d = \begin{bmatrix} 0 & 0 & 0 \\ 0 & 1 & 0 \\ 0 & 0 & 1 \end{bmatrix} \quad (4.23)$$

$$Q_d = \begin{bmatrix} M_{DC}V_x & M_{DC}\delta & 0 & 0 & V_x\delta \\ 0 & 0 & 1 & 0 & 0 \\ 0 & 0 & 0 & 1 & 0 \end{bmatrix} \begin{bmatrix} \sigma_\delta^2 & 0 & 0 & 0 & 0 \\ 0 & \sigma_v^2 & 0 & 0 & 0 \\ 0 & 0 & 0 & 0 & 0 \\ 0 & 0 & 0 & 0 & 0 \\ 0 & 0 & 0 & 0 & P_{M_{DC}} \end{bmatrix} \begin{bmatrix} M_{DC}V_x & 0 & 0 \\ M_{DC}\delta & 0 & 0 \\ 0 & 1 & 0 \\ 0 & 0 & 1 \\ V_x\delta & 0 & 0 \end{bmatrix} \quad (4.24)$$

Figure 4.2 shows the results of M_{DC} being estimated in a simulation with a steady-state input. The estimator was told to start estimating M_{DC} at time = 200 seconds and stop at time = 400 seconds. The actual value of M_{DC} was also decreased by ten percent at time = 300 seconds without the covariance being reset. As seen, the estimate of M_{DC} almost immediately reaches the correct value due to the covariance being reinitialized at time = 200 seconds. The estimate takes longer to converge to the new value at time = 300 seconds because only the forgetting factor is causing the estimate to move. This rate of convergence is investigated more in Section 4.5. System identification tests found that the disturbances were best described as second or third order transfer functions. However, the process disturbances are modeled as white noise in the estimator. In order for all of the process disturbances to propagate through the estimator, the value of the

disturbance covariance (σ_δ) would have to be large. Unfortunately, this would result in the MDC estimate taking a long time to converge. Therefore, the disturbance covariance is kept small to allow for faster convergence at the cost of filtering out some of the process disturbances. Because the disturbances were filtered, adaptively changing the noise covariance for M_{DC} was not investigated.

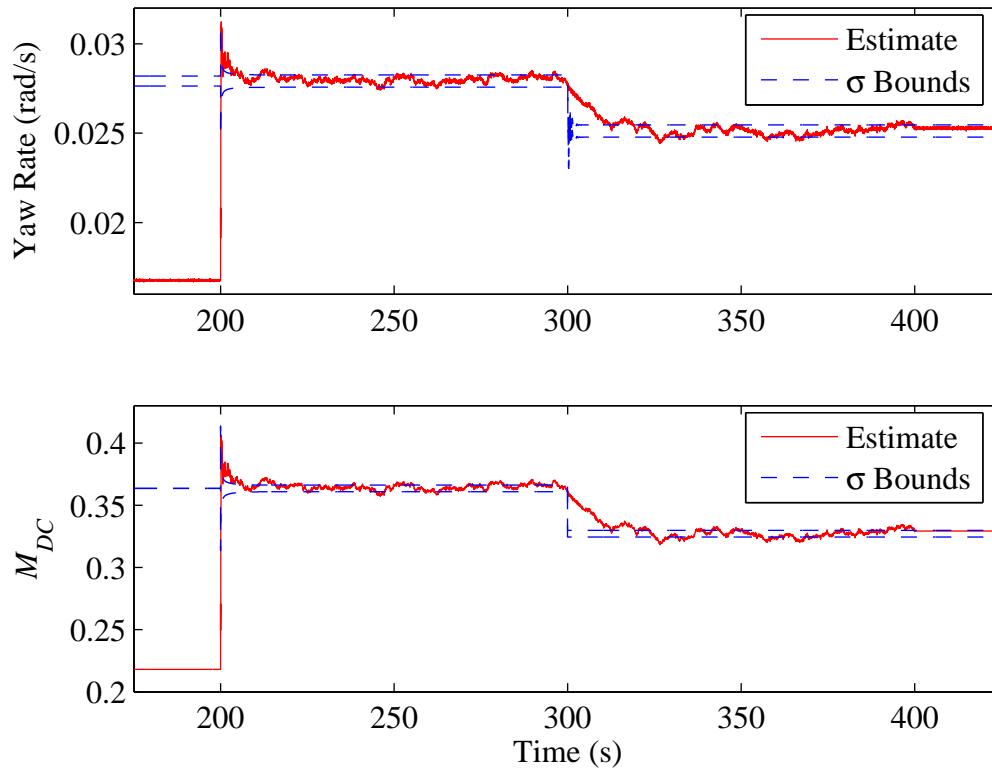


Figure 4.2: Estimate of M_{DC} and yaw rate.

The nominal noise values used in the design of the Extended Kalman Filter are listed in Table 4.1.

Table 4.1 Discrete noise values used for the yaw rate dual estimator

Parameter	Value	Units	Frequency
σ_v	0.05	meters/second	5 Hz
σ_δ	8.73×10^{-4}	radians	100 Hz
$\sigma_{r_{bias}}$	1×10^{-7}	radians/second	100 Hz
$\sigma_{M_{DC}}$	1×10^{-4}	1/meters	100 Hz
σ_r	5.23×10^{-3}	radians/second	100 Hz

4.4 Sensitivity of Estimation to Neglected Dynamics

To examine how the accuracy of the estimate is affected by neglecting the poles and zeros in the yaw rate transfer function, a simulation was designed to see what kind of errors this would cause. The transfer function used to simulate the disturbance free plant and the disturbances (shown in Equations (4.25) and (4.26), respectively) were taken from a Box Jenkins fit of experimental data at 2 mph with no implement.

$$\frac{r}{\delta} = \frac{-0.288557z^3 + 0.814621z^2 - 0.765003z + 0.239394}{z^4 - 3.718368z^3 + 5.343205z^2 - 3.522835z + 0.899421} \quad (4.25)$$

These transfer functions represented a worse case scenario, because they contained the largest magnitude and phase change over the low frequencies found from system identification tests.

$$\frac{r_{dist}}{e} = \frac{z^2 + 2.002189z + 1.002191}{z^2 - 1.880024z + 0.944499} \quad (4.26)$$

The standard deviation of the noise generating the disturbances was also obtained from the Box Jenkins fit, and is displayed below with the units of radians.

$$\sigma_e = 0.00013869622 \quad (4.27)$$

Sine waves at a number of different frequencies and amplitudes were tested as inputs to determine the resulting mean and standard deviations of the estimates after the estimator had settled. The simulation assumed that there was always enough excitation to estimate M_{DC} and was run long enough to determine a clear trend in the data.

Figure 4.3 shows the actual value of M_{DC} with the average value of the M_{DC} versus frequency with input amplitudes of 5, 10, and 15 degrees. Also shown in the figure is the magnitude of the gain in Equation (4.25) divided by velocity, which is labeled as (Bode Magnitude)/V. Recall that M_{DC} is the magnitude of the DC gain divided by velocity and is therefore represented as a constant value. The magnitude of gain in Equation (4.25) divided by velocity corresponds to the value of M_{DC} that should be estimated if there is no phase change. As can be seen, the estimated values are close to the bode curve at less than 1 rad/sec but estimates lower than it at higher frequencies. The estimates became worse at higher frequencies. It should be noted that the tractor dynamics rarely operate in these high frequencies. As will be shown later in this section, these errors can be reduced using a more accurate model in the estimator.

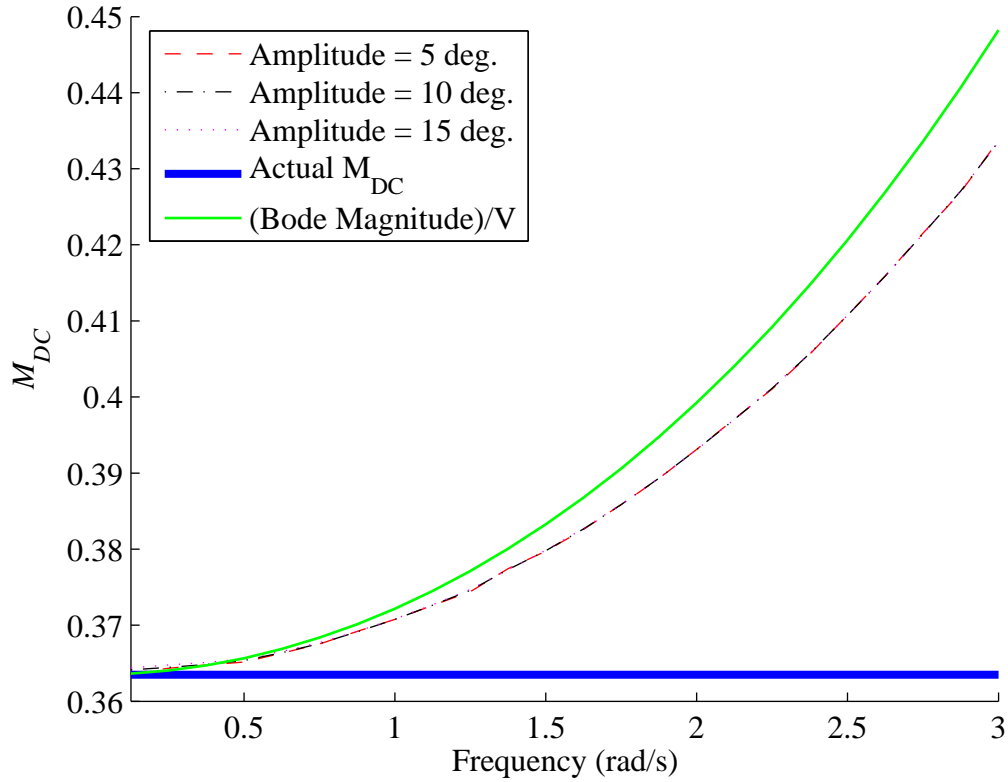


Figure 4.3: Mean M_{DC} versus input frequency using the input of $\delta = A \sin(\omega t)$.

Figure 4.4 contains the clean yaw rate, the steer angle times the DC gain of Equation (4.25), and the estimated yaw rate for a 3 rad/s simulation with a steer angle input of 5 degrees. As seen in the figure, there also exists a phase difference in addition to the magnitude difference. However the magnitude error is the main source of error shown in Figure 4.3. This is because the difference in the phase between the actual system and estimator model is minimal (compared to the differences in magnitude) as is shown later in Figure 4.10.

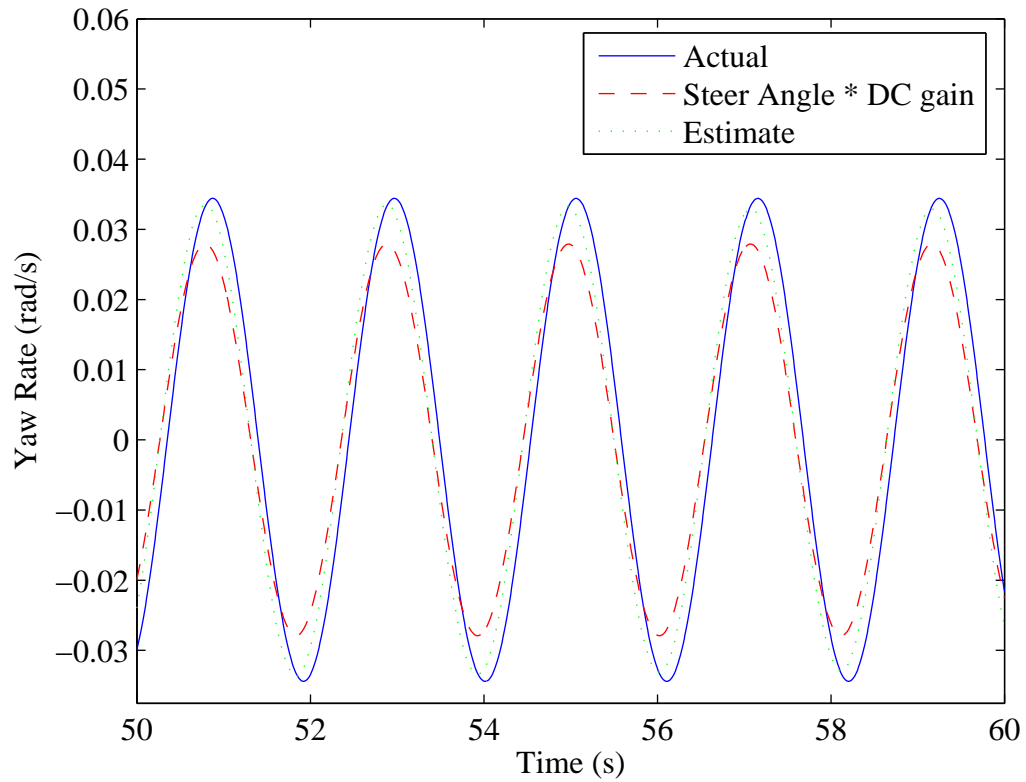


Figure 4.4: Magnitude and phase difference between yaw rate and steer angle times DC gain for $\delta = 5 \sin(3t)$ (degrees).

Figure 4.5 shows the estimated M_{DC} for the simulated run shown in Figure 4.4. As seen in the figure, the estimate contains some of the 3 rad/s sine wave due to the forgetting factor placed on the estimate.

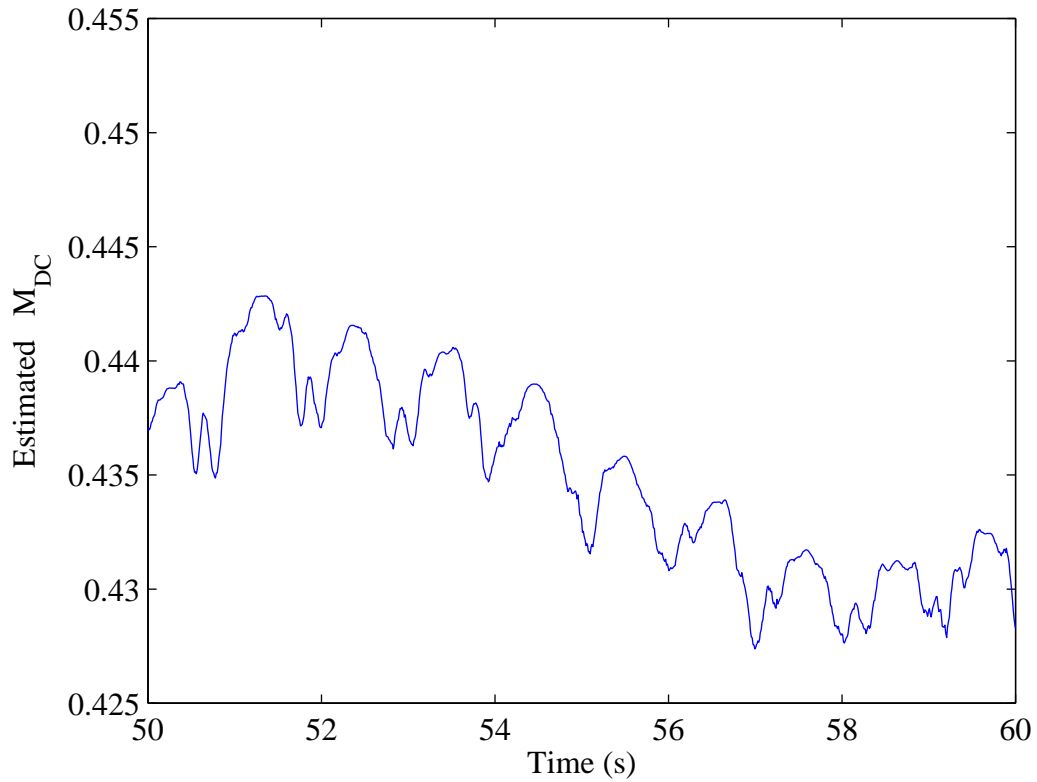


Figure 4.5: Estimate of M_{DC} with an input of $\delta = 5 \sin(3t)$ (degrees).

In Figure 4.6 shows the standard deviation of the estimated M_{DC} for each velocity and input amplitude, which should contain the same standard deviation regardless of frequency. The Jacobian of the state equations with respect to the states (4.18) shows that the estimate will be less uncertain when the input is larger. However, this is not reflected in Figure 4.6. This may be because due to the fact that at higher amplitudes more of the sine wave is incorporated into its estimate.

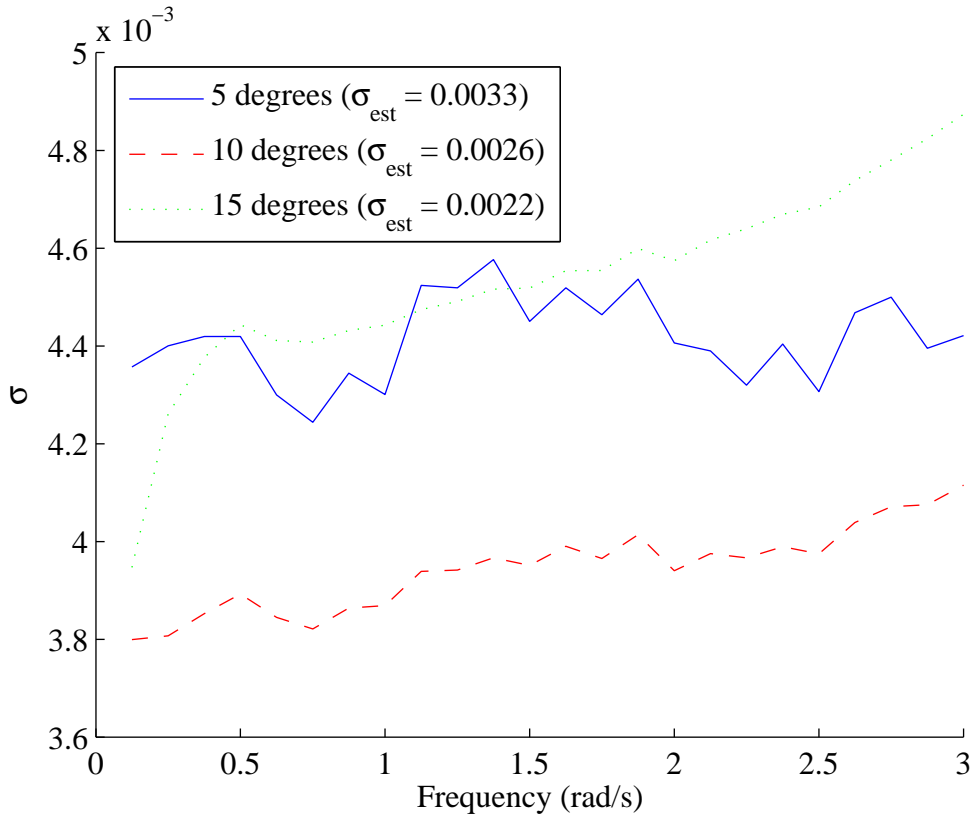


Figure 4.6: Standard deviation of estimated M_{DC} versus input frequency.

The Kalman Filter provides an estimate of the covariances of the states. The square root of the covariance once the estimator has converged for the M_{DC} state is contained in Table 4.2 for an input amplitude of 1 rad/s. Note that the values in Figure 4.6 are greater than the values in Table 4.2, because as mentioned previously the forgetting factor causes some of the sine wave to be incorporated into the estimate.

Table 4.2: Square root of covariance of M_{DC} provided by the estimator

Sine Wave Amplitude	Standard Deviation
5 degrees	3.11×10^{-3}
10 degrees	2.18×10^{-3}
15 degrees	1.77×10^{-3}

Using the bode magnitudes from the system identification tests divided by velocity for the upper bounds on the M_{DC} estimate, Figure 4.7 shows that with no implement the errors decrease as velocity increases. Since the value should be the same as at zero frequency. Similarly Figure 4.8 shows that the error decreases with hitch loading.

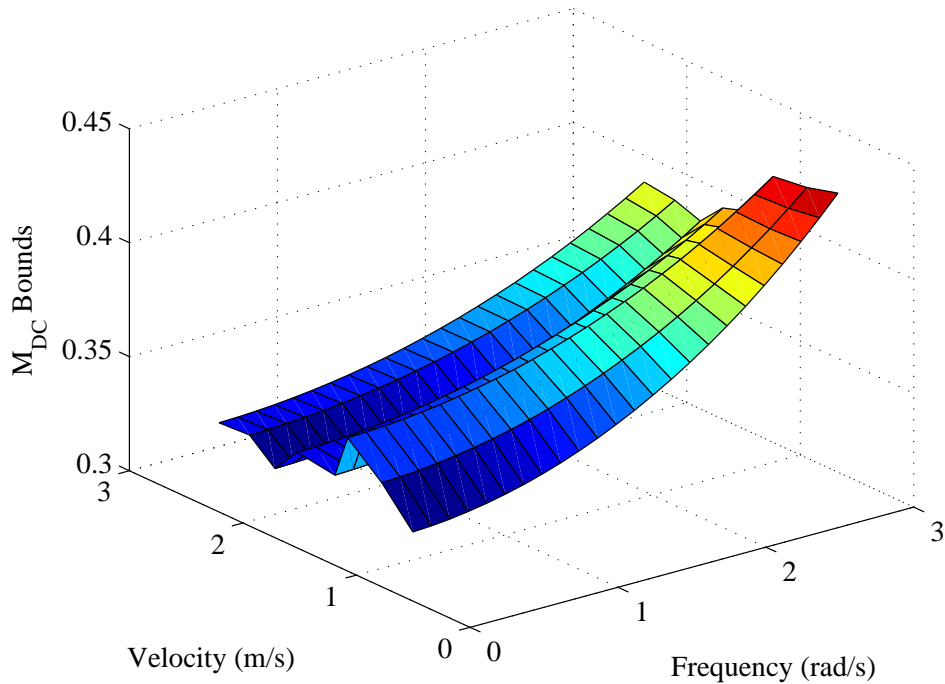


Figure 4.7: Bode magnitudes divided by velocity for no implement.

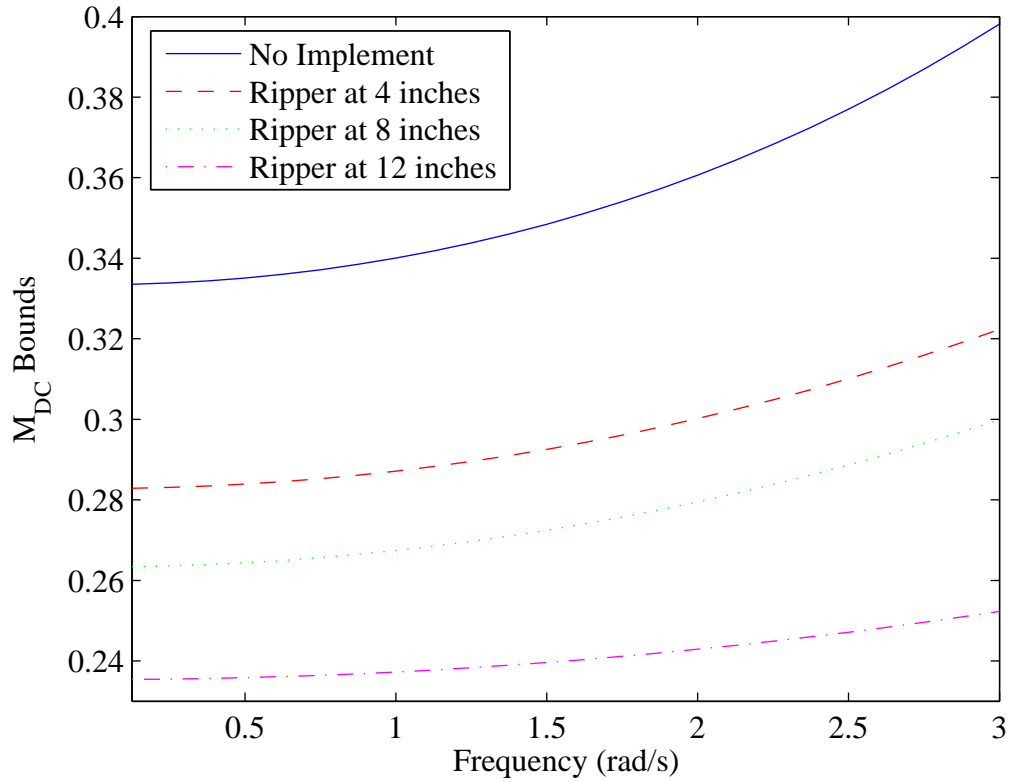


Figure 4.8: Bode magnitudes divided by velocity for various hitch loadings at 3 mph.

The estimation of M_{DC} can be improved through the use of the dominant poles of the system. Equation (4.28) shows the transfer function that was used in an improved estimator.

$$\frac{r}{\delta} = \frac{(1 - 1.962266z + 0.970604)M_{DC}V_x}{z^2 - 1.962266z + 0.970604} \quad (4.28)$$

This requires that an additional intermediate state (η) be added to the estimator, which is shown in Equation (4.29).

$$x = \begin{bmatrix} r \\ \eta \\ r_{bias} \\ M_{DC} \end{bmatrix} = \begin{bmatrix} 1.962266r + \eta \\ -0.970604r + (1 - 1.96226 + 0.970604)M_{DC}(V_x + w_V)(\delta + w_\delta) \\ r_{bias} + w_{r_{bias}} \\ M_{DC} + w_{M_{DC}} \end{bmatrix} \quad (4.29)$$

The Jacobian of the measurement equations with respect to the states then changes to Equation (4.30) when the bias can be estimated.

$$H = [1 \quad 0 \quad 1 \quad 0] \quad (4.30)$$

The computation of the discrete covariance matrix is performed with Equation (4.31) using the same approximation as in Equation (4.21) and using the same value of Q_I .

$$G_d = \begin{bmatrix} (1 - 1.96226 + 0.970604)M_{DC}V_x & (1 - 1.96226 + 0.970604)M_{DC}\delta & 0 & 0 \\ 0 & 0 & 0 & 0 \\ 0 & 0 & 1 & 0 \\ 0 & 0 & 0 & 1 \end{bmatrix} \quad (4.31)$$

The simulation was then run again with the new estimator. As seen in Figure 4.9 the difference between the estimated gain and the Bode magnitude at 3 rad/sec is now half that of what was obtained using the previous estimator. The (Bode Magnitude)/V value shown in the figure was obtained through Equation (4.32).

$$\frac{Mag_{sys-est}}{V} = \frac{Mag_{Full Model}}{V} - \left(\frac{Mag_{Second Order Model}}{V} - M_{DC} \right) \quad (4.32)$$

This corrects the Bode magnitude from Equation (4.25) for the magnitude improvement obtained from using the second order model in the estimator. As can be seen in Figure 4.9, the estimates are now closer to the Bode magnitude, which implies that the phase errors are having less of an effect than what was shown in Figure 4.3.

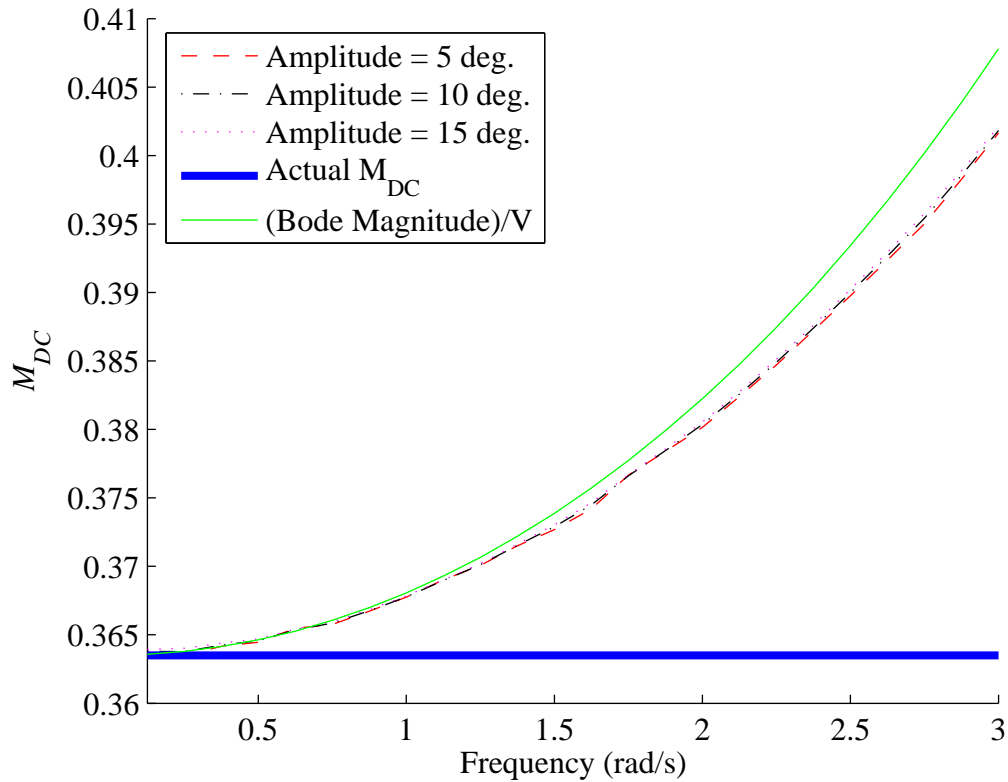


Figure 4.9: Mean M_{DC} versus input frequency for second order model.

Figure 4.10 shows the frequency response of the simulated system and the second order system in the estimator for the frequencies used in the simulation. As seen in the figure, the dominant poles do not account for all of the magnitude and phase change in the simulated system. This is most likely caused by the set of zeros after the dominant poles having little damping themselves. Therefore, it may be possible to design an improved estimator by adding more dynamics or by possibly by modifying the identified dominant poles to have less damping such that the magnitudes of the actual model and estimator model match more closely.

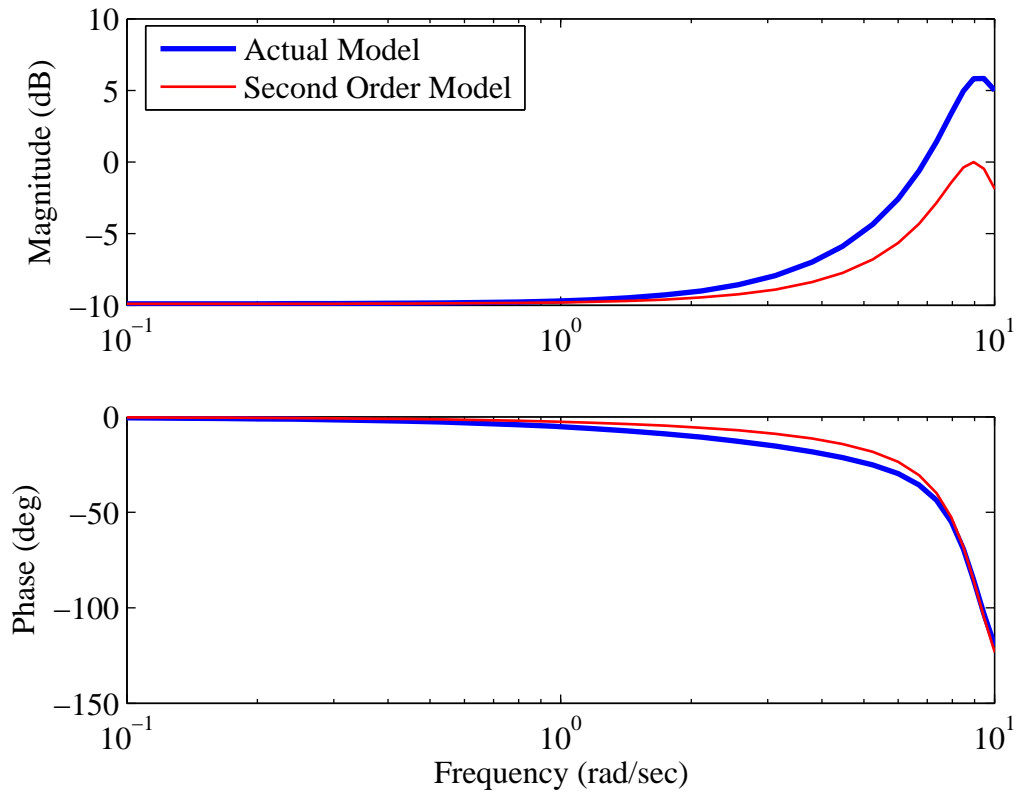


Figure 4.10: Frequency response of the actual system and second order estimator model.

Figure 4.11 shows the standard deviation of the simulations with the improved estimator. Note that the estimates now have the same standard deviations regardless of the frequency and that the effects of the estimate incorporating the sine wave have been reduced.

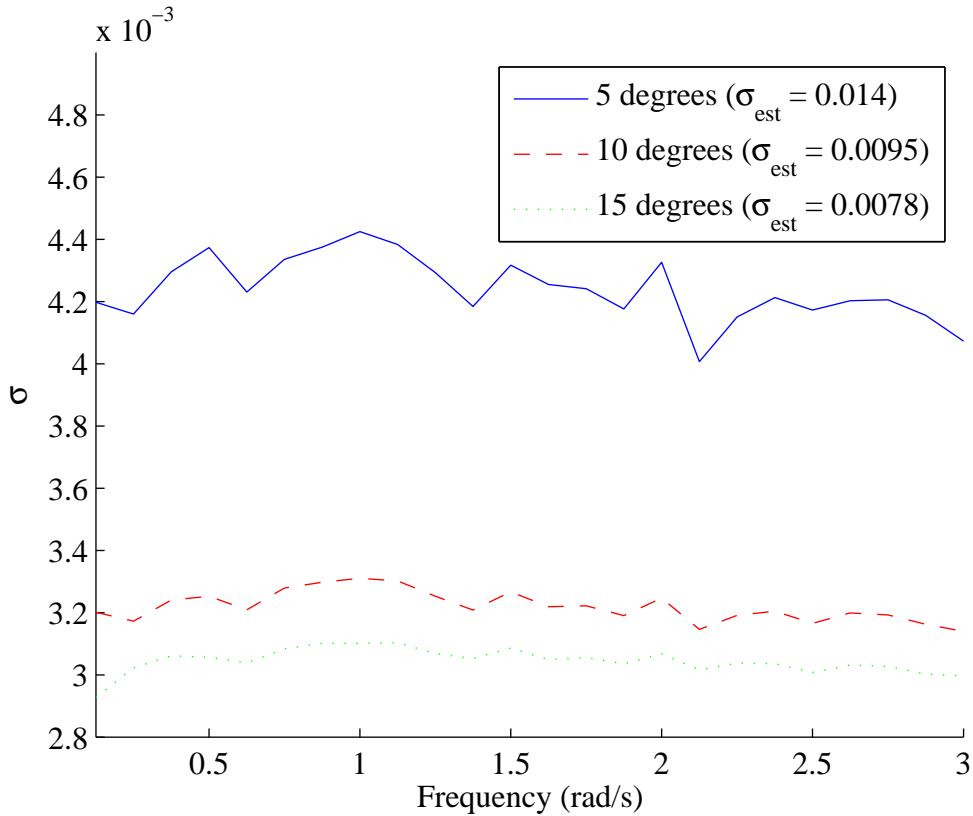


Figure 4.11: Standard deviation of M_{DC} for improved estimator.

4.5 Rate of Convergence

A simulation was conducted using steady state inputs to examine how long it takes for the estimator to converge on the correct value without using the covariance resetting, such that only the forgetting factor caused the convergence. No noise was added to the simulated measurements passed to the estimator, but the assumed that the nominal noise characteristics. This produces the same results as a monte carlo simulation since the measurement noise is zero mean. Figure 4.12 shows the results from three different offsets, for which it can be seen that they all converge at the same amount of time. This is understandable because the Extended Kalman Filter effectively acts as a

closed loop controller of the estimates and the value of M_{DC} is effectively making a step input to the correct value.

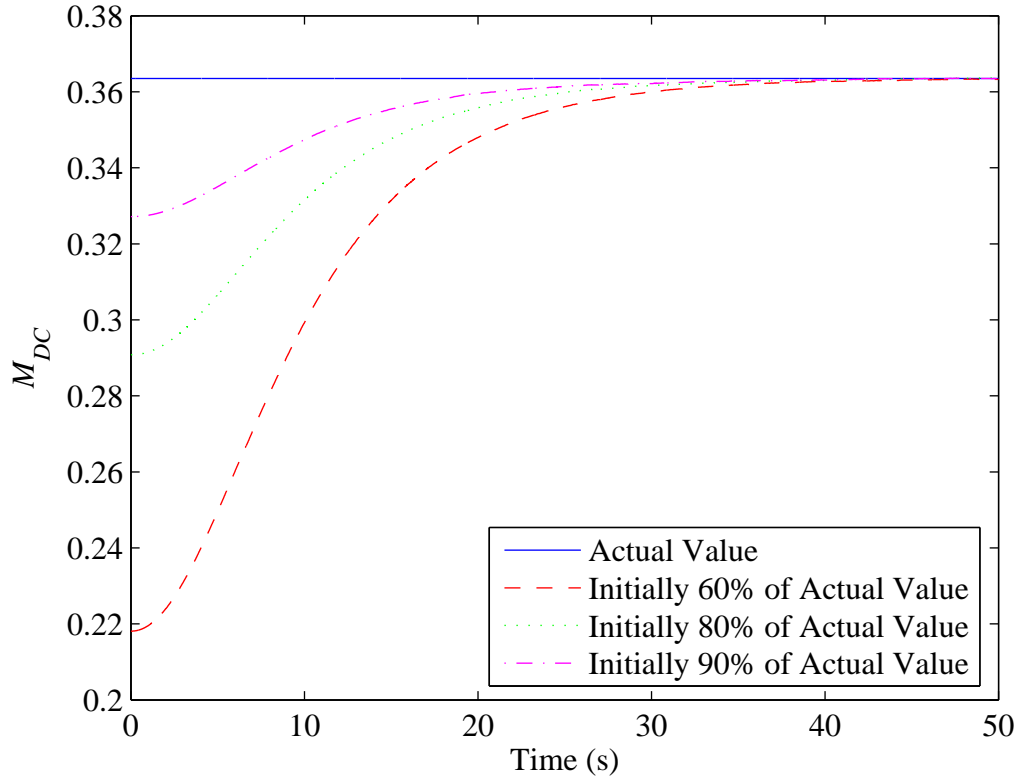


Figure 4.12: Convergence from different offsets.

While the amount of time to converge is independent of the offset, it is dependent on $V_x\delta$ according to Equation (4.18). Therefore, the simulation was conducted again for various $V_x\delta$ with different noise values used for M_{DC} ($\sigma_{M_{DC}}$). The time to converge to within 99.9 % of the correct value was recorded. As shown in Figure 4.13, M_{DC} converges faster for larger values of $\sigma_{M_{DC}}$ and when $V_x\delta$ is larger.

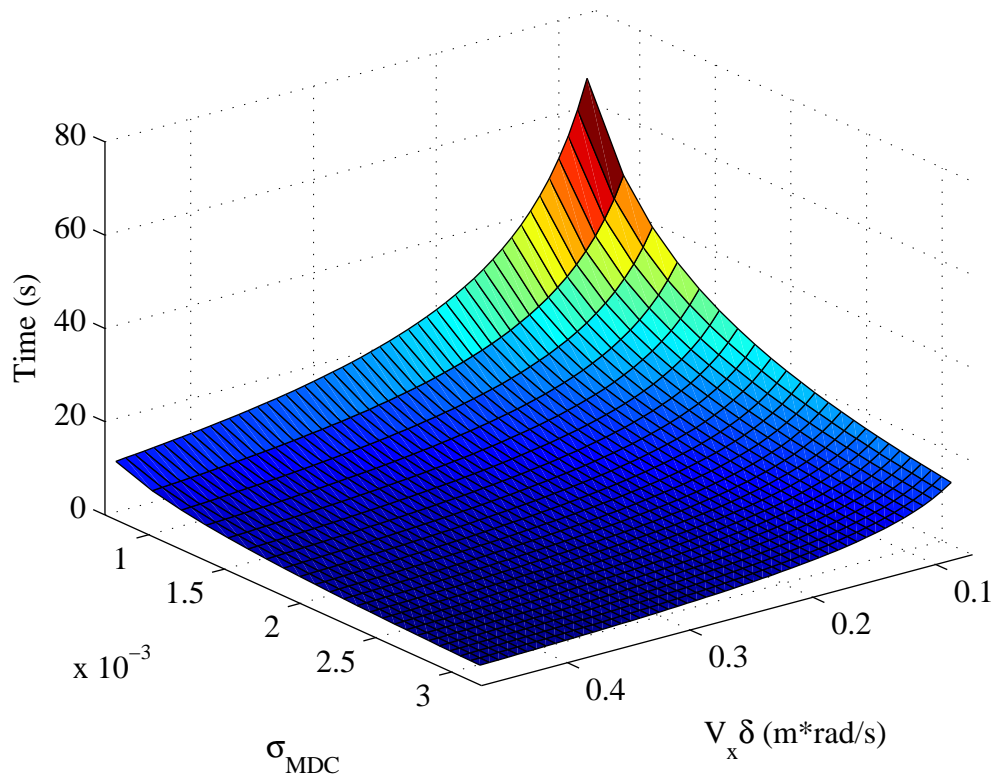


Figure 4.13: Time to converge within 99.9 % of the correct value.

The square root of the estimated covariances for the simulations in Figure 4.13 was also recorded and is shown in Figure 4.14. It can be seen that the estimates get noisier as the noise value on M_{DC} is increased. It can also be seen in Figure 4.14 that the estimator noise placed on the M_{DC} state can be increased, allowing for faster convergence of the estimate, when $V_x \delta$ increases without sacrificing accuracy of the M_{DC} estimate. However, recall that in Section 4.3 it was found that the actual accuracy of the estimate is likely much larger than the predicted accuracy shown in Figure 4.14.

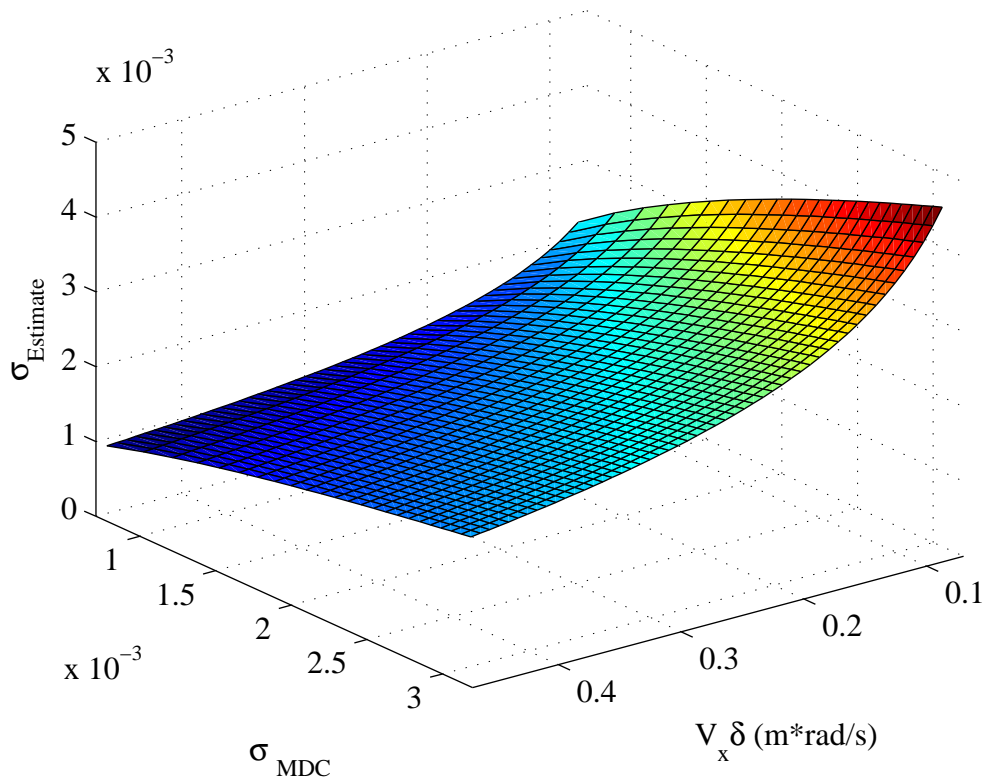


Figure 4.14: Estimated standard deviation for M_{DC} .

4.5 Design of Position Estimator

The states in the position estimator are north, east, and course. The input to the position estimator is the filtered yaw rate from the yaw rate estimator. Unlike the yaw rate estimator which uses GPS velocity to approximate longitudinal velocity, the position estimator needs the velocity in the direction of the course angle. Therefore, GPS provides the correct measurement of velocity for this estimator. The calculation of north and east involves a coordinate transformation from the body fixed frame to the global frame, as can shown in Equation (4.31), which contains the continuous state equations for the estimator.

$$\dot{x} = \begin{bmatrix} \dot{N} \\ \dot{E} \\ \dot{\nu} \end{bmatrix} = \begin{bmatrix} (V_\nu + w_\nu) \cos(\nu) \\ (V_\nu + w_\nu) \sin(\nu) \\ r + w_r \end{bmatrix} \quad (4.31)$$

Since there is no velocity perpendicular to the course direction, there is only one term in the north and east derivatives. Note that yaw rate plus the derivative of side slip is the derivative of course ($\dot{\nu} = r + \dot{\beta}$). However, it will be shown that the course measurement provided by GPS is clean enough to compensate for neglecting the derivative of sideslip in the estimator.

The Jacobian of the state equations with respect to the states is shown in Equation (4.32).

$$F = \begin{bmatrix} 0 & 0 & -V_\nu \sin(\nu) \\ 0 & 0 & V_\nu \cos(\nu) \\ 0 & 0 & 0 \end{bmatrix} \quad (4.32)$$

Since the errors in the state equations include sensor noise on the velocity and uncertainty in the yaw rate estimate passed to the position estimator, the Jacobian of the state equations with respect to the disturbance contains two columns as shown in Equation (4.33).

$$G = \begin{bmatrix} \cos(\nu) & 0 \\ \sin(\nu) & 0 \\ 0 & 1 \end{bmatrix} \quad (4.33)$$

The first column is associated with the velocity sensor noise and the second column is associated with the uncertainty in the yaw rate estimate.

The continuous process noise covariance matrix shown in Equation (4.34) contains the covariance of the sensor noise for the velocity measurement (σ_v) and the covariance of the yaw rate that has been passed from the yaw rate estimator ($P_{M_{DC}}$).

$$Q = \begin{bmatrix} \sigma_v^2 & 0 \\ 0 & P_{M_{DC}} \end{bmatrix} \quad (4.34)$$

It should be noted that the yaw rate estimator provides a discrete covariance for its filtered yaw rate which must be converted to continuous before being used in Equation (4.34). However, no coordinate transformation of the yaw rate covariance is necessary since roll and pitch angles have been assumed to be negligible.

The GPS messages have significantly more computation time than the inertial measurements. However, if this computational delay is known, it can be accounted for in the output equation of the estimator. In order to obtain the amount of delay in the GPS output, an RTD GPS receiver with a pulse per second (PPS) output, a one hundred kilohertz clock (synchronized to the GPS PPS), and two counters were used. Knowing that the pulse per second of the RTD GPS receiver and the Starfire measurement are synchronized, the one hundred kilohertz clock and the two counters were used to determine the lag between when the GPS measurement occurred and when the serial message arrived at the computer. Figure 4.15 shows the results of one experimental test.

The mean value of the delay in the figure is 0.0787 seconds. It should be noted that some of the noise is most likely to be from the message passing between the serial driver and the logging program, which can generally be slow. A more accurate way of getting this lag would be to monitor the serial port's interrupt line.

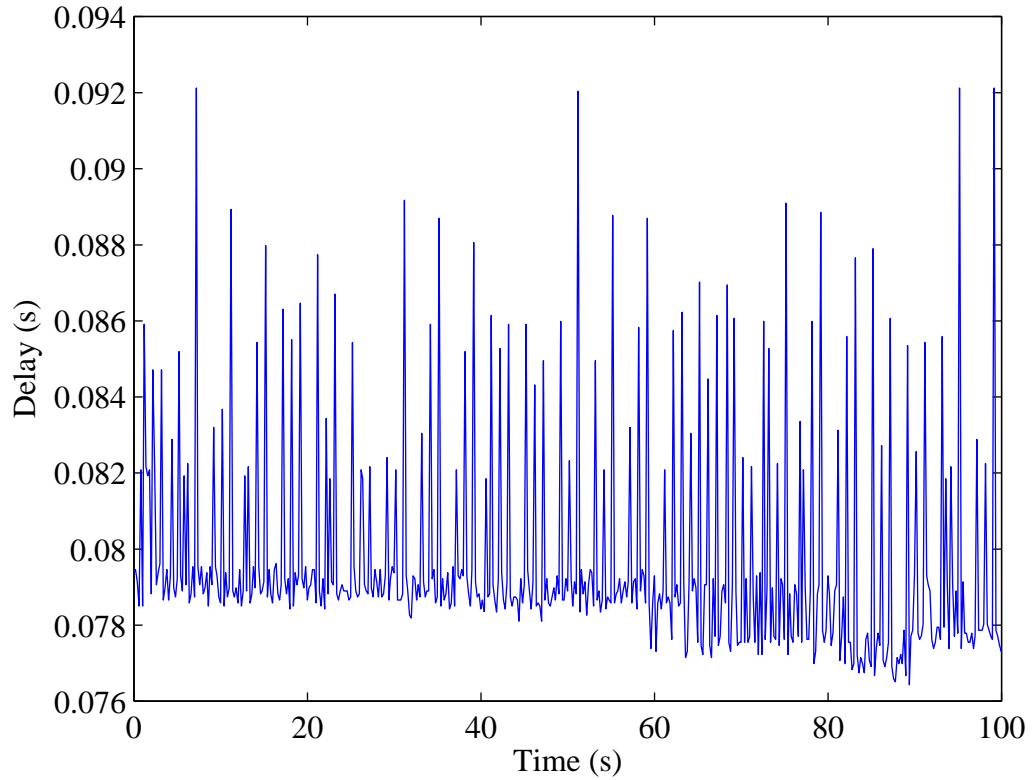


Figure 4.15: Delay in GPS messages

The lag in the receipt of the GPS messages can then be accounted for in the measurement update of the estimator. Equation (4.35) shows that a simple Euler approximation can be used along with the estimates of the states to propagate the current estimates back to when the measurement should have been received.

$$y = \begin{bmatrix} N_{meas} \\ E_{meas} \\ V_{meas} \end{bmatrix} = \begin{bmatrix} N - V_v \cos(\nu) T_{lag} + v_N \\ E - V_v \sin(\nu) T_{lag} + v_E \\ \nu - r T_{lag} + v_\nu \end{bmatrix} \quad (4.35)$$

Section 4.6 will provide further evidence that this compensation is needed. In Equation (4.35) T_{lag} is the time that has elapsed between when the measurements should have been

received by the estimator and when they are used in the estimator. While the time update of the position estimator is conducted at 100 hertz, the measurement update only occurs when a GPS measurement is available, which is at 5 hertz.

In the Jacobian of the measurement equations with respect to the states, Equation (4.36), it can be seen that a correction of the course angle is provided directly from the position measurements because of the delay.

$$H = \begin{bmatrix} 1 & 0 & V_v \sin(\nu) T_{lag} \\ 0 & 1 & -V_v \cos(\nu) T_{lag} \\ 0 & 0 & 1 \end{bmatrix} \quad (4.36)$$

The Jacobian of the measurement equations with respect to the measurement noises shown in Equation (4.37) is no longer an identity matrix, since there is now a direct contribution from the input of the estimator to the output.

$$U = \begin{bmatrix} 1 & 0 & 0 & 0 \\ 0 & 1 & 0 & 0 \\ 0 & 0 & 1 & -T_{lag} \end{bmatrix} \quad (4.37)$$

The discrete covariance of yaw rate from the yaw rate estimator is then needed to be included in the measurement noise covariance matrix shown in Equation (4.38).

$$R = \begin{bmatrix} \sigma_N^2 & 0 & 0 & 0 \\ 0 & \sigma_E^2 & 0 & 0 \\ 0 & 0 & \sigma_\nu^2 & 0 \\ 0 & 0 & 0 & P_{M_{DC}} \end{bmatrix} \quad (4.38)$$

In the equation σ_N and σ_E are the noises on the position states, whose errors are dominated by its bias. However, since the estimator doesn't have a way to remove this bias, the estimator uses a noise value in order to filter some of the bias. The value σ_ν is

the standard deviation of the course angle measurement which is a function of velocity and $P_{M_{DC}}$ is the covariance passed from the yaw rate estimator.

In Figure 4.16 a comparison of the measured and estimated course shows that despite the derivative of sideslip ($\dot{\beta}$) being neglected in the position estimator, the GPS course measurement is accurate enough to provide corrections.

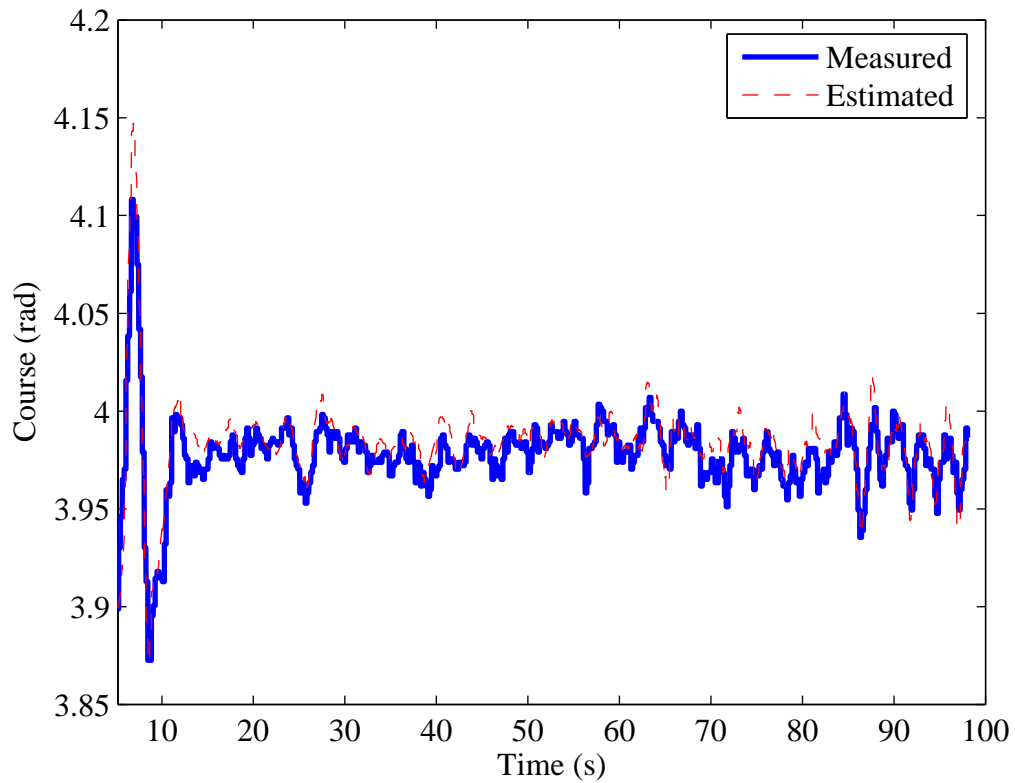


Figure 4.16: Comparison of measured and estimated course from experimental test.

The discrete noise values used in the Extended Kalman Filter for the position estimator are listed in Table 4.3. These values and their continuous counterparts were used in Equations (4.34) and (4.38).

Table 4.3: Discrete noise values used for the position estimator

Parameter	Value	Units	Frequency
σ_V	0.05	meters/second	5 Hz
σ_N	0.02	meters	5 Hz
σ_E	0.02	meters	5 Hz
σ_ψ	$\frac{0.05}{V}$	radians	5 Hz

4.6 Effects of GPS Delay

To test the effects of the GPS delay on the position estimator, the simulation in Section 4.4 was again used. The input used was a sinusoidal steer angle with a 5 degree amplitude at 2 mph, driving in open loop, in the direction of north. Three simulations were run to compare the effect of the GPS delay. The first simulation had no GPS delay, the second simulation had a 0.08 second delay with no compensation in the estimator, and the third simulation had a 0.08 second delay which was compensated for in the estimator. The estimators used the nominal sensor and input noise specifications, but noiseless values were provided to the estimators so that a clearer picture of the errors could be obtained. Additionally, no side slip was included in the simulation and hence course reduced to heading.

Figure 4.17 shows the result for the error in the north position estimate for the three simulations. Without compensating for the delay the vehicle estimate is behind the true location. However for this work, longitudinal accuracy is not a degrading factor. Some of the cosine wave can also be seen in the uncompensated system, which is due to

the lateral effects from the tractor not always heading north. The estimates for the compensated system are slightly ahead of the true position, likely due to integration errors.

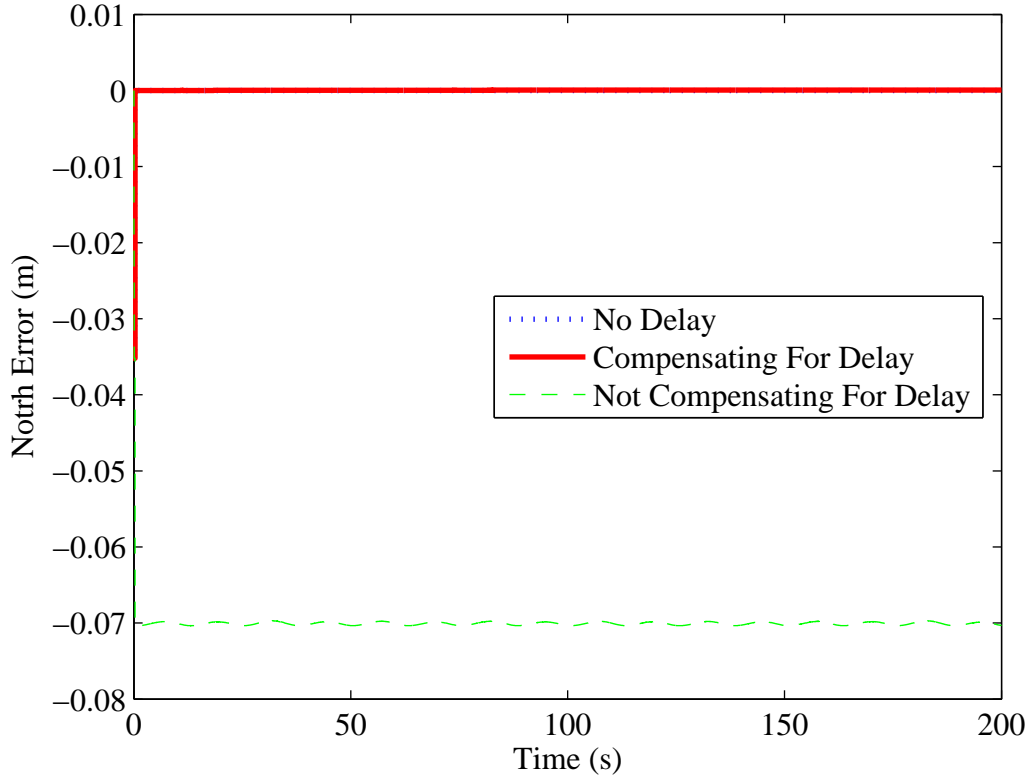


Figure 4.17: North error

From Equation (4.35) it can be seen that the longitudinal error of the vehicle can be approximated with Equation (4.39).

$$e_{longitudinal} = -V_x T_{lag} \quad (4.39)$$

For the simulation, the value computed from (4.39) was -0.0704 meters, which corresponds well with what is seen in Figure 4.17. Equation (4.40) approximates the longitudinal error with respect to the desired path, where ψ_{err} is the difference between

the heading of the desired path and the tractor heading during the GPS delay, and ν_{err} is the angle between the desired path and the course angle.

$$e_{longitudinal\ to\ path} = -[V_x \cos(\psi_{err}) - V_y \sin(\psi_{err})] T_{lag} = -V_v \cos(\nu_{err}) T_{lag} \quad (4.40)$$

Note that the above equation is an approximation since the sensor noise covariances in the estimator will provide some filtering and there is an interaction of errors.

Figure 4.18 shows that the error in the east position from the uncompensated system can produce errors that would affect the tractors lateral error tracking performance. If the measurement delay is not compensated, the GPS measurement of the tractor could be to the left of the desired path when the tractor is actually to the right of the desired path. This would cause the controller to move the tractor in the wrong direction leading to instability. The error shown in Figure 4.18 is due to the effect of the longitudinal error entering into the East error at small heading angles which affects the lateral error of the tractor since it is not always heading parallel to the line it is tracking. Equation (4.41) provides an estimate of the lateral error in the estimator due to the GPS measurement delay.

$$e_{lateral\ to\ path} = -[V_x \sin(\psi_{err}) + V_y \cos(\psi_{err})] T_{lag} = -V_\phi \sin(\nu_{err}) T_{lag} \quad (4.41)$$

For the simulation in Figure 4.18, the maximum value of ψ_{err} was 0.115 radians which resulted in a maximum lateral error of 0.008 meters. This corresponds very well to the predicted lateral error of 0.00808 using Equation (4.41).

The lateral errors induced from this measurement latency can also be important if the tractor is oscillating on the verge of instability, since it could cause the tractor to go unstable. Recall that measurement latency can be modeled as a loss of phase in the

system which reduces the phase margin [Franklin, 2002]. The compensated system still contains some of the cosine wave but its errors are much more manageable.

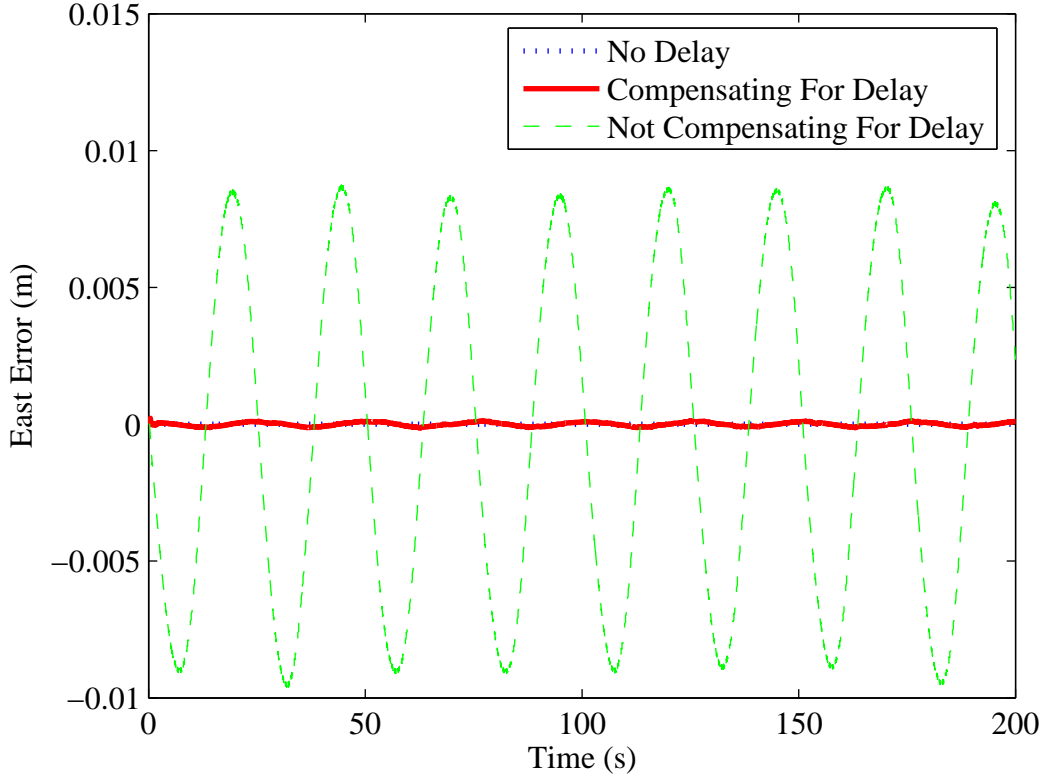


Figure 4.18: East error

Figure 4.19 shows that the heading error produces errors that appear similar to that of the error in the lateral direction from the vehicle. Equation (4.42) approximates the heading estimation error due to the measurement latency.

$$e_{course} = -rT_{lag} \tag{4.42}$$

For the simulation in Figure 4.19 the maximum heading error using Equation (4.42) is 0.00225 radians which corresponded well with the results in Figure 4.19.

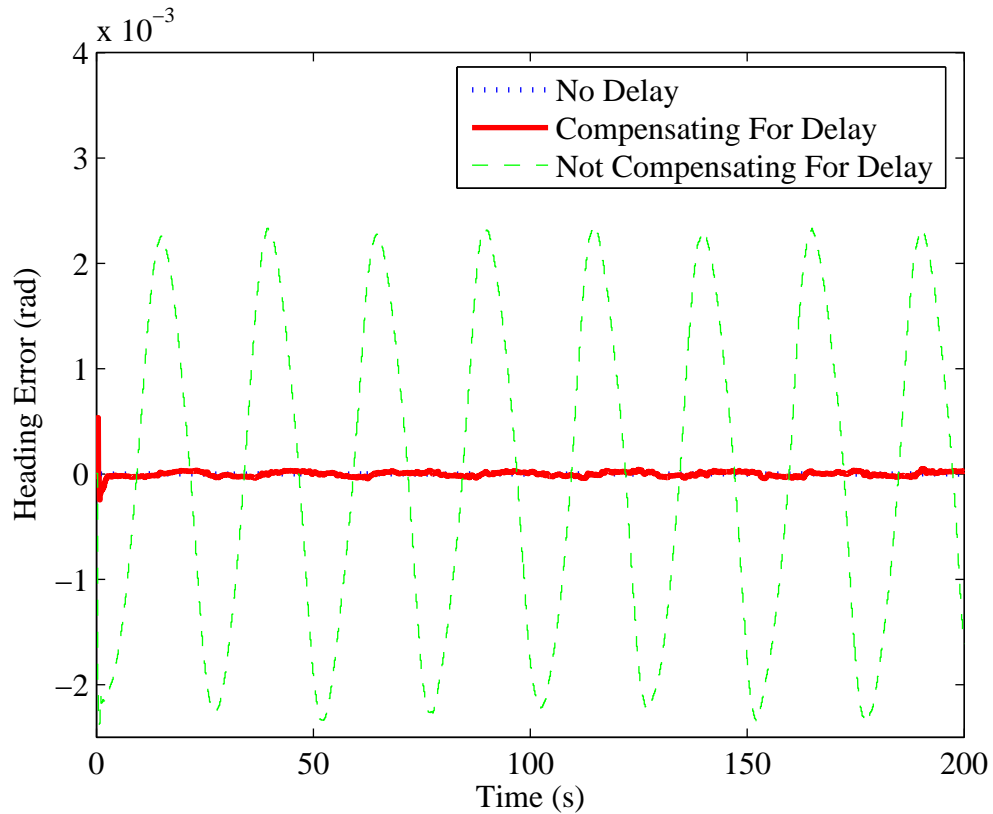


Figure 4.19: Heading Error

The covariance estimates of the estimators with no GPS measurement delay and with the delay compensation are shown in Figure 4.20. As can be seen, the uncertainty in the compensated system is only slightly higher than without the delay. Additionally, no lag can be seen in the covariance estimates between the two simulations. The north estimate is also cleaner than east estimate. This is because the uncertainty in course does not enter into the position state in the direction of course (as seen in Equation (4.32)), which is mostly in the direction of north in this simulation.

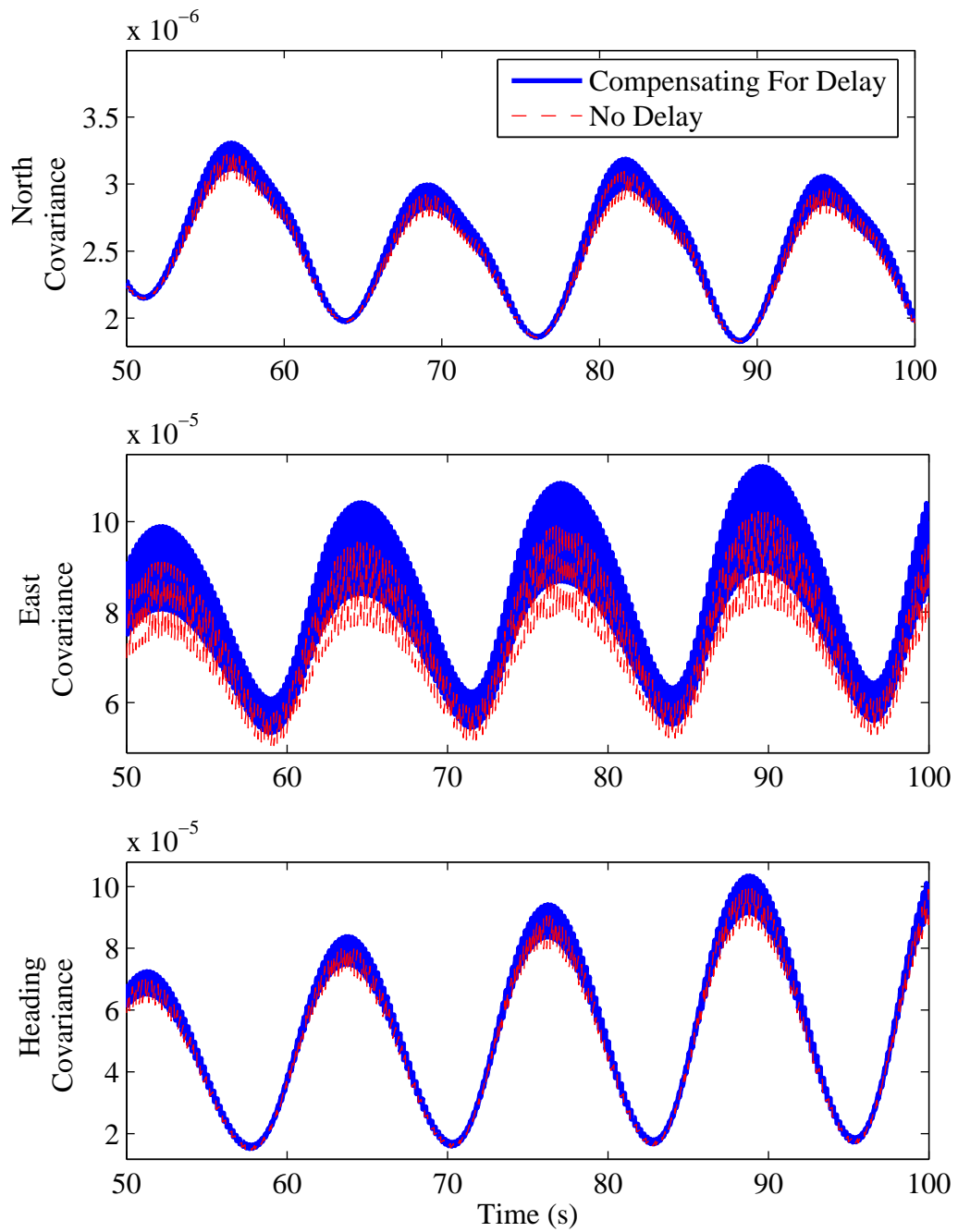


Figure 4.20: Comparison of covariances for an estimator with no GPS measurement delay and an estimator that compensates for the delay.

4.7 Summary and Conclusions

Details on the design of an estimator to estimate the yaw rate, yaw rate bias, and M_{DC} were given in this chapter. A method was given that determined when to estimate the yaw rate bias and M_{DC} so that disturbances did not dominant the estimation of M_{DC} . It was shown that with the covariance resetting, the estimate of M_{DC} would converge quickly. A solution to estimating the bias during low levels of excitation was also explained and the effect of the neglected dynamics on the estimation was displayed.

It was shown that most of the errors occurred because of magnitude errors between the estimator model and actual system and not phase errors. It was also shown that the covariance estimate for the estimated M_{DC} was lower than the actually accuracy of the estimated M_{DC} . The errors in the estimate of M_{DC} caused by the magnitude errors were found to decrease as the velocity and hitch loading were increased. A method of compensating the adaptation for these errors was found by approximating the pole locations. The rate of convergence of M_{DC} due to the forgetting factor was found to be independent of its offset and was instead simply a function of the longitudinal velocity times the steer angle. It was shown that M_{DC} would converge faster with higher amplitudes of excitation and with a larger forgetting factor on the estimated state. However, increasing the forgetting factor resulted in a noisier estimate of M_{DC} .

The design of the position estimator for providing faster updates of position was also detailed. This estimator was designed to compensate for the delay in the receipt of a GPS message since it was shown that the effect of this lag could cause large position errors. Equations were provided that approximated the errors induced by the GPS lag.

CHAPTER 5

EXPERIMENTAL IMPLEMENTATION

5.1 Introduction

The results of experimental tests using the controllers and estimators discussed in previous chapters are given in this chapter. A John Deere 8420 tractor was used for the experimental tests. A Bosch gyroscope was used to measure yaw rate and a linear potentiometer was used to measure the steer angle. Both measurements were synchronized to GPS measurements using a GPS pulse per second (PPS). The GPS measurements were provided by a Starfire GPS receiver. The delay in the GPS messages was obtained using a ten kilohertz clock synchronized to the one hertz clock (PPS) as discussed in Chapter 4.

5.2 Trajectory Design

In this thesis all tractor trajectories consist of straight line segments. Figure 5.1 displays a desired path in a North-East coordinate system. The desired path is defined by a reference point (N_{ref}, E_{ref}) and a reference heading (ψ_{ref}) . The point (N, E) is the location of the tractor. (N_{des}, E_{des}) is the desired point on the path which is defined by a line perpendicular to the path that goes to the point (N, E) . The tractor position can then be described as a longitudinal distance from the reference point and a lateral distance from the path.

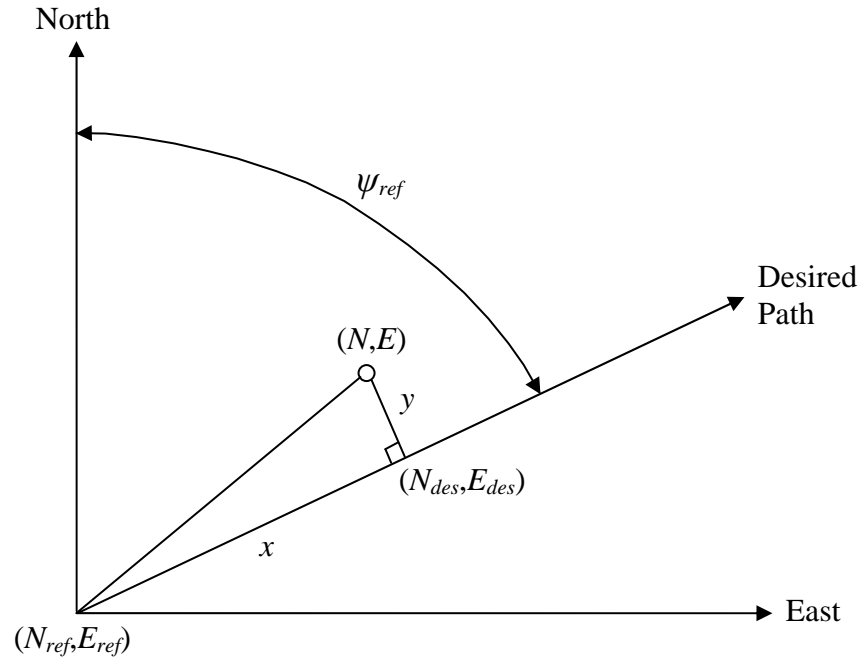


Figure 5.1: Tracking a straight line.

Using the coordinate transformation given in Equation (5.1) the longitudinal and lateral distances can be found from the North-East coordinate system.

$$\begin{bmatrix} x \\ y \end{bmatrix} = \begin{bmatrix} \cos(\psi_{ref}) & \sin(\psi_{ref}) \\ -\sin(\psi_{ref}) & \cos(\psi_{ref}) \end{bmatrix} \begin{bmatrix} N - N_{ref} \\ E - E_{ref} \end{bmatrix} \quad (5.1)$$

It was shown in Chapter 4 that higher frequencies can cause the estimator to estimate the incorrect value of M_{DC} . Thus, it can be advantageous to prevent the tractor from executing a step input by redrawing the path when the lateral distance is large and conducting a steady-state turn to the path. Additionally, if the tractor is at too large of an offset it will approach the desired path perpendicular to it, creating an unsatisfactory response. Therefore, the desired path is redefined using a circular path, which is tangential to the desired straight line trajectory, when the tractor is a large

distance away from the desired line. A description of the circular path is shown in Figure 5.2.

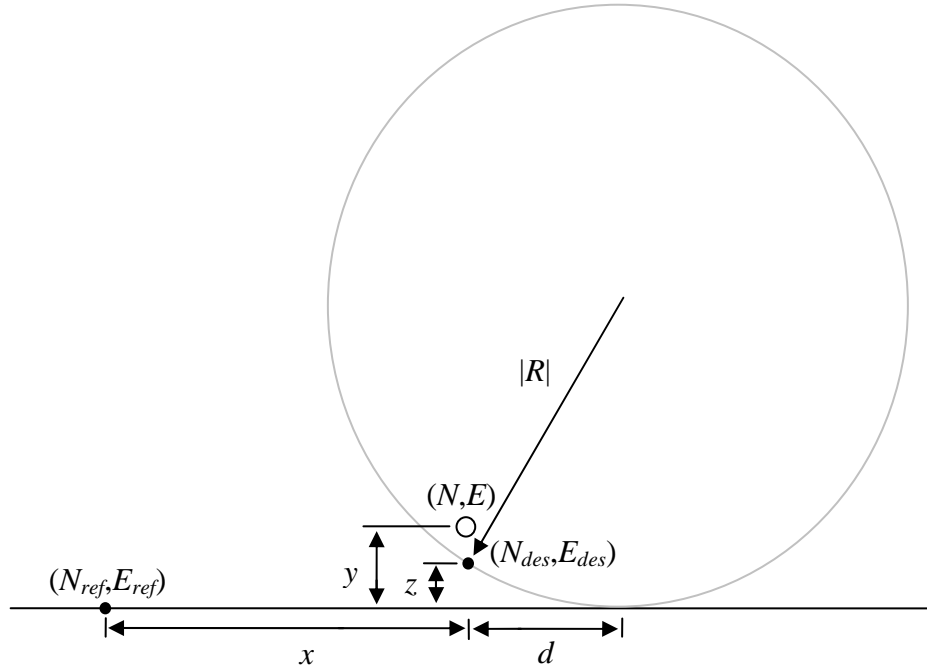


Figure 5.2: Curved trajectory to the straight line.

The value z is the distance between the circular path and the straight line path. When it is determined that the offset from the desired straight line path is too large, the circular path is formed by setting the current lateral offset as shown in the equation below.

$$x_{init} = y \quad (5.2)$$

The distance d that is desired for when the straight line path and the curved path converge is then computed as a function of the initial offset using Equation (5.3), where l is a value larger or equal to one.

$$d_{init} = lx_{init} \quad (5.3)$$

As will be seen in the next few equations l sets the rate to which the tractor will (limited by the tractor dynamics) approach the line trajectory. In this work l was chosen to be 4.

The radius can then be calculated by solving for the hypotenuse of a triangle that takes into account the initial offsets as shown below.

$$R^2 = (d_{init})^2 + (radius - x_{init})^2 \quad (5.4)$$

Substituting Equation (5.3) into Equation (5.4) results in Equation (5.5), where the sign of R contains the information corresponding to which side of the straight line the circular path is on.

$$radius = \frac{l^2 + 1}{2} x_{init} \quad (5.5)$$

Solving for Equation (5.4) with the current offsets instead of the initial offsets, the distance between the circular and straight path while the tractor is moving can be solved as shown below.

$$x = radius - sign(radius)\sqrt{radius^2 - d^2} \quad (5.6)$$

The lateral distance to the circular path can then be found using Equation (5.6) and the distance y .

5.3 Results

To first validate the ability of the algorithms to provide correct estimates of M_{DC} . Experimental test were conducted. For these experiments, the tractor was commanded to track a straight line from an initial offset. The estimator used an initial value of M_{DC} set to 0.25. Figure 5.3 shows the results of two tests. The on-line experimentally estimated

M_{DC} values have less than a five percent error from the true value identified in Chapter 2 ($M_{DC} = 0.334$).

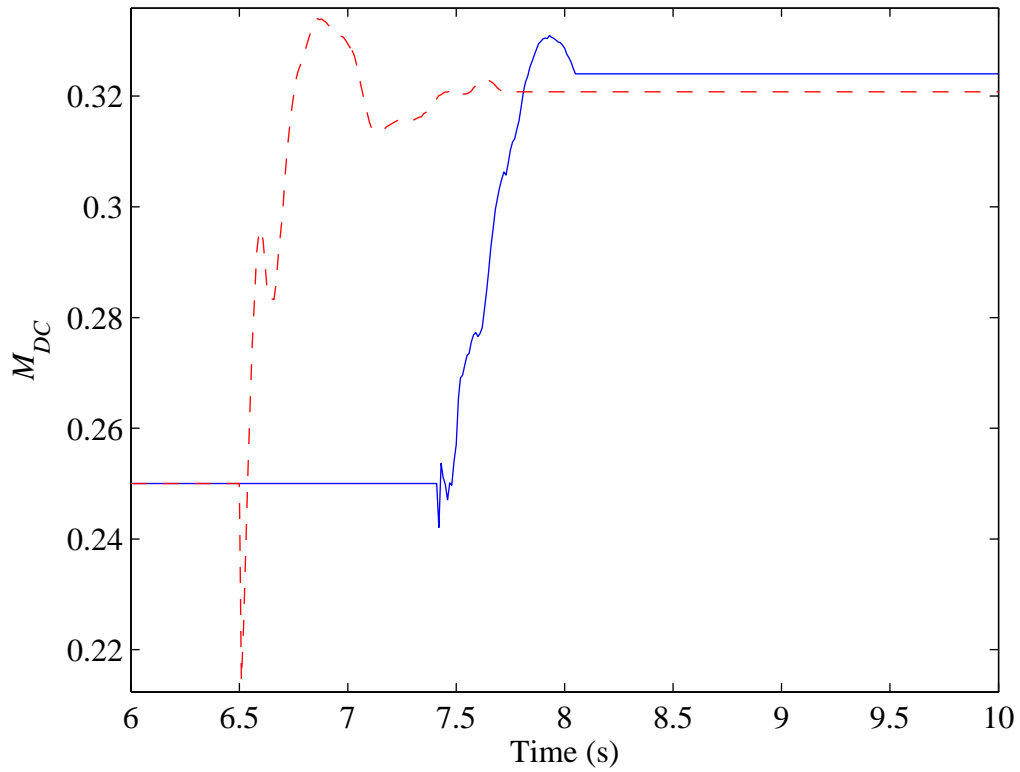


Figure 5.3: Estimation of M_{DC} during experimental tests.

Tests were also conducted to determine how the lateral error was affected by changes in velocity. Figure 5.4 shows that the lateral error increases only slightly with increased velocity.

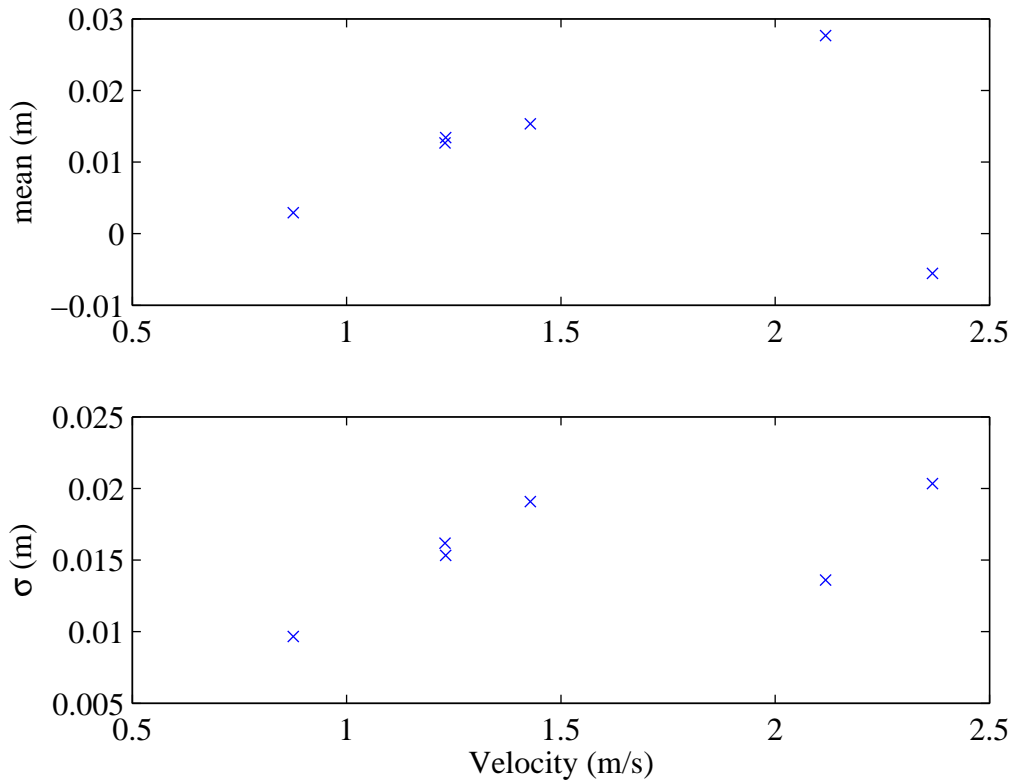


Figure 5.4: Lateral error versus velocity

The tracking performance of the controller without an implement is displayed in Figure 5.5, where five experimental results are shown. As seen in the figure, the tracking performance appears to remain fairly constant for each of the tests.

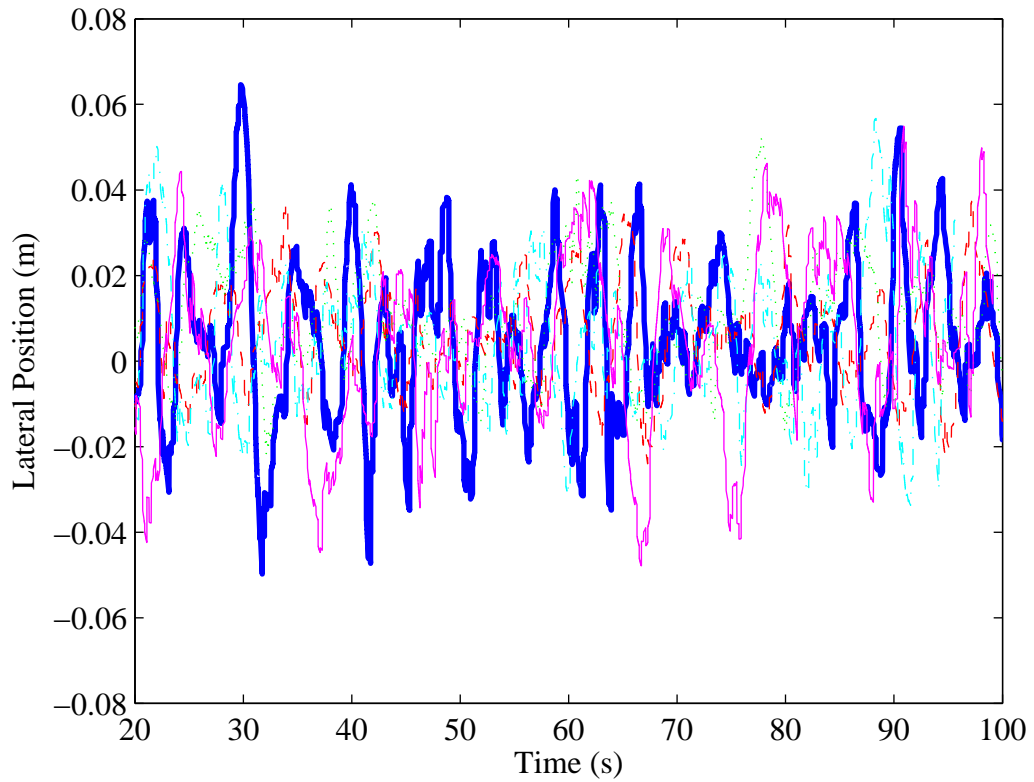


Figure 5.5: Lateral error without an implement.

In Figure 5.6 the tracking performance of the controller with a four shank ripper at a twelve inch depth is shown for five experimental tests. As shown in the above figure, the lateral tracking accuracy degrades slightly with the implement.

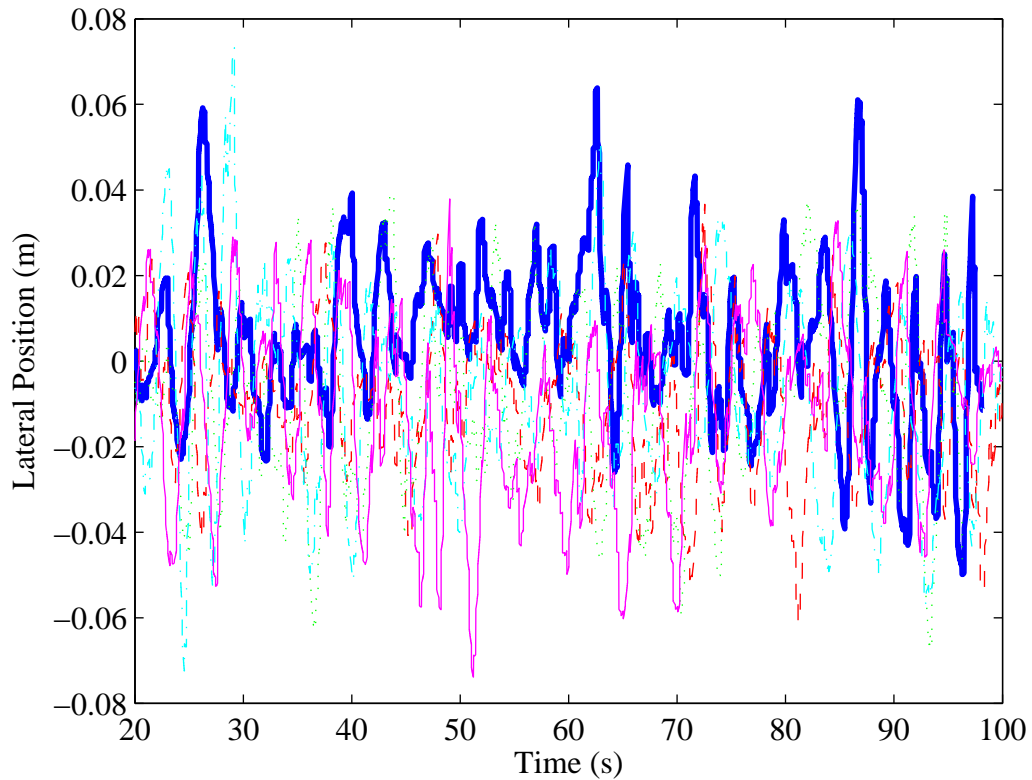


Figure 5.6: Lateral error with a four shank ripper at a twelve inch depth.

The corresponding mean and standard deviation of the experimental tests with and without an implement are shown in Table 5.1. As can be seen in the table, the standard deviations of the controlled runs with an implement are larger than without an implement. This is most likely due to the fact that the implement induces larger disturbances into the system. However, the fact that the experimental control accuracy with and without an implement is fairly consistent shows that the adaptive control algorithm, based on on-line estimation of M_{DC} , provides an effective means to handling the tractor dynamic variations.

Table 5.1: Statistics of lateral error at a constant velocity

Run	No Implement		Ripper at 12" depth	
	Mean (m)	σ (m)	Mean (m)	σ (m)
1	0.00491	0.0191	0.00496	0.0187
2	0.00639	0.0120	-0.0105	0.0167
3	0.0109	0.0156	-0.00747	0.0221
4	0.00454	0.0167	-0.00646	0.0228
5	0.00453	0.0205	-0.0118	0.0210
Average	0.00625	0.0168	-0.0252	0.0202

5.4 Summary and Conclusions

This chapter has detailed the experimental implementation of the estimation and control algorithms developed in this thesis. The trajectories used for the tractor controller were discussed. Experimental results showing the accuracy of the estimation algorithms were then provided. Experimental tests demonstrated that the tracking response changed little with velocity. The average standard deviations while varying velocities was found to be 0.016 m. It was also shown that the standard deviation of the lateral position changed little with hitch loading with a standard deviation of 0.0168 m without an implement and 0.0202 m with a 4 shank ripper at a 12" depth while driving at 2 mph.

CHAPTER 6

FIXED POINT IMPLEMENTATION OF YAW RATE ESTIMATOR

6.1 Introduction

Implementation of a Kalman filter is difficult in a fixed point microprocessor. The propagation of the covariance presents the largest challenge, since it can be poorly conditioned if small machine precision is used. However, filters that propagate the square root of the covariance are more easily manageable, because they propagate a matrix that has the square root of the condition number of what the Kalman filter requires. Examples of square root Kalman filters include the square root covariance filter and square root information filter [Anderson, 1979; Bierman, 1977; Maybeck 1979a].

In this chapter, a square root covariance filter (SRCF) will be used to show that the Kalman filter from Chapter 4 can be implemented using fixed point math. The estimator provides an estimate of the slope of the DC gain with respect to velocity of the transfer function between steer angle and yaw rate (M_{DC}).

6.2 Square Root Covariance Filter

The square root covariance filter is derived from the Kalman filter equations. It uses orthogonal matrices, T_1 and T_2 , shown in Equations (6.2) and (6.3) to solve for upper triangular matrices.

$$x_{k|k-1} = f(x_{k-1}, u_{k-1}) \quad (6.1)$$

$$\begin{bmatrix} S_{k|k-1}^T \\ 0 \end{bmatrix} = T_1 \begin{bmatrix} S_{k-1}^T F^T \\ Q^{1/2T} L^T \end{bmatrix} \quad (6.2)$$

The process of splitting the matrix into an orthogonal and upper triangular matrix is known as QR decomposition and the most popular methods used for square root Kalman filters are the householder [Golub, 1989] and modified Gram-Schmidt methods. The householder method is used in this work. Equations (6.1) and (6.2) consist of the time update of the estimator. Note that the state time update is the same as in the Kalman filter.

Equations (6.3-6.5) show the measurement update equations for the estimator.

$$\begin{bmatrix} (R + H^T P H)^{1/2T} & \tilde{K}^T \\ 0 & S_k^T \end{bmatrix} = T_2 \begin{bmatrix} R^{1/2T} & 0 \\ S_{k|k-1}^T H^T & S_{k|k-1}^T \end{bmatrix} \quad (6.3)$$

$$K = \tilde{K} (R + H^T P H)^{-1/2} \quad (6.4)$$

$$x_k = x_{k|k-1} + K (z - H x_{k|k-1}) \quad (6.5)$$

The QR factorization displayed in Equation (6.3) returns terms that are used for both the covariance square root and the Kalman gain. The state measurement update shown in (6.5) is the same as the Kalman filter state measurement update. In Equation (6.4) it is evident that a matrix inverse is needed if there is more than one measurement. However, sequential processing is used in square root filters to eliminate the need for a matrix inversion.

When compared with the Kalman filter the square root covariance filter takes more computation time [Bierman, 1977; Kaminski, 1971]. This is due to the fact that the SRCF needs more multiplications, additions, divisions, as well as square root calculations.

6.3 Fixed Point Math

For the fixed point implementation, additions and subtractions were performed as normal. Multiplications were performed using Equation (6.6), where \gg is the right shift operator and N is the number of bits to shift.

$$ab \gg N \quad (6.6)$$

Divisions were carried out using Equation (6.7), where \ll is the left shift operator.

$$(a \ll N)/b \quad (6.7)$$

An overflow would result if the answer to the equations was larger than 2^{15} , since variables were defined as 16 bit signed integers.

The householder method was used on Equation (6.8) as an example of the accuracy of the fixed point implementation of the algorithm.

$$A = \begin{bmatrix} 345 & 156 & 543 & 15 \\ -435 & 261 & 623 & 89 \\ 210 & 45 & 96 & 112 \\ -19 & 61 & 75 & 412 \end{bmatrix} \quad (6.8)$$

The householder method reduces Equation (6.8) into $A=QR$, by doing a column wise reduction.

Equation (6.9) shows the result of the decomposition when floating point is used.

$$R = \begin{bmatrix} 607.2026 & -96.4271 & -125.4095 & -32.0321 \\ 0 & 299.4332 & 816.926 & 176.2676 \\ 0 & 0 & 121.3396 & -352.4878 \\ 0 & 0 & 0 & 184.6349 \end{bmatrix} \quad (6.9)$$

Performing the decomposition in fixed point results in errors build upon one another as each column is reduced as shown in Equation (6.10).

$$R = \begin{bmatrix} 605 & -92 & -126 & -30 \\ -12 & 295 & 801 & 182 \\ 4 & -3 & 130 & -333 \\ -2 & 0 & 0 & 214 \end{bmatrix} \quad (6.10)$$

This implies that the first state will have the most accurate covariance estimate.

6.4 Estimator Model

Since the first state will have the most accurate covariance estimate, the slope of the DC gain (M_{DC}) was made the first state. The yaw rate state in the estimator was set to be scaled by $N = 9$ bits from the units of degrees/second. Meaning that the yaw rate state would be yaw rate in degrees/second times 2^9 . The measured yaw rate, velocity, and steer angle were also scaled by 9 bits. M_{DC} was scaled by N bits plus $N_{DC} = 4$ bits or $2^{(N+N_{DC})}$. The bias was scaled by N bits plus $N_{bias} = 4$ bits or $2^{(N+N_{bias})}$. M_{DC} and the bias were scaled by extra bits in order to reduce the error in those states caused by the fact that MDC and the bias were smaller in magnitude then the yaw rate state.

Equation (6.11) shows the state time update equations, where the states are M_{DC} , yaw rate, and the yaw rate bias.

$$\begin{aligned} M_{DCk} &= M_{DCk-1} \\ r_k &= [(M_{DCk-1} \gg N_{DC}) \mathcal{V}_k \gg N] \delta_k \gg N \\ r_{biask} &= r_{biask-1} \end{aligned} \quad (6.11)$$

The M_{DC} and r_{bias} values are simply the previously computed values. The M_{DC} state has to be shifted down in the yaw rate computation since it has a larger scaling in the estimator. The order of the shifts can be changed, as long as it does not increase the risk of overflow.

Equations (6.12-6.14) display the Jacobian matrices used in the square root covariance filter.

$$F = \begin{bmatrix} 1 \ll N & 0 & 0 \\ V\delta \gg (N + N_{DC}) & 0 & 0 \\ 0 & 0 & 1 \ll N \end{bmatrix} \quad (6.12)$$

$$H = [0 \quad 1 \ll N \quad 1 \ll (N - N_{bias})] \quad (6.13)$$

$$L = \begin{bmatrix} 1 \ll N & 0 & 0 \\ 0 & 1 \ll N & 0 \\ 0 & 0 & 1 \ll N \end{bmatrix} \quad (6.14)$$

Note that in F , the term related to the partial of the yaw rate with respect to M_{DC} is shifted down due to the extra scaling on the parameter. Additionally in H , the partial derivative with respect to the bias is shifted up less due to the extra scaling on the bias.

Equations (6.15) and (6.16) contain the square root of the noise covariances, which are displayed as a function of the extra scaling on the states.

$$Q^{1/2} = \begin{bmatrix} 4 \ll N_{DC} & 0 & 0 \\ 0 & 154 & 0 \\ 0 & 0 & 6 \ll N_{bias} \end{bmatrix} \quad (6.15)$$

$$R^{1/2} = [68] \quad (6.16)$$

The noise values had to be larger than the nominal values given in Chapter 4. This was done do to the fact that even though the covariance may not converge to zero, the Kalman gain can become zero if the covariance is too small.

The initial covariance square root is shown in Equation (6.17).

$$S = \begin{bmatrix} 0 & 0 & 0 \\ 0 & 0 & 0 \\ 0 & 0 & 460 \ll N_{bias} \end{bmatrix} \quad (6.17)$$

The initial value for the yaw rate covariance is set to zero, since the estimator will be initialized with the most recent yaw rate measurement. The M_{DC} covariance square root initial value is also set to zero because adaptation will not be performed until there is adequate excitation.

To determine when to estimate the parameter, Equation (6.18) was calculated recursively, where $N_w = 6$ was chosen to prevent an overflow.

$$status = \sum_{m=0}^{19} (\delta_{k-m}^2 \gg N_w) \quad (6.18)$$

The equation is simply an estimate of the covariance of the steer angle over a short period of time. This period was chosen to be one second at a twenty hertz resolution.

The value of status was arbitrarily chosen to be 1920, therefore, if $status < 1920$ then it was determined that there was insufficient excitation to estimate M_{DC} . Therefore in order to prevent the parameter from being estimated, the first element of the Kalman gain was set to zero ($K(0,0) = 0$). Once there was adequate excitation to estimate M_{DC} and M_{DC} was not previously being estimated, then the covariance for M_{DC} was reset to $S(0,0) = 25 \ll N_{DC}$ in order to inject some uncertainty into the state.

6.5 Comparison between Fixed Point and Floating Point Implementation

To test the performance of the fixed point estimator, experimental data was used during a straight line tracking test with an initial offset. A floating point estimator was

also used for comparison. Note that for parity of comparison, the noise values used in Equations (6.15-6.16) were used in both estimators. Figures 6.1-6.4 show the comparison between the results using the fixed point versus floating point estimators. Note that in the following figures the scaled fixed point values have been rescaled back to more traditional values. It can be seen in Figure 6.1 that there was enough excitation to estimate the parameter at the beginning of the experiment. When the yaw rate moved to switch signs and was around zero, it was determined that there was not enough excitation and the estimation of M_{DC} was stopped. Once the yaw rate completed changing signs, the windowed analysis determined that there was adequate excitation to continue estimating M_{DC} .

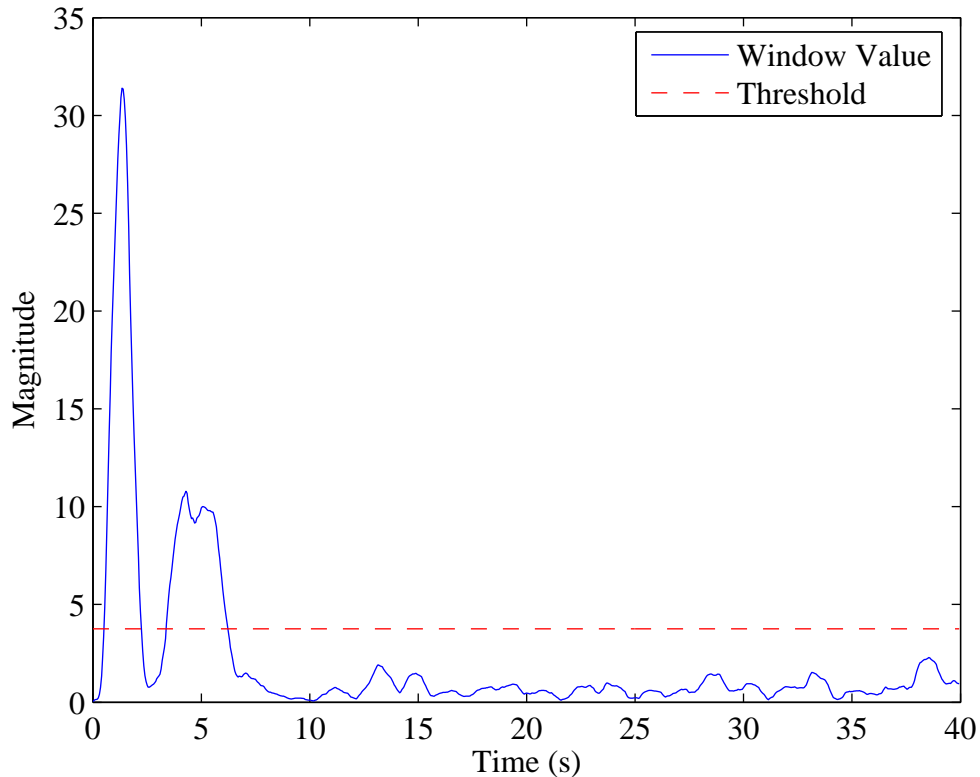


Figure 6.1: Windowed analysis of experimental data to determine when to adapt.

The estimate of M_{DC} using the fixed point estimator initially overshoots the estimate from the floating point estimator as seen in Figure 6.2. Unfortunately the M_{DC} estimate does not recover from the initial overshoot during the second opportunity for estimation.

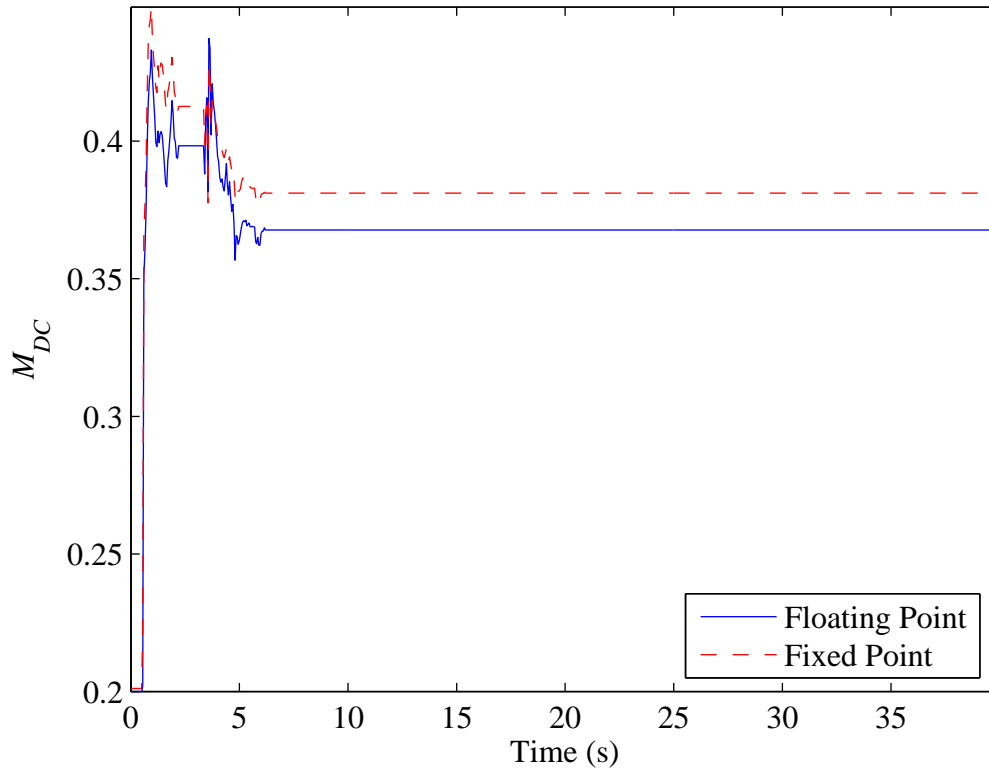


Figure 6.2: Comparison of the estimation of the slope of the dc gain equation with respect to velocity for fixed and floating point using experimental data

Also, Figure 6.3 shows that there exists a slight difference in the estimated yaw gyro bias from the two estimators. This results in a small difference in the yaw rate estimate seen in Figure 6.4. The differences in the estimation of M_{DC} can likely be attributed to the differences in the estimate of the yaw rate bias. Note that if M_{DC} had not

been made the first state, errors in the computation in the covariance could have caused the Kalman gain to go to zero even while the windowed analysis showed there was enough excitation. This would cause the estimation to turn off, possibly before it converged to the correct value.

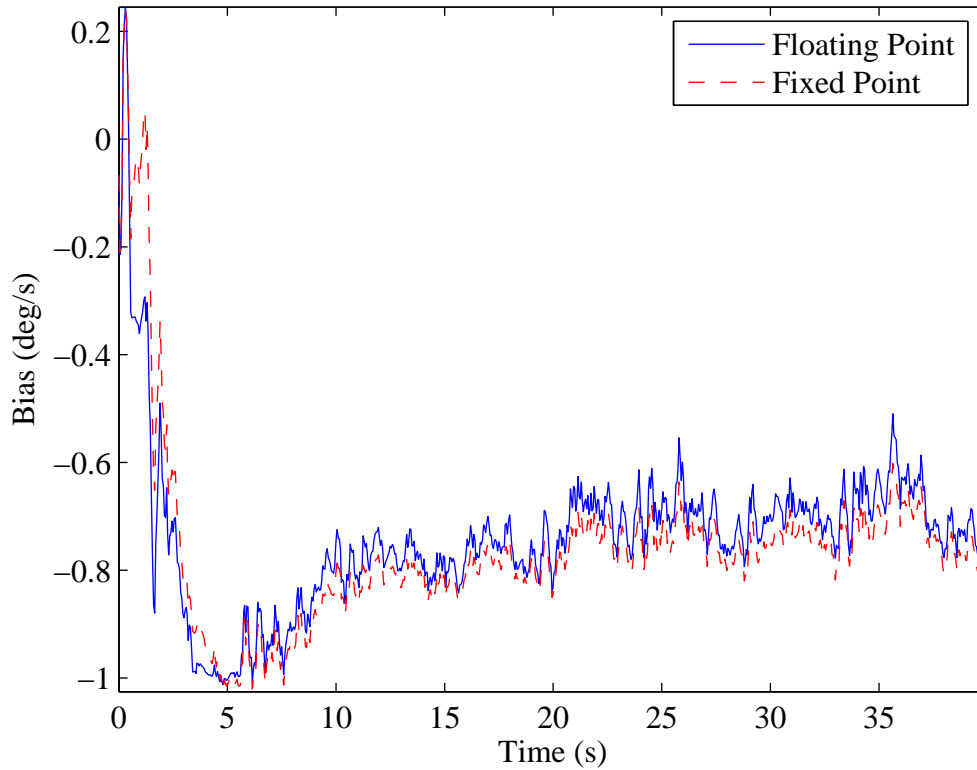


Figure 6.3: Comparison of the estimation of the yaw rate bias in fixed and floating point using experimental data

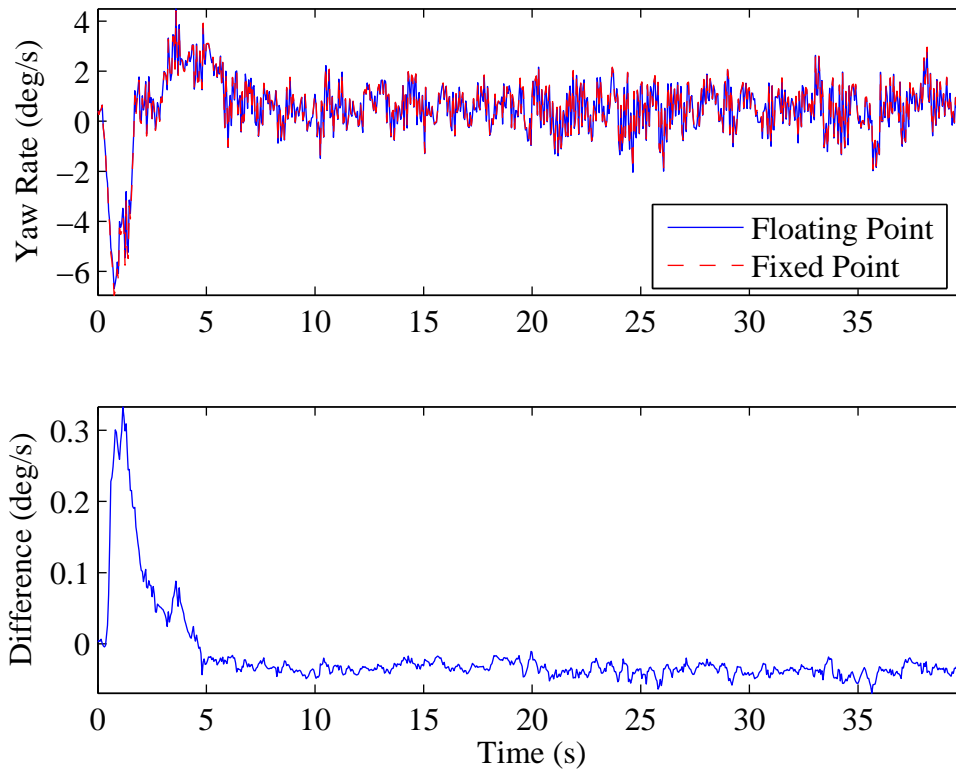


Figure 6.4: Comparison of the estimation of yaw rate in fixed and floating point using experimental data

In order to test the repeatability of the estimator and whether the estimator was estimating the correct values, simulated data that was generated using a sine wave steer angle input and a second order disturbance model. The results are given in Figures 6.5-6.8. As seen in the figures, the estimates for the fixed and floating point estimators both approach the correct value every time the parameter is estimated.

Recall that the process noise values in Equation (6.15) were set higher than the actual noise values in order to prevent the Kalman gain from going to zero. This causes

the bias to incorporate a scale factor error effect (from the sine wave) due to M_{DC} having not completely converged.

In Figure 6.7, it can be seen that the covariance resetting did not allow for the convergence on the correct value the first time it tried to estimate the parameter. However, resetting the covariance twice allowed the M_{DC} estimate to approach the correct value. Again this was due to the process noise values being set higher than the actual values. Although, it took longer to converge with the larger noise covariances, the M_{DC} estimate did converge to the correct value. As shown in Figure 6.8, there were multiple opportunities where sufficient excitation existed for M_{DC} to be estimated.

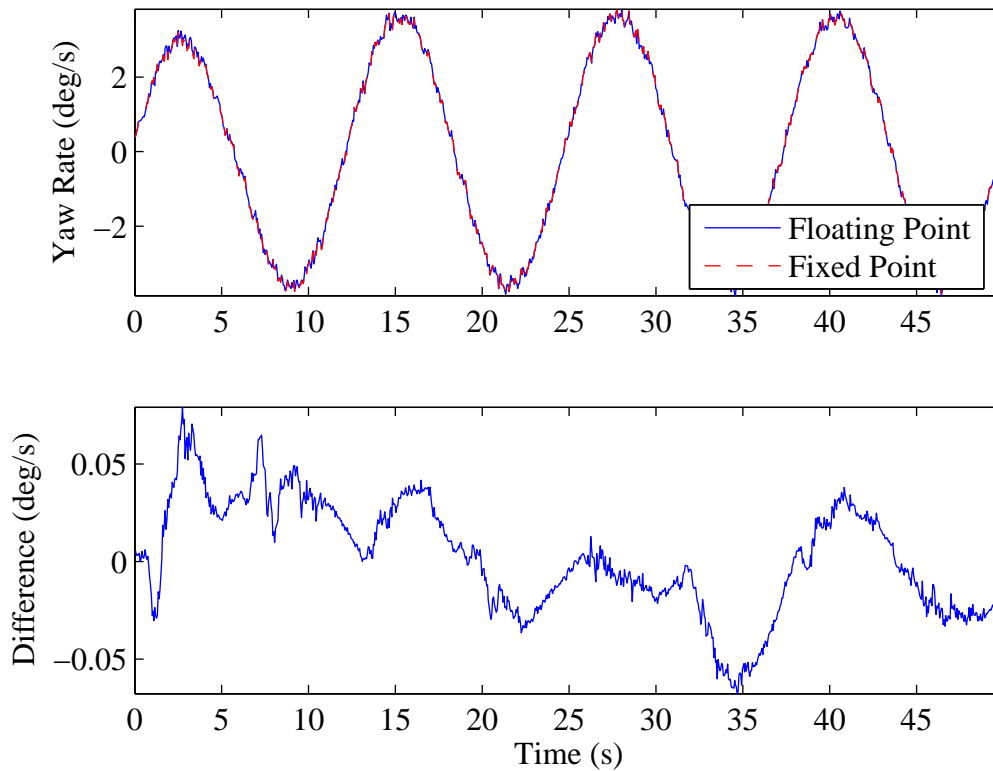


Figure 6.5: Comparison of the estimation of yaw rate in fixed and floating point for simulated data

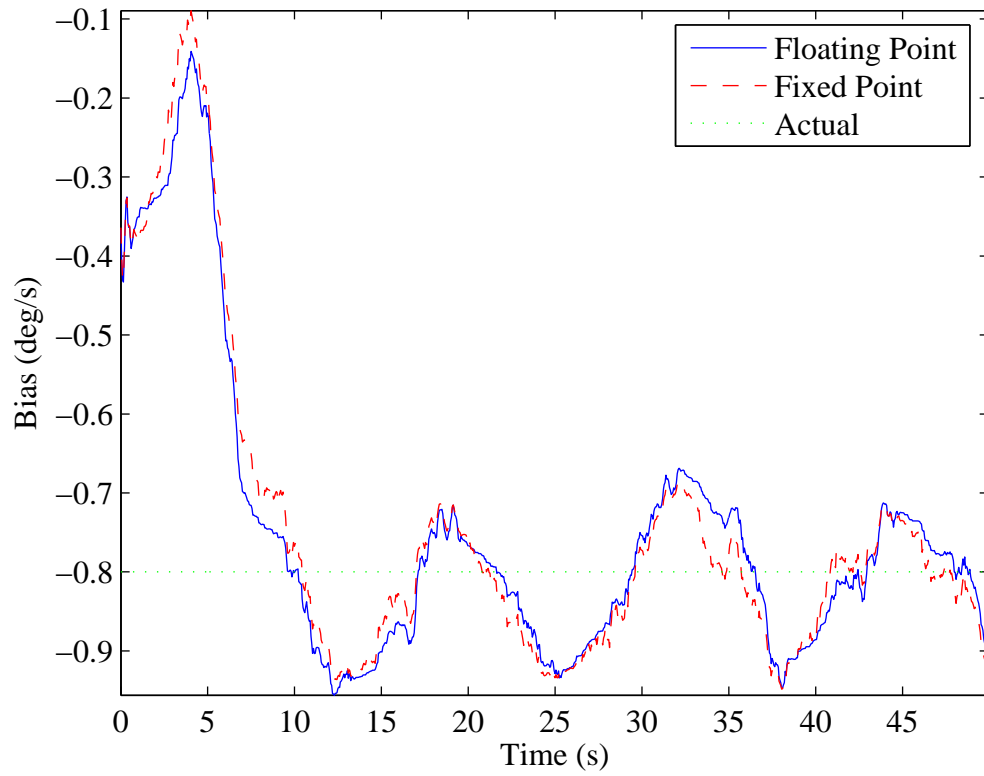


Figure 6.6: Comparison of the estimation of the yaw rate bias in fixed and floating point using simulated data

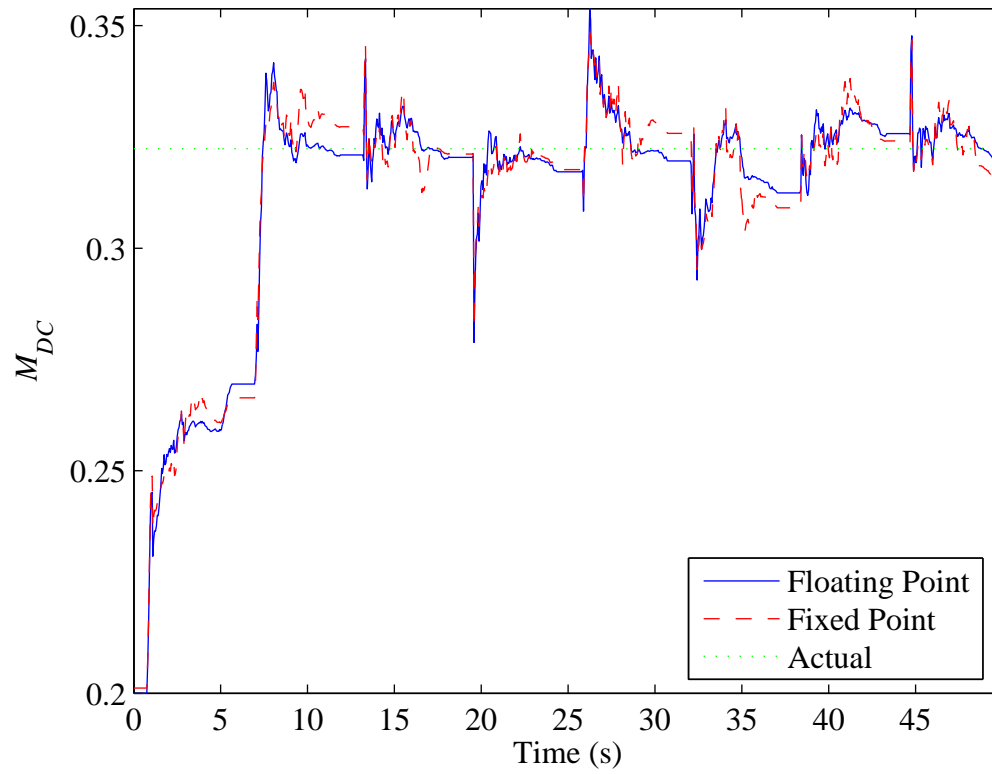


Figure 6.7: Comparison of the estimation of the yaw rate dc gain slope with respect to velocity in fixed and floating point for simulated data

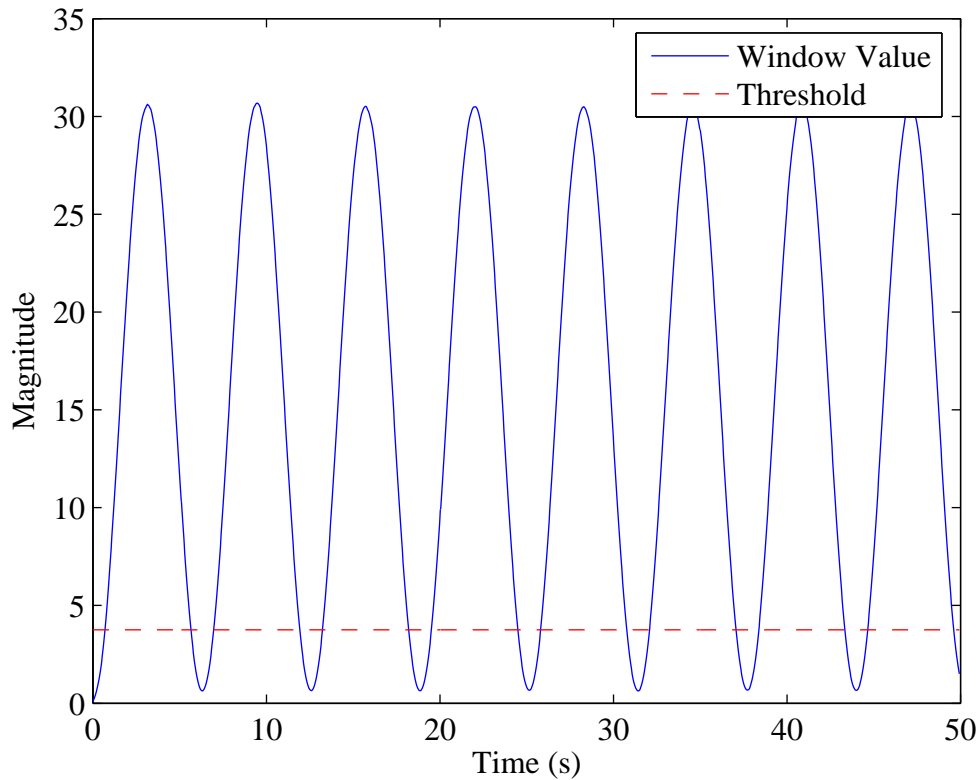


Figure 6.8: Windowed analysis of experimental data to determine when to adapt.

6.6 Summary and Conclusions

A square root covariance filter was used to implement the yaw rate estimator using fixed point math. The methods for the numerical operations were shown as well as the fact that the first state would have the most accurate covariance estimate. The modifications of the Kalman filter matrixes were also given, where the noise covariances had to be made larger than necessary to prevent the Kalman gain from going to zero even when the covariance was not zero. The algorithm was then compared using both a floating point estimator and fixed point estimator with experimental data. Finally, it was

shown with simulated data that even with the increased noise values in the fixed point estimator that the correct values could be converged on.

CHAPTER 7

CONCLUSION

7.1 Summary

In Chapter 2, system identification of the steering servo found that the steering servo could be modeled using a nonlinear input transformation plus a transfer function with an integrator. A review of previous yaw dynamic models for tractors found that they did not match the dynamics of the 8420 tractor identified in this thesis using system identification tests. From the system identification tests of the steer angle to yaw rate transfer function it was found that the system should be modeled as a fourth order model with a non-minimum phase zero. It was found that the DC gain of the steer angle to yaw rate transfer function was linear and that only the slope of the DC gain with respect to velocity varied with velocity and implement loading. A model of the tractor with various hitch loadings was identified for use in the controller design.

Chapter 3 detailed the design of the cascaded controllers for the steering servo, yaw rate, and position of the tractor. The method of determining the controller gains using parameter estimation was discussed. The sensitivity of the controller to the model simplifications was given and it was shown that the stability margins of the controller improve with increasing hitch loading and velocity. The sensitivity of the controller to the incorrect velocity was shown. It was found that the system could be unstable if designed for too low of a velocity and could have an undesirably slow response when

designed for too high of a velocity. Similarly, it was found that an estimate of M_{DC} that was too low could lead to instability and too high of an estimate could lead to a slow response.

In Chapter 4, the design of an estimator to estimate the yaw rate, yaw rate bias, and M_{DC} was detailed. It was shown that a windowed auto-correlation could be used to determine when to estimate M_{DC} so that disturbances do not dominant the estimate. It was shown that with the covariance resetting, the estimate of M_{DC} would converge quickly. The effect of the neglected dynamics on the estimation was displayed and it was concluded that most of the errors occurred because of magnitude errors between the estimator model and the true dynamics and not phase errors. It was also shown that the covariance estimate for the estimated M_{DC} was lower than it actually should be, making it unreliable the accuracy of the estimate. The errors caused by neglecting dynamics were found to decrease as the velocity and hitch loading were increased. A method of compensating the adaptation for these magnitude errors was found by approximating the pole locations of the tractor. Even while augmenting the estimator with the dominant poles, the estimation still contained some errors. However, this could be corrected by decreasing the damping ratio of the dominant poles or adding more dynamics to the estimator model. The rate of convergence of M_{DC} due to the forgetting factor was found to be independent of its offset and was instead simply a function of the longitudinal velocity times the steer angle. It was shown that M_{DC} would converge faster with higher amplitudes of excitation and with a larger forgetting factor on M_{DC} . However, the M_{DC} estimate was shown to less accuracy as the forgetting factor was increased. The design of the position estimator for providing higher updates of position was also detailed. This

estimator was designed to compensate for the delay in the receipt of a GPS message. It was shown that not accounting for this latency could cause large position errors. Analytical equations were developed that approximated the errors induced by the GPS lag.

Chapter 5 described the design of the trajectories used to control the tractor in this thesis. Experimental results showing the repeatability of the estimation were given. Experimental tests showed that the tracking response changed little with velocity and hitch loading, validating the adaptive control and estimation algorithms in this thesis.

In Chapter 6, the estimator for the yaw rate, yaw rate bias, and M_{DC} was designed for fixed point implementation using a square root covariance filter. A summary of the fixed point math used was given. An example using a QR decomposition with fixed and floating point operations using the householder method was conducted. It was shown that the first state would have the most accurate covariance estimate. The scaling of the different states was detailed including differences from the estimator developed in Chapter 4. A comparison of estimators designed using fixed and floating point math was displayed for both experimental and simulation data.

7.2 Recommendation for Future Work

An accurate parameter based or analytical model of a tractor needs to be developed. Based on this model a more accurate controller could be designed, since approximations had to be made to the dynamics with the use of an implement. Controllers could also be designed for specific types of implements, with the use of user inputted information on the implement. With the use of a user specified model, the estimate of M_{DC} could more

accurately take into account higher dynamics. The first step would be the design of a model that matches the dynamics without an implement since from system identification tests they appear to be similar. This may include investigating the effect of tire faulty circularity and suspension dynamics. Then, models of various types of implements that take into account the hitch dynamics need to be developed.

Recording the performance of the tractor could lead to improved performance. With the use of a user profile for each implement, the statistics of the use of that implement versus time and location could be stored. A record of the performance over time for each recorded implement could allow for slight variations in the controller to test for improved performance. While a record of the tractor position could reveal differences in the terrain for which different control strategies could be evaluated over time for that location.

REFERENCES

- Anderson, B., and Moore, J., *Optimal Filtering*, Prentice-Hall, 1979.
- Astrom, K. and Wittenmark, B., *Adaptive Control*, Addison-Wesley Publishing Company, 1989.
- Benson, Stombaugh, T.S., Noguchi, N., Will, J.D., and Reid, J.F., “An evaluation of a geomagnetic direction sensor for vehicle guidance in precision agriculture applications”, ASAE Paper 983203, 1998.
- Bell, T., *Precision Robotic Control of Agricultural Vehicles on Realistic Farm Trajectories*, P.H.D. Thesis Department of Mechanical Engineering, Stanford University, June 1999.
- Bevly, D.M., *High Speed, Dead Reckoning, and Towed Implement Control for Automatically Steered Farm Tractors using GPS*, P.H.D. Thesis, Department of Mechanical Engineering, Stanford University, August 2001.
- Bierman, G., “Factorization Methods for Discrete Sequential Estimation”, *Academic Press*, 1977.
- Böhler, H., “Simulation of the Dynamic Loads of a Tractor with the Help of a Multi-Body-System Program”, *Proceedings of the 13th International Conference for the International Society for Terrain-Vehicle Systems*, München, 1999.
- Bryson Jr., A.E., Ho, Y., *Applied Optimal Control*, Hemisphere Publishing Company, 1975.

- Cordesses, et. Al., “CP-DGPS Based Combine Harvester Control without Orientation Sensor,” *Proceedings of the 1999 ION-GPS Meeting*, Nashville, TN, Sept. 1999.
- Franklin, G.F., Powell, J.D., and Workman, M., *Digital Control of Dynamic Systems*, Addison Wesley Longman, Inc., 3rd ed., 1998.
- Franklin, G.F., Powell, J.D., Emami-Naeini, A., *Feedback Control of Dynamic Systems*, Prentice-Hall, Inc., 3rd ed., New Jersey, 2002.
- Gelb, A., et al., *Applied Optimal Estimation*, The MIT Press, Cambridge, MA, 1992.
- Gillespie, T.D., *Fundamentals of Vehicle Dynamics*, Society of Automotive Engineers, Warrendale, PA, 1992.
- Golub, G., and Van Loan, C., *Matrix Computations*, The Johns Hopkins University Press, 1989.
- Haykin, S., *Kalman Filtering and Neural Networks*, John Wiley and Sons, Inc., New York, 2001.
- Hingwe, P., Packard, A.K., Tomizuka, M., “Linear parameter varying controller for automated lane guidance experimental study on tractor semi-trailers”, *Proceedings of the 2000 American Control Conference*, Vol. 3, pp. 2038-2042.
- Kaminski, P., Bryson Jr., A., Schmidt, S., “Discrete Square Root Filtering: A survey of Current Techniques”, *IEEE Transactions on Automatic Control*, Volume 16, Issue 6, Dec 1971 Page(s):727 – 736.
- Maybeck, P.S., *Stochastic Models, Estimation, and Control*, Vol.1, Academic Press, San Francisco, 1979a.
- Maybeck, P.S., *Stochastic Models, Estimation, and Control*, Vol. 2, Academic Press, San Francisco, 1979b.

- O’Conner, M., Bell T., Elkaim G., and Parkinson, B., “Automatic Steering of Farm Vehicles Using GPS”, *Proceedings of the 3rd International Conference on Precision Agriculture*, Minneapolis, MN, June 1996, pp. 767-777.
- O’Conner, M.L., *Carrier-Phase Differential GPS for Automatic Control of Land Vehicles*, P.H.D. Thesis, Department of Aeronautics and Astronautics, Stanford University, December 1997.
- Ogata, K., *System Dynamics*, Prentice Hall, 3rd ed., New Jersey, 1998.
- Owen, R.H., “Directional Dynamics of a Tractor-Loader-Backhoe”, *Vehicle System Dynamics*, Vol. 11, 1982, pp.251-265.
- Pearson, P.J. and Bevly, D.M., “Comparison of Analytical and Empirical Models to Capture Variations in Off Road Vehicle Dynamics”, *Proceedings of the 2005 IMECE Conference*, Orlando, FL.
- Reid, J., Searcy, S., “Vision-based guidance of an agriculture tractor”, *IEEE Control Systems Magazine*, Vol. 7, issue 2, pp. 39 – 43, 1987.
- Rekow, A., *System Identification, Adaptive Control and Formation Driving of Farm Tractors*, P.H.D. Thesis, Department of Aeronautics and Astronautics, Stanford University, December 2001.
- Saarilahti, M., *Soil Interaction Model*, Quality of Life and Management of Living Resources Contract No. QLK5-1999-00991, 2002.
- Stengel, R., *Optimal Control and Estimation*, Dover ed, Dover Publications, Meneola, New York, 1994.

- Stombaugh, T.S., Benson, E.R., and Hummel, J.W., “Automatic Guidance of Agricultural Vehicles at High Field Speeds”, 1998 ASAE Annual International Meeting, Orlando, FL, 1998.
- Svestka, P., Vleugels, J., “Exact motion planning for tractor-trailer robots”, *Proceedings of the 1995 IEEE International Conference on Robotics and Automation*, Vol. 3 , pp. 2445 -2450.
- Versallogic, 2005a: Bobcat 586 Processor Modelue
<http://www.versallogic.com/Products/DS.asp?PN=Bobcat>
- Versallogic, 2005b: VCM-DAS-1 PC/104 Data Acquisition Module
<http://www.versallogic.com/Products/DS.asp?PN=VCM-DAS-1>
- Versallogic, 2005c: VL-ENCL-4 Ruggedized Enclosure
<http://www.versallogic.com/Products/DS.asp?PN=VL-ENCL-4>
- Wan, E.A., and van der Merwe, R., “The Unscented Kalman Filter for Nonlinear Estimation”, *Proceedings of IEEE Symposium*, Alberta, Canada, 2000.
- Wong, J.Y., *Theory of Ground Vehicles*. Wiley, New York, 1978.
- Wu, D., Zhang, Q., and Reid, J.F., “Adaptive steering controller using a Kalman estimator for wheel-type agricultural tractors”, *Robotica*, Vol. 19, pp. 527–533, 2001.
- Zhang, Q., Reid, J.F., Noguchi, N., “Agricultural Vehicle Navigation Using Multiple Guidance Sensors,” *Proceedings of the International Conference on Field and Service Robotics*, August 1999.

APPENDIX A
EXPERIMENTAL SETUP

A John Deere 8420 tractor with an independent link front suspension was used for experimental tests, which is shown in Figure A.1. The tractor was interfaced to with the use of a Controller Area Network (CAN).



Figure A.1: John Deere 8420 Tractor

The algorithm computations were calculated with the use of a Versalogue Bobcat PC/104 CPU shown in Figure A.2. The analog sensors used were recorded with the use of a Versalogue PC/104 data acquisition board shown in Figure A.3. The PC/104 components were stored inside of a PC/104 case from Versalogue shown in Figure A.4.



Figure A.2: Versalogue PC/104 CPU
[Versalogue, 2005a]



Figure A.3: Versalogue PC/104 data acquisition board [Versalogue, 2005b]



Figure A.4: Versalogue VL-ENCL-4 Ruggedized Enclosure [Versalogue, 2005c]

The Bosch IMU shown in Figure A.5 was used to obtain inertial measurements. The linear potentiometer shown in Figure A.6 was used for measurements of steer angle. GPS messages were obtain with the use of the Starfire GPS receiver shown in Figure A.7.

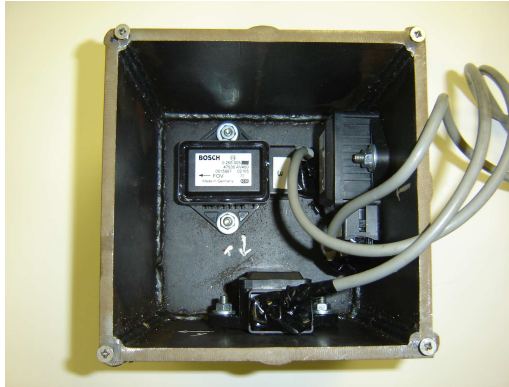


Figure A.5: Bosch IMU



Figure A.6: Steer angle sensor



Figure A.7: Starfire GPS reciever